Development and Proving of a Split Hopkinson Pressure Bar used for High Strain Rate Materials Testing

By

Stephen Thomas Marais

A Dissertation Submitted to Fulfil the Requirements
for the Degree MSc (Engineering)

Department of Mechanical Engineering
University of Cape Town
Cape Town, August 2001

Abstract

As a result of increasing demand to improve analysis of manufacturing techniques and safety in structures, it is necessary to determine material properties at high strain rates. Conventional screw-driven or servo-hydraulic methods of testing materials at high strain rates are not adequate as oscillations and stress waves are set-up within the testing apparatus. These oscillations and stress waves foul the transducer reading, thus making the data obtained unusable. To overcome these limitations the split Hopkinson pressure bar (SHPB) was developed.

A SHPB facility was developed at UCT to measure material properties at high strain rates. The development, discussed in this thesis, included the design and manufacturing of a SHPB, strain gauge amplifiers and a data acquisition system. In addition to this a data processing package, including a dispersion correction routine was also developed.

From the development and testing on the system the following conclusions can be drawn. The system as a whole functioned well and enabled testing of different materials at various strain rates up to $10^3 s^{-1}$. The dispersion correction program used was able to shift the pulses to the specimen interface and substantially reduced the oscillations on the stress strain plot. In addition to this, the use of pulse shaping further reduced the oscillations.

The data acquisition system was able to sample at 20MHz and capture 24000 sample points per channel, thus making it more than adequate to capture the signal for the strain gauge amplifiers. The Visual Basic user interface for the data acquisition was user friendly and the operation was very similar to that of an oscilloscope, thus considerably reducing the time required to train an operator. The amplifiers developed were stable and had very low levels of noise on the output. They also gave sufficient gain to the signal to generate a stress-strain plot.

The calibration tests conducted were repeatable and the dynamic calibration factor only deviated from the theoretical calibration factor by 5%, thus reconfirming the

calibration of the system. The method for determining Young's modulus and Poisson's ratio of the bar was very successful, as the Young's modulus could be determined to within 1GPa and the Poisson's ratio to within 0.01.

The material models published in the literature did not correlate well with the actual test data but there was good correlation between published results. There could be two main reasons for this. Firstly, the material tests conducted showed that there is a large difference in the stress level of an as worked specimen and one that was annealed. Thus, the work hardening state and microstructure of the specimen could be the source of the discrepancy. Secondly, the value used for the constitutive constants in the model significantly altered the predicted stress level. As a result, the selection of the correct values for the constitutive constants is vital, if one is to obtain good correlation with the models.

As the SHPB system developed is fully functional and accurate, it is recommended that additional testing be done to determine the cause of the discrepancy between the test results and the material model. This should including noting the effects of work hardening, microstructure and temperature on the stress of the material. From these tests the constitutive models could be modified to be more representative of the material or a new model developed which incorporates work hardening characteristics as well as (earlier) strain rate parameters. During testing the incident pulse should be pulse shaped, as there is a considerable reduction in the oscillations on the stress-strain curve in so doing.

Declaration

I declare that this dissertation contains only my own original work, except where reference is made with acknowledgment to contributions from others. I also declare that this material has not been submitted for any purpose or examination to any other Department or University

Signed this.....22..... day of .....11- 2001.....

.....

Stephen Thomas Marais

Acknowledgements

I would like to extend my thanks to the following people for the assistance they provided during the course of my thesis. Their advice was invaluable to the successful completion of the project.

Prof. R.B. Tait who supervised the project and gave help and support at all times.

Prof. G. N. Nurick who co-supervised the project and gave help and support at all times.

T.J.Cloete who co-supervised the project. His insight and knowledge of the subject was invaluable.

Prof. J. Tapson for his time and help with the electronics.

All the workshop and administrative staff of the Department.

Family and friends for their support and encouragement during the course of the project.

Contents

List of Figures

List of Symbols and Abbreviations

A_0	Original cross-sectional area of the specimen	[m^2]
A_s	Instantaneous cross-sectional area of the specimen	[m^2]
A_{Bar}	Bar cross-sectional area	[m^2]
C_0	Fundamental wave speed	[m/s]
C_p	Phase velocity	[m/s]
C_g	Group velocity	[m/s]
d	Diameter of bar	[m]
E	Young's modulus	[GPa]
E_{Bar}	Energy of the pulse in the bar	[J]
f	Frequency	[Hz]
$f(t)$	Function in the time domain	
$F(\varpi)$	Fourier transform of a pulse	
I_{Bar}	Momentum of the pulse in the bar	[N.s]
l_0	Original length of the specimen	[m]
l_s	Instantaneous length area of the specimen	[m]
ϖ	Angular frequency	[rad/s]
m	Mass of the striker	[kg]
T	Period of the sample	[s]
u	Displacement	[m]
v	Velocity of a particle in the bar	[m/s]
Z	Distance the pulse is moved	[m]
ε	Strain	
$\dot{\varepsilon}$	Strain Rate	[s^{-1}]
σ_{s1}	Stress at the incident bar/specimen interface	[MPa]
σ_{s2}	Stress at the specimen/transmitter bar interface	[MPa]
ν	Poisson's ratio	
Λ	Wavelength	[m]
ρ	Density of the bar	[kg/m^3]

Subscripts

r	Reflective
i	Incident
t	transmitted

Abbreviations

DIHB	Direct impact Hopkinson bar
SHPB	Split Hopkinson pressure bar
FFT	Fast Fourier Transform
IFFT	Inverse Fast Fourier Transform

1

Introduction

This thesis sets out the details and results of the development and testing of a split Hopkinson pressure bar (SHPB) facility for the use of testing of materials to high strain rates typically up to $10^3 s^{-1}$. This forms part of an ongoing research project of the Centre for Research in Computational and Applied Mechanics (CERECAM) at the Department of Mechanical Engineering, University of Cape Town.

Experimental techniques have been developed to determine material properties at high strain rates as a result of increasing demand to improve manufacturing techniques and safety in structures. The following list highlights some of the applications where high strain rate material properties are needed:

- increase the rate of manufacture of products such as high-speed wire drawing, cold rolling, high-rate forging, shot-peening and shock welding
- defence applications including projectiles, armour and explosive or propellants, material interactions
- automotive crashworthiness
- cavitation and particulate erosion in turbines and marine propulsion
- aerospace impacts; including foreign object damage such as bird ingestion in jet engines, blade containment in engines, and meteorite impact on satellites
- the development of material models, such as the Cowper-Symonds[1] and Johnson-Cook[2], to characterise the behavior of materials at high strain rates for use in finite-element simulations

The conventional method of measuring the material properties is carried out by loading the specimen at a constant rate, in compression, tension or torsion, and recording the

load and deflection. From this, the engineering stress-strain property could be obtained. These testing machines are typically screw-driven or servo-hydraulic and owing to their construction they typically have an upper limit of strain rate of $1s^{-1}$. To obtain higher strain rates than this, specially designed high capacity servo-hydraulic machines are used and can achieve strain rates of $200s^{-1}$. At these strain rates, the conventional testing methods suffer from oscillations and stress waves being set up in the load cell by the rapid loading of the specimen. These oscillations and stress waves foul the reading obtained for the transducer and make them of questionable value and often unusable. Alternative testing techniques have to be used to overcome these limitations at higher strain rates.

To overcome the limitations on the conventional methods, the stress wave reflections within the load measuring device must be discriminated against. The most successful technique to achieve this has been the split Hopkinson pressure bar and is capable of achieving strain rates up to $2 \times 10^4 s^{-1}$ in compression[3][4][5][6]. The SHPB achieves this by using long impact bars which are strain gauged. The bars are sufficiently long that the incident and reflected stress waves can be separated and discrimination achieved. The Hopkinson bar technique has also been developed to test materials in tension [7][8][9][10][11] and torsion [12][13] but at lower strain rates. The split Hopkinson pressure bar has also been utilised to load samples to measure material fracture toughness [14][15][16] and to test specimens at elevated temperatures [17][18][19].

The objectives of this project have been to develop and test a SHPB for testing material at high strain rates in compression. The project considered the following developments:

1. setting up of the pressure bars and gas gun
2. design and construction of strain gauge amplifiers
3. sourcing of a data acquisition system
4. programming of a data processing system to correct for dispersion
5. make the abovementioned systems user friendly
6. to calibrate the system

7. perform compression tests on material specimens to generate stress-strain curves at different strain rates. These results are then to be compared to those of material models and values found in literature.

The report begins with a review of the relevant literature. It then goes on to describe the SHPB system and the tests that were to be conducted to validate the system. Next, the operation of the data processing program, that corrects for dispersion, is described. The calibration of each subsystem is reviewed and then calibration of the system as a unit is considered. The results of the material tests are then discussed along with the operation of the system. Finally, conclusions are drawn and recommendations made for future work.

2

Background and Theory

2.1 Introduction

As mentioned earlier the split Hopkinson pressure bar is one of the most popular techniques to measure material properties at high strain rate. This chapter goes through the background and theory for the split Hopkinson pressure bar. Firstly the origin of the name is briefly discussed, then the layout of the system is given. Next the compression test on the SHPB is discussed with the relevant one dimensional wave propagation theory necessary for the generating of the stress-strain curve. After that, the development of the data capture systems and data processing methods are discussed. The material models used for comparison with the test data are then described and finally concluding remarks are given.

2.2 Historical Background of the Naming of the SHPB

In 1914 Bertran Hopkinson studied the shape and evolution of stress pulse propagation in a long elastic metallic bar [20]. Davies[21] and Kolsky[22] continued the work of Hopkinson and, by using two Hopkinson pressure bars in series with a specimen sandwiched between, were able to measure the dynamic stress-strain response. Owing to the pioneering work of Hopkinson, the experimental apparatus using stress wave propagation in long rods to study material properties was named the split Hopkinson pressure bar (SHPB).

2.3 Principal of Operation

2.3.1 Layout of split Hopkinson pressure bar

A SHPB system, shown schematically in *Figure 2-1*, typically comprises of the following:

- a gas gun and associated control valving that can launch a striker, to produce a

controlled pulse in the incident bar,

- a speed trap to measure the speed of the striker. The speed is then used in the calibration of the system,
- two long symmetric bars, namely the incident bar and transmitter bar,
- bearing and alignment fixtures to allow the bars to move freely while retaining precise axial alignment,
- strain gauges mounted longitudinally on both bars to measure the stress wave propagation in the bars,
- associated amplifiers and data acquisition system to record the stress wave.

2.3.2 Compression testing with the split Hopkinson pressure bar

In the compression test a short cylindrical specimen is positioned between the incident and transmitter bars. A striker of the same material and cross-sectional area as the incident bar is launched at the free end of the incident bar. This sets up a longitudinal compressive incident pulse, designated σ_i, which travels down the incident bar and is recorded by the first strain gauge station. Once the pulse reaches the bar/specimen interface part of the pulse is reflected in the form of a tensile pulse, designated σ_r, and is recorded by the first strain gauge station. The remainder of the pulse passes through the specimen where some of the energy of the pulse is absorbed by the specimen and then passes into the transmitter bar. The pulse travels down the transmitter bar ,designated σ_t, and is then recorded by the second strain gauge station.

The shape of the incident pulse can be varied in length and amplitude by varying the striker length and impact velocity. By altering the shape of the incident pulse the strain and strain rate of the specimen can be varied. For a given striker length, the strain rate can be increased by increasing the impact velocity of the striker. As the bars should not go plastic the maximum allowable impact velocity $v_{\max}$ is [12]

$$v_{\max} = \frac{2C_0\sigma_y}{E} \tag{2.1}$$

were σ_y is the yield stress and E is the Young's modulus of the pressure bar, C_0 is the fundamental longitudinal wave velocity. The strain that the specimen undergoes is increased by increasing the length of striker. The length of the striker must always remain less than half the length of the shorter pressure bar. This will avoid any overlap of the incident and reflected pulse at the recording station.

From the three readings (σ_i, σ_r and σ_t) it is posible to determine the time dependent stress state of the bar and, using one dimensional wave propagation theory, a stress-strain plot of the specimen can be obtained. A typical plot of the three recorded strain gauges reading is shown in *Figure 2-2 a.* with the calculated stress-strain plot shown in *Figure 2-2 b.* The one dimensional wave propagation theory needed to determine the stress-strain plot is discussed in the next section.

2.4 One Dimensional Wave Propagation Theory

Wave propagation behavior for elastic bars is well understood and mathematically predictable [23] [24] [25]. An schematic diagram of the SHPB showing the stresses in the bar is shown in *Figure2-3.*

From elementary wave theory the wave equation can be shown to be[7] [12] [26]

$$\frac{\partial^2 u}{\partial x^2} = \frac{1}{C_0^2} \cdot \frac{\partial^2 u}{\partial t^2}, \tag{2.2}$$

where $C_0 = \sqrt{\frac{E}{\rho}}$ is the fundamental longitudinal wave velocity, u is the displacement and t the time. The general solution to the wave equation can be written as

$$u = f(x - C_0 t) + g(x - C_0 t) = u_i + u_r \tag{2.3}$$

Considering the wave moving in the positive x direction, then the general solution becomes

$$u = f(x - C_0 t). \tag{2.4}$$

Then by differentiating *Equation 2.4* with respect to x the 1-D strain is given by

$$\varepsilon = \frac{du}{dx} = f' \tag{2.5}$$

and differentiating *Equation 2.4* with respect to t the velocity is given by

$$v = \frac{du}{dt} = -C_0 f' \tag{2.6}$$

where $(')$ denotes the differentiation with respect to the argument $(x - C_0 t)$.

Thus by substituting *Equation 2.5* into *Equation 2.6* we get

$$\frac{\partial u}{\partial t} = -C_0 \frac{\partial u}{\partial x}$$

or

$$v = -C_0 \varepsilon \tag{2.7}$$

Substituting $\sigma = E\varepsilon$ and $E = C_0^2 \rho$ in we can rewrite as

$$v = -C_0 \frac{\sigma}{E} = -\frac{\sigma}{\rho C_0} \tag{2.8}$$

giving

$$\sigma = -\rho C_0 v \tag{2.9}$$

The negative sign indicates that the tensile pulse is moving in the positive x direction, but it is conventional in wave theory to take compressive stresses positive thus

$$\sigma = \rho C_0 v \tag{2.10}$$

The velocities of a particle in the bar due to the incident pulse, the reflected pulse and the transmitted pulse are Δv_i, Δv_r and Δv_t respectively and can be written as

$$\Delta v_i = \frac{\sigma_i}{\rho C_0}, \; \Delta v_r = -\frac{\sigma_r}{\rho C_0} \text{ and } \Delta v_t = \frac{\sigma_t}{\rho C_0}$$

Note the negative sign for the reflected pulse is because the pulse is travelling in the

negative x direction.

From this, the velocity at the end of the incident bar, at bar/specimen interface, can be determined.

$$v_1 = \Delta v_i + \Delta v_r$$

giving

$$v_1 = \frac{1}{\rho C_0}\left(\sigma_i - \sigma_r\right). \tag{2.11}$$

By integration the velocity the displacement of the end of the bar can be determined.

$$\begin{aligned} u_1 &= \int_0^t v_1 dt \\ &= \frac{1}{\rho C_0}\int_0^t \left(\sigma_i - \sigma_r\right) dt \end{aligned} \tag{2.12}$$

Similarly the displacement of the transmitter bar at the specimen/bar interface can be determined.

$$u_1 = \frac{1}{\rho C_0}\int_0^t \sigma_t \, dt \tag{2.13}$$

Now that the displacement of the two bars can be calculated, the true strain of the specimen can be found. The true strain is

$$\begin{aligned} \varepsilon_{true} &= \int_{l_0}^{l} \frac{dl}{l} \\ &= \ln l - \ln l_0 \\ &= \ln\left(\frac{l}{l_0}\right) \end{aligned} \tag{2.14}$$

and the instantaneous length of the specimen is

$$l_s\left(t\right) = l_0 - u_1\left(t\right) + u_2\left(t\right), \tag{2.15}$$

then the true strain in the specimen with respect to time is

$$\begin{aligned}\varepsilon(t) &= \ln\left(\frac{l_s(t)}{l_0}\right) \\ &= \ln\left(\frac{l_0 - u_1(t) + u_2(t)}{l_0}\right) \\ &= \ln\left(1 + \frac{u_2(t) - u_1(t)}{l_0}\right).\end{aligned} \tag{2.16}$$

Differentiating the strain with respect to time gives the strain rate in the specimen

$$\frac{d\varepsilon}{dt} = \frac{d}{dt}\left(\ln\left(\frac{l_s(t)}{l_0}\right)\right)$$

$$\dot{\varepsilon} = \frac{1}{\left(\frac{l_s(t)}{l_0}\right)}\frac{d}{dt}\left(\frac{l_s(t)}{l_0}\right)$$

$$\dot{\varepsilon} = \frac{v_1 - v_2}{l_s(t)}. \tag{2.17}$$

The true stress can be obtained by assuming incompressible plasticity, in which case $A_0.l_0 = A_s l_s$ where A_0 is the original cross-sectional area, and A_s is the instantaneous cross-sectional area.

Then the instantaneous area of the specimen is

$$A_s(t) = \frac{l_0 A_0}{l_s(t)}. \tag{2.18}$$

The stress at the incident bar/specimen interface is

$$\sigma_{s1} = \frac{(\sigma_i - \sigma_r) A_{Bar}}{A_s(t)}, \tag{2.19}$$

and the stress at the specimen/transmitter bar interface is

$$\sigma_{s2} = \frac{\sigma_t A_{Bar}}{A_s(t)}. \tag{2.20}$$

Note that once the ringing up of the specimen is complete and the specimen has attained a stable stress state then $\sigma_{s1} = \sigma_{s2}$.

2.5 Development of Data Capturing and Processing

The central challenge in SHPB operation has always been to obtain reliable stress wave measurements. This section discusses the development of the data capturing and processing of the signals from the SHPB.

The first work by Davies (1947)[21] and by Kolsky (1949)[22] used cylindrical condenser microphones, and capacitive sensors mounted on the bars to measure the stress wave propagation. The signal was amplified and fed into a cathode ray oscilloscope. The amplifier used, No. 234 Pulse Amplifier, was developed by the Telecommunications Research Establishment and had a maximum gain of 3000. The amplifier was constructed using valves which limited the frequency response. Along with the signal from the amplifier, a sinusoidal wave was fed into the second channel. This signal was used to provide a reference timing trace. When the pulse was applied to the bar, by either explosive loading or by projectile, an inertia switch mounted on the bar would trigger a camera to photograph the trace generated by the oscilloscope. The film was developed and photograph enlarged so that the trace could be used to generate a stress-strain curve for the material tested.

The analysis of the results from the split Hopkinson pressure bar was based on the assumption that one- dimensional wave theory was adequate. To improve the accuracy of the analysis of the test results, the dispersion of the wave had to be considered. The dispersion of the pulse meant that the higher frequency components of the pulse travel slower in the bar than the low frequency components. This meant that the pulse "broke up" at it moved down the bar. This is overcome by correcting the signal for dispersion using the Pochhammer-Chree curves.

The solution to the equation of motion for the wave propagation in an infinitely long cylindrical bar was solved by Pochhammer (1876) and independently by Chree (1889). The solution relates the propagation velocity C_p to the wavelength Λ and is exact only for an infinitely long cylinder. An excellent summary of the Pochhammer-Chree solution has been given by Love [27]. The full generation of the Pochhammer-Chree modes is discussed in detail in *Section 4.2*, as part of the data processing program, as it is more appropriate there.

The first Pochhammer-Chree mode is shown in *Figure 2-4* and from the graph it can be seen that as the frequency of the individual components of the pulse increases, the phase velocity deceases. To illustrate the breakup of the pulse due to the dispersion, a trapezoidal shaped pulse was assumed to be initiated at the end of the pressure bar. The pulse was then allowed to travel 500mm down a ϕ20mm bar and to disperse according to the first Pochhammer-Chree mode as can be seen in *Figure 2-5*. It can also be seen in *Figure 2-5* that the low frequency components of the pulse stay within the main body, whereas the high frequency components form a "tail" at the rear of the pulse. What is also evident, as a result of the separation of the frequencies, is the oscillations of the main body of the pulse. These oscillations result in oscillations on the stress-strain curve which distort the true stress-strain state of the specimen.

Davies [21] applied the numerical results calculated from the Pochhammer-Chree equation to determine the dispersion of a wave travelling in a bar. He assumed that the pulse initiated at the end of the bar was trapezoidal and periodic. From this he expressed the periodic wave by a Fourier series and let each component travel with its phase velocity. Davies' investigations showed that it was possible to reconstruct a dispersive stress wave in a long cylindrical bar with prior knowledge of the diameter, Young's modulus, Poisson's ratio and the density of the bar. He also showed that the wave propagation belonged predominantly to the first mode of vibration. This investigation method was time consuming at the time as all the calculations were performed manually. The number of Fourier terms were also limited which reduced the resolution of the corrected wave. Despite the computational limitations, he was able to show that the wave propagation belonged to the first mode of vibration. In 1958 Hsieh and Kolsky [28] used a simpler method to confirm Davies work.

The development of the transistor and the improvement of computational equipment, made it possible to use Fast Fourier Transform (FFT) analysis technique [29]. The FFT algorithm is used to transform the time domain data to the frequency domain. The final result is a complex expression of the magnitude and phase of each of the frequencies in the time domain data. In 1978 Yew and Chen [30] captured the wave at two locations in a cylindrical aluminum rod simultaneously with an oscilloscope (by photographing the

image) and a transient recorder. From the two readings at separate locations with the use of the FFT, they were able, experimentally to plot the phase velocity. Their results showed good correlation to the theoretical phase velocity generated from the first Pochhammer-Chree dispersion curve.

In 1983, Gorham[31] significantly reduced the oscillation on the generated stress-strain curve. The signal from the pressure bar was digitized, at a sample rate of $20MHz$, and processed using the FFT algorithm on a HP9825 computer. Once the data was transformed he corrected the phase shift using tabulated data generated by Bancroft (1941). The Inverse Fast Fourier Transform (IFFT) was then used to reconstruct the pulse to the time domain. This method was significantly different from the former methods as it did not use the assumption that the wave was trapezoidal and periodic. This meant that pulses that are not trapezoidal in shape, such as those generated from explosive detonation, could be corrected for.

Even though the method used by Gorham reduced the oscillation on the stress-strain curve it had not been removed completely. Lipshitz and Leber (1994) investigated the source of these oscillations by noting the effect of small errors in the value used for the fundamental wave speed $C_0 = \sqrt{\frac{E}{\rho}}$ where E = Young's modulus and ρ = density of the bar. This was achieved by measuring the stress pulse in a bar at two locations and then shifting the reading of the first pulse to the second with the correction for dispersion. They used the method proposed by Gorham to correct for the dispersion but they used several values close to the correct fundamental wave speed to note the effect. They showed the an error of only 1% in the fundamental wave speed could significantly increase the oscillation on the stress-strain curve.

So far the dispersion correction used the Pochhammer-Chree solution for the propagation of the wave, but this solution is only exact for bars of infinite length. Lee and Crawford (1993)[32] developed a method to measure the phase velocity of the stress pulse. The first version of the method used only one Hopkinson pressure bar and a sphere of high explosives was detonated at one end. The recorded signal was then analyzed with the rectangular-window Fourier transform technique to obtain the time-dependent Fourier

coefficients from a measured signal. From this the phase velocities were obtained. These phase velocities took into account the time of arrival of each frequency, thus gaining a better representation of the actual phase velocity. The corrected phase velocities were then used to correct for the dispersion of the pulse. The pulse measure was shifted to the loaded end of the bar and corrected for dispersion. The new trace of the pulse was compared to the method used by Gorham, and it was shown that the peak was far more defined. There were also less oscillations ahead of the pulse indicating that the correct phase velocity had been used. This new method was more computationally costly, as 3000 data points were processed on an IBM 486 and the new method took 30 minutes to analyse, whereas the Gorham method took 3 minutes.

The use of a rectangular-window in the Fourier transform meant that the higher frequencies were filtered out and any higher modes of vibration present were lost. Lee and Crawford (1995)[33] then used the Gaussian-window Fourier transform technique to experimentally measure the Pochhammer-Chree dispersion curves. The same setup was used as in their previous experiment, but the signal was sampled by a high speed, high resolution data recorder (sample rate of 10MHZ, sample size of 10000 and 12 bit resolution). The transformed data showed the presence of four modes of vibration. The Pochhammer-Chree analytical solution and the transformed data were then used to generate the new semi-empirical dispersion curve for the stress wave propagation in the bar. This new dispersion curve was then used to shift the pulse to the loaded end of the bar. This method was compared to the method used by Gorham and it was noted that the rise time of the explosion was higher with the new method. The peak was also more defined and there were no oscillations preceding the pulse.

2.6 Material Behavior at High Strain Rate

It is well established that the material flow stress is sensitive to the strain rate and is known as the material strain rate sensitivity [1][2][34][35]. The flow stress being the stress level that leads to macroscopic, non recoverable strain. Not all materials have the same strain rate sensitivity, for example mild steel has a high strain rate sensitivity, where as

aluminium 6061-T6 is essentially strain rate insensitive[1][36]. The increase in strain rate tends to increase the yield point and flow stress of the material. This increase in yield point is well illustrated in *Figure 2-6*, extracted from Jones [1], where the dynamic lower yield point divided by the static lower yield is plotted for mild steel at different strain rates. The graph also shows the wide scatter in the data that different authors have published.

2.7 Material Models

Numerical models representing the behavior of materials have been extensively used in finite-element simulations. For any of these models the desirable feature would be to be able to characterize the material with a limited number of laboratory tests so that the simulations could be used with more confidence. Two of these numerical models are discussed below, these being the Cowper-Symonds [1] and Johnson-Cook model [2]. These two models were selected as they are well established in the literature and used extensively in many of the finite-element computer programmes[37]. The constitutive constants used in the model are however not always available for the specific material under consideration especially as a function of its microstructure and degree of cold working or work hardening. For this reason the Cowper-Symonds model will be used for comparison of the mild steel test data and the Johnson-Cook model for the copper test data.

2.7.1 Cowper-Symonds Constitutive Equation

In 1957 Cowper and Symonds introduced their constitutive equation (*Equation 2.21*) [1] to characterize the effect of strain rate on material properties. Their model was formulated by gathering test data of the dynamic lower yield stress of various materials at different strain rates. From the data a best fit curve was generated and constitutive constants for *Equation 2.21* were generated. From the material coefficients (D and q) the stress-strain curve of a material at a known strain rate could be scaled to determine the material properties at an unknown strain rate.

$$\frac{\sigma_0'}{\sigma_0} = 1 + \left(\frac{\dot{\varepsilon}}{D}\right)^{1/q} \tag{2.21}$$

where

- σ_0' was the dynamic flow stress at a uniaxial plastic strain rate $\dot{\varepsilon}$.
- σ_0 was the associated static flow stress ($\dot{\varepsilon} = 0.004s^{-1}$)
- D and q were constants for a particular material

The Coefficients for various materials are given in *Table 2.1* and were extracted from Jones publication [1].

Table 2.1 Coefficients of *Equation 2.21*

Material	D $[s^{-1}]$	q
Mild steel	40.4	5
Aluminium alloy	6500	4
Aluminium 6061-T6	1288000	4
α-Titanium (Ti 50A)	120	9
Stainless Steel 304	100	10

From *Equation 2.21* it can be seen that $\sigma_0' = 2\sigma_0$ when $\dot{\varepsilon} = D$, regardless of the value of q. Thus, the dynamic flow stress of mild steel doubles at a strain rate of $40.5s^{-1}$, while the aluminium alloy requires a strain rate of $6500s^{-1}$ to double its dynamic flow stress.

The data gathered to determine the constants for the model had a large scatter. Jones [1] gathered some of this test data and compared it to the Cowper-Symonds constitutive model with constants of $D = 40.4s^{-1}$ and $q = 5$. A copy of the graph generated by Jones is shown in *Figure 2-6*. From the comparison plot it can be seen that the model correlates relatively well with the test data at low strain rates, but deviates substantially at the high strain rates. Other values for D and q for mild steel are listed by Abramowicz [38] with constitutive constants of $D = 802s^{-1}$ and $q = 3.585$ which are substantially different for those listed by Jones. This discrepancy in the constitutive constants are believed to be due to the different type of mild steel tested, the difference in grain size, the heat treatment, amount of work hardening during steel making as well as machining of the specimen, and the variety of testing machines and data recording equipment used. In addition to these

factors, the model does not take into account the effect of increase in temperature which could also affect the accuracy of the model.

2.7.2 Johnson-Cook Constitutive Equation

The Johnson-Cook model was introduced in 1983 [2] and was primarily intended for computational work. The model was formulated by gathering test data at different strain rates and temperatures for a wide range of test procedures. The following set of procedures was used:

1. Tensile tests were performed both at low strain rates on conventional tensile testing equipment and at high strain rates on a split Hopkinson pressure bar system. The stress was based on the current area of the neck, and the strain was defined as $\ln(A_0/A)$ were A_0 and A represent the initial and current areas of the neck respectively. At large strains when necking began, the tensile test data was approximately determined by the using the Bridgman correction factor [39].

2. Torsion test data were obtained [40][41] and the equivalent tensile flow stress was obtained by using von Mises flow rule, the tensile stress is $\sigma = \sqrt{3}\tau$.

From these tests the model was expressed as

$$\sigma = [A + B\varepsilon^n][1 + C\ln\dot{\varepsilon}^*][1 - T^{*m}] \tag{2.22}$$

where

- ε is the equivalent plastic strain, $\dot{\varepsilon}^* = \dot{\varepsilon}/\dot{\varepsilon}_0$ is the dimensionless plastic strain rate for $\dot{\varepsilon}_0 = 1.0s^{-1}$.
- T^* was the homologous temperature $\left(T^* = \frac{T - T_{ROOM}}{T_{MELT} - T_{ROOM}}\right)$
- A is the yield stress
- B and n represent the effects of strain hardening
- C is the strain rate constant

- m is the thermal softening fraction

From *Equation 2.22* it can be seen that the first set of brackets gives the stress as a function of strain. The second set of brackets represents the effects of strain rate and the third the effect of temperature.

The constitutive constants for *Equation 2.22* were determined for the following materials and can be found in [2] and in *Table 2.2* : OFHC copper, Cartridge brass, Nickel 200, Armco iron, Carpenter electrical iron, 1006 steel, 2024-T351 aluminum, 7039 aluminum, 4340 steel, S-7 tool steel, Tungsten alloy (0.07Ni, 0.03Fe) and DU-0.75Ti. Other Material constants can be determined but this requires rigorous material testing.

Tabel 2.2 Constitutive Constants for the Johnson-Cook model

Material	Constitutive Constants for Equation 2.22				
	$A\ [MPa]$	$B\ [MPa]$	n	C	m
OFHC copper	90	292	0.31	0.025	1.09
Cartridge brass	112	505	0.42	0.009	1.68
Nickel 200	163	648	0.33	0.006	1.44
Armco iron	175	380	0.32	0.060	0.55
Carpenter electrical iron	290	339	0.40	0.055	0.55
1006 steel	350	275	0.36	0.022	1.00
2024-T351 aluminum	265	426	0.34	0.015	1.00
7039 aluminum	337	343	0.41	0.010	1.00
4340 steel	792	510	0.26	0.014	1.03
S-7 tool steel	1539	477	0.18	0.012	1.00
Tungsten alloy (0.07Ni, 0.03Fe)	1506	177	0.12	0.016	1.00
DU-0.75Ti	1079	1120	0.25	0.007	1.00

Note that all that is needed to determine the material property at a given strain, strain rate and temperature are the correct values of the constitutive constants. This makes this model ideal for use in finite-element simulations. One of the limitations of this model is that

it does not take into account the initial state of the specimen. Therefore, for a specimen that is machined and then annealed would be predicted, using the Johnson-Cook model, to have the same stress-strain response as one that is not annealed and which could be already extensively work hardened. An example of the stress-strain curve, generated using the Johnson-Cook model, for copper at strain rates from $0.001s^{-1}$ to $10\ 000s^{-1}$ is given in *Figure 2-7*. It can be seen from *Figure 2-7* that copper is strain rate sensitive

2.8 Concluding Remarks

This chapter has provided some background of the effects of high strain rate on material behavior, as well as on the SHPB system, both from an historical as well as a theoretical stand point.

The two material models described above have vastly different methods for characterizing the material properties. The selection of the material model used depends on whether the model has coefficients of the material under consideration, or whether laboratory tests are required to be conducted to determine these coefficients. Another factor is that different models give better correlation with actual test results than with others.

With the need for a better understanding of material behavior at high strain rates, so that the finite-element simulations of components and structures can be improved, it is necessary to develop a facility that can test materials at high strain rates, but with substantially increased accuracy. This is now possible as a result of the increase in the electronic capability and computational power available for data analyses. It is more convenient now to process the data in the frequency domain using the FFT. This is also more effective than working with the time domain. The shape of the dynamic stress strain curve is very sensitive to small errors in the value of C_0, which means that accurate values for Young's modulus and the density of the bar have to be determined. The first mode of vibration dominates the propagation of the wave, but the higher modes do contribute to the shaping of the pulse.

The chapters which follow deal precisely with the setting up of an exceptionally accurate SHPB facility to test materials at high strain rates which ultimately leads to comparison of

experimental results with the behavior predicted by the models. in this way it is believed a significant contribution can be made to the understanding of material behavior at high strain rates, and a technique of improving models.

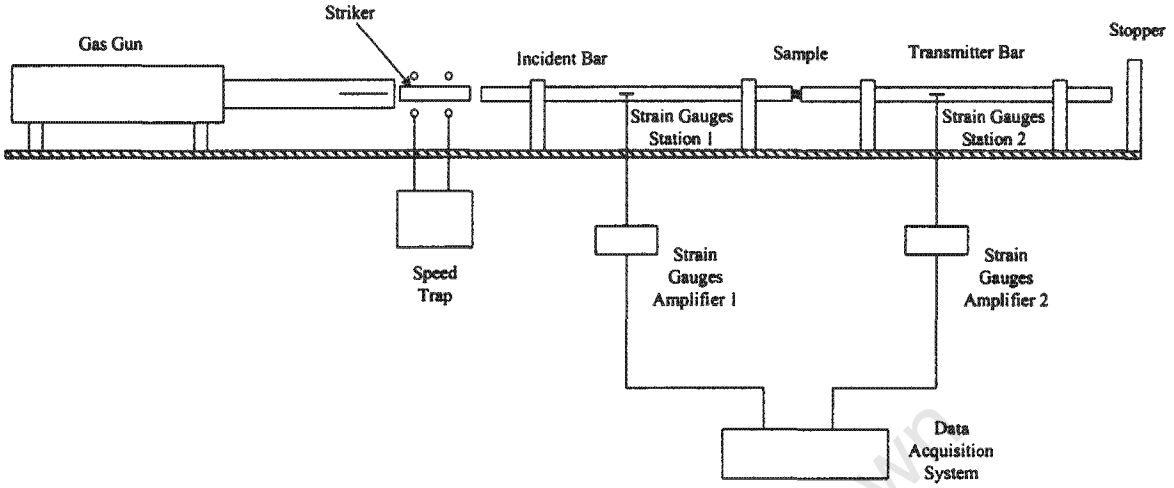

FIGURE 2-1. Schematic diagram of the split Hopkinson pressure bar test apparatus.

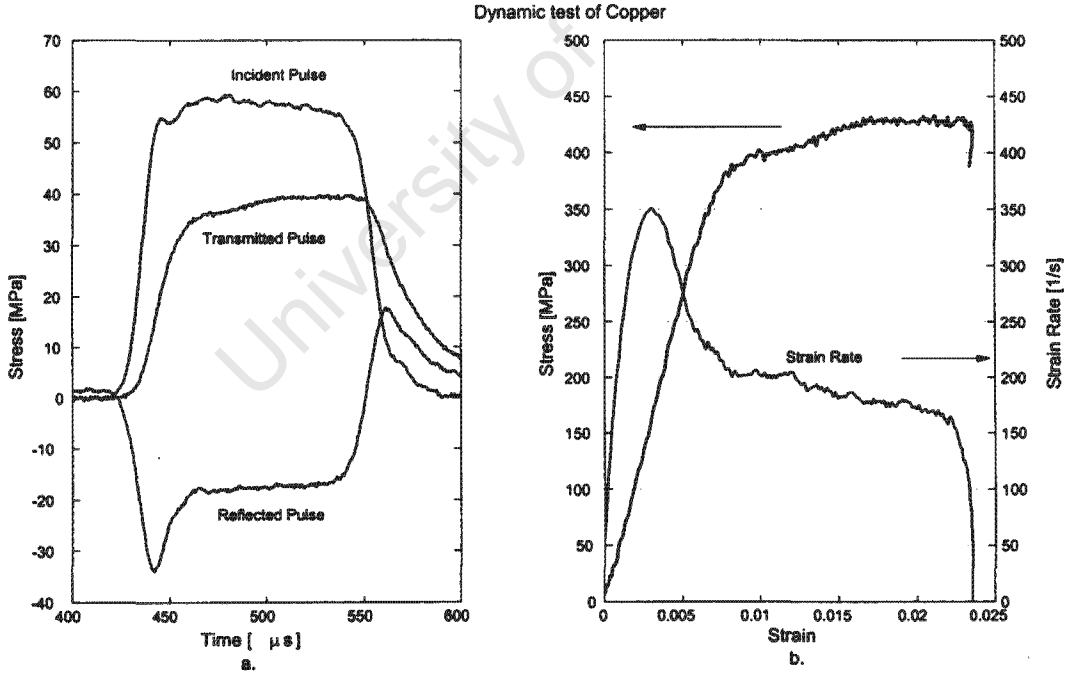

FIGURE 2-2. Copper test showing a.) the stress reading in the bar and b.) the Stress-strain and strain rate plot.

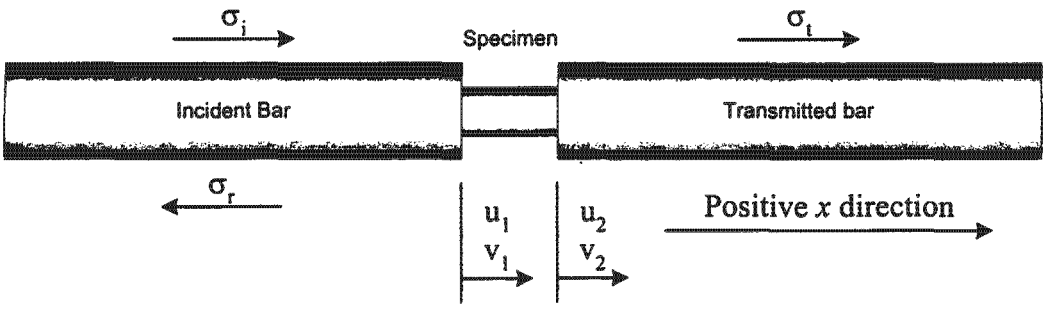

FIGURE 2-3. Schematic of the SHPB showing the stresses in the bar

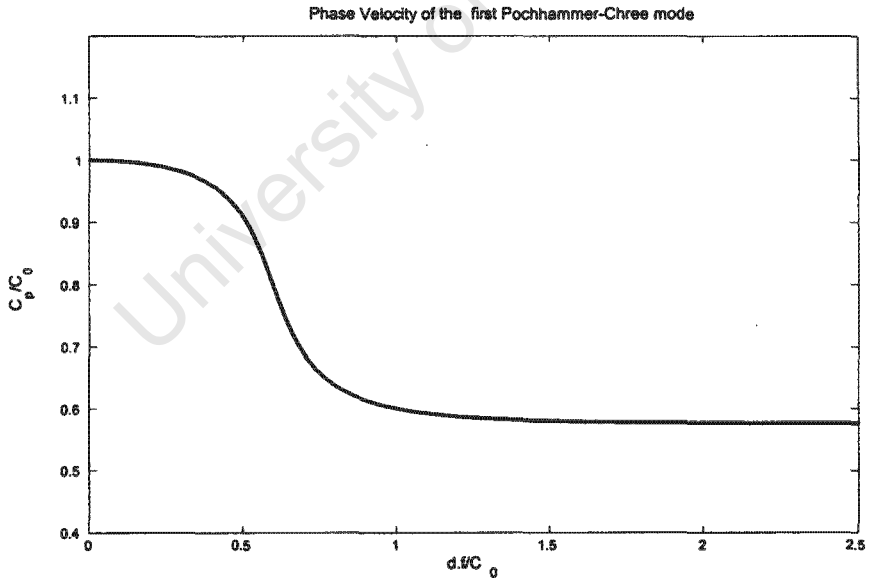

FIGURE 2-4. Phase Velocity of the first Pochhammer-Chree mode

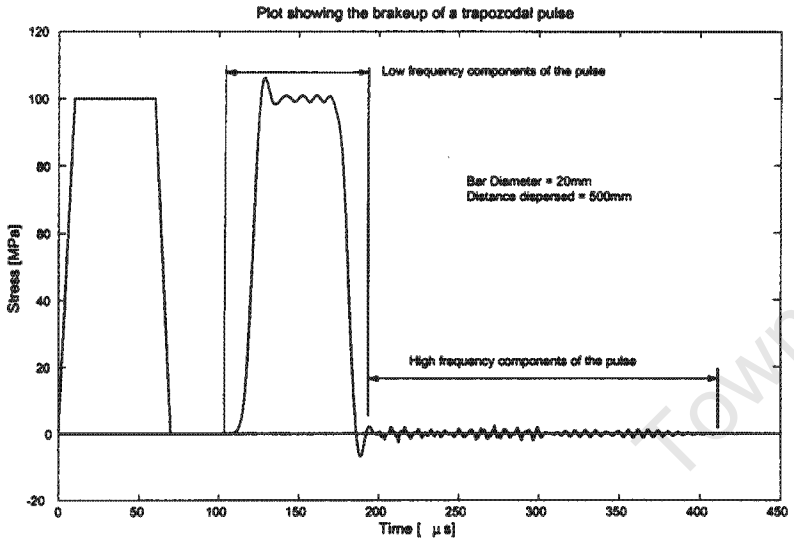

FIGURE 2-5. Plot showing the breakup of a trapezoidal pulse due to dispersion.

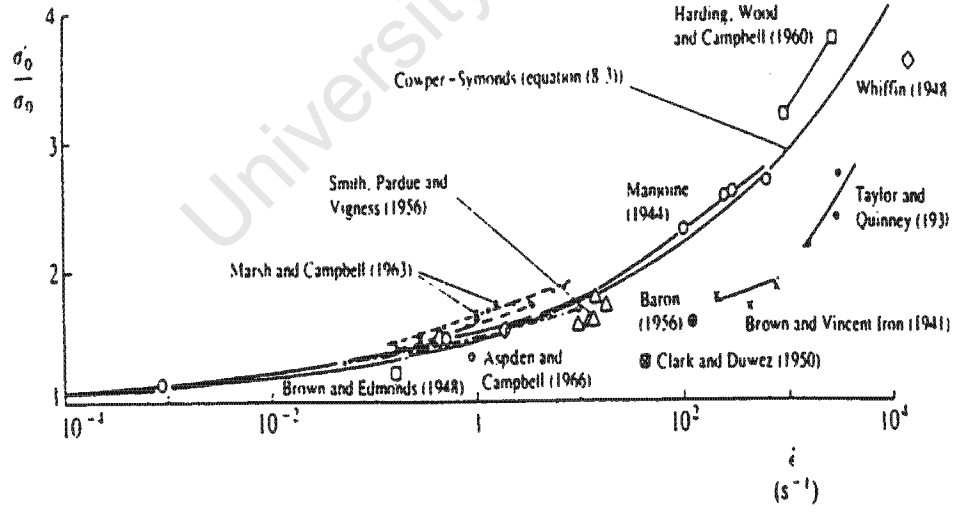

FIGURE 2-6. Extracted figure from Jones [1] showing the effect of increasing strain rate on the yield point of mild steel. Also note the relatively large scatter in the results. Details of the references in this figure can be obtained from Jones original publication [1].

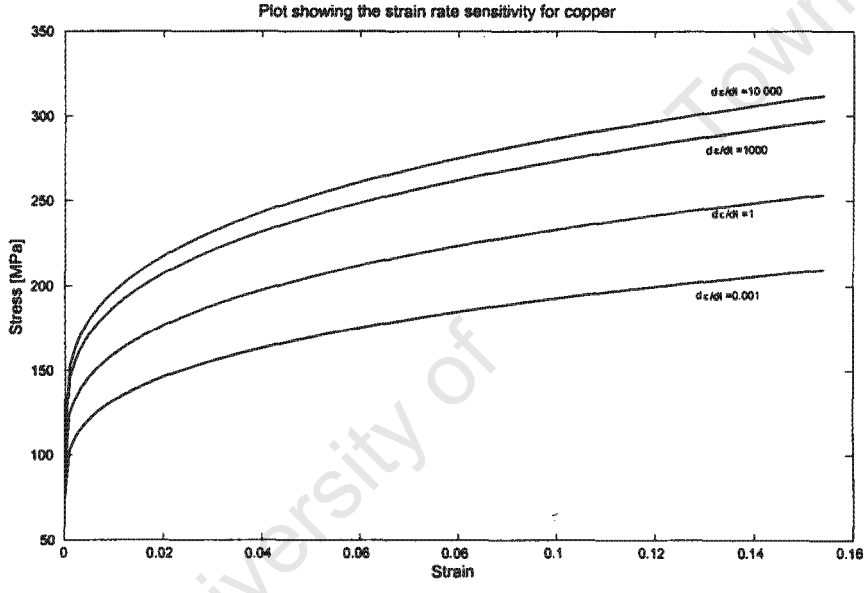

FIGURE 2-7. Plot showing the strain rate sensitivity of copper using the the Johnson-Cook model

3

Experimental Details

3.1 Introduction and Overview of the Operation of the SHPB system

As mentioned earlier, standard tensile test machines are not suitable for measuring material properties at high strain rates, as stress waves set up by the rapid loading of the specimen propagate through the entire system thus fouling the transducer readings. To overcome these limitations of conventional testing, the split Hopkinson pressure bar (SHPB) has been developed for high strain rate applications.

Figure 3-1 and *Figure 3-2* provide a schematic and photograph representation of the split Hopkinson pressure bar (SHPB) system. The SHPB system operates as follows. The test specimen is placed between the two bars. The gas gun launches a striker bar that impacts upon the end of the incident bar. A stress wave is generated which travels down the bar and is recorded sequentially by the first and second strain gauges mounted longitudinally on the bar. The stress wave then passes through the specimen and the specimen is compressed. Part of the stress wave is reflected in the form of a tensile pulse and is recorded by the second strain gauge. Part of the wave energy is absorbed by the specimen and the remainder is transmitted to the transmitter bar and recorded by the third strain gauge similarly mounted. The three readings are used to determine the time dependent stress state of the specimen. The time dependent strain state data is processed and a stress-strain plot is obtained.

In this chapter the components comprising the experimental apparatus are discussed. This includes mechanical components, the electronics used to measure the signal and the data acquisition system. The procedure for performing a test is described and finally the testing program used to validate the SHPB is discussed.

3.2 Experimental Equipment

3.2.1 Original Setup of Equipment

The gas gun and stand were originally designed for use in ballistics testing. The gas gun was designed to fire projectiles at speeds up to $150m/s$ rather than the relatively low speeds that an SHPB requires. The main beam on which the original gas gun was mounted was also too short for SHPB purposes, as it was simply used to support a target, and not long enough to mount the two bars. The system also did not have any data logging facilities as visual measurement and evaluation were used in previous experiments . An exception to this was the relatively crude electronic system used to measure the speed of the projectile, which was mounted on wooden blocks.

3.2.2 Layout of the Current SHPB

3.2.2.1 Modification to the frame

A separate frame was manufactured to support the gas gun so that the main beam could be used to support the two bars (*Appendix D*). The gas gun frame was bolted to the main beam so as to make a single unit with a coupling between the two. As there would be some flexibility in the coupling between the gas gun frame and the main beam, the gas gun frame was fitted with adjustable feet. This also aided in the alignment between the frame and the main beam. *Figures 3-2* and *3-3* show the layout of the current system. From the photograph one can see the gas gun on the left, the original main support beam and the coupling between them. Originally the frame was going to be mounted directly to the main beam, but additional length was required to make the two bars as long as possible. Two bright mild steel strips were run along the length of the beam to provide a surface on which to mount the bar supports.

3.2.2.2 Modification to the gas gun and control valving

As the original system was mainly run at high pressures, the gauges on the regulator, that measured the pressure in the primary cylinder, was not sensitive enough to display the low end pressures (up to 10 bar). Full scale deflection for the pressure regulator was 300 bar. For this reason an additional gauge was installed into the line between the pressure

regulator and the primary cylinder, *Figures 3-4* and *3-5*. This pressure gauge had a full scale deflection of 30 bar to accommodate testing at low pressure for the SHPB and for the slightly higher pressures needed for direct impact Hopkinson bar (DIHB) tests, an additional complication of the system. An isolator valve was installed to protect the pressure gauge from over pressurising when the system was run at full pressure for ballistic tests. A bleed off valve was also installed for the primary cylinder to allow for finer setting of the pressure and to accommodate the post test draining of the primary cylinder.

3.2.2.3 Barrel alignment and support system

To accommodate alignment of the barrel with the incident bar a barrel alignment system was manufactured and installed. This system also supported the barrel and can be seen in *Figure 3-6*. The alignment of the barrel with the incident bar was achieved by placing the striker in the barrel so that it protruded slightly and then adjusting the four bolts until the striker and bar were aligned. Visual inspection was used to determine the alignment of the barrel with the bar.

3.2.2.4 Limitation of the striker diameter

The internal diameter of the barrel was only 12.7mm. Sourcing a larger barrel was not possible given the time and budget constraints. It was decided to use the small barrel even though this would limit the striker diameter. The striker diameter was therefore limited to 10mm giving space around the striker for a sealing ring.

3.2.2.5 Operation of the gas gun and control valves

In order to charge the gas gun for testing, the trigger cylinder was pressurised to 110% of the primary cylinder pressure. The required pressure was then introduced into the primary cylinder. The striker was loaded into the barrel, with the aid of a plunger, to the required depth. The combination of pressure and depth of the striker determined the final exit velocity of the striker. Once the specimen was in place, the trigger circuit was activated which opened the trigger valve and allowed the primary cylinder to discharge. When all testing was finished the system was depressurised.

A step by step guide for the operation on the gas gun is given in *Appendix C*.

3.2.2.6 Bar support method

The bars are supported as shown in *Figure 3-7*. A Teflon bush was used to reduce the sliding friction and provide maximum impedance mismatch between the bar and the support. In doing so noise from the bar support was minimised. The alignment of the bar was achieved by adjusting the eight setting bolts. Horizontal adjustment was achieved by adjusting the four horizontal bolts to push up on the edge of the flange of the support beam. When the horizontal adjustment was completed all four bolts were tightened down to lock the support in place. Vertical alignment was achieved in a similar manner using the four vertical bolts.

3.2.3 Electronics used with the SHPB

3.2.3.1 Speed trap sensor

The speed of the striker was measured by two infrared transmitter/receiver sets mounted on the barrel *(Figure 3-6)*. When the striker gets to the end of the barrel it breaks the infrared signal of the first and second traps sequentially. The signal from the infrared receivers is electronically cleaned up to output a digital pulse ($0V$ or $+5V$). The signal was then fed into a *FLUKE 7250* timer where the time between the positive edge of each pulse was displayed on a digital readout. The gap between the two transmitter/receiver sets was determined (see *Section 5.4*) and by dividing the gap length by the recorded time the speed was determined.

3.2.3.2 Preliminary strain gauge bridge amplifiers configurations

As the data acquisition card (*Section 3.2.4*) required a maximum input signal of $\pm 5V$, the strain gauge bridge amplifier had to provide sufficient gain to utilize the full (12 bit) range of the card. Two approaches could be used to adjust the gain. Firstly, using a digitally programmable gain amplifier such as the Burr-Brown PGA 103 and secondly, to use an instrumentation amplifier with fixed gain and adjust the strain gauge bridge voltage. The latter approach was adopted because acquisition of the PGA would require a significant delay for delivery.

3.2.3.3 Layout of final strain gauge bridge amplifiers

A gain of 1000 was needed to obtain a full scale defection of $\pm 5V$ at a stress in the bar of 100MPa, for a bridge voltage of $\pm 5V$. To get this gain and to keep the circuit as simple as possible, two Burr-Brown INA110 fast settling instrumentation amplifiers were used. The first amplifier was set to a gain of 100 and the second one set to a gain of 10. The gain of the first amplifier was chosen to ensure maximum common mode rejection and still have sufficient gain at the higher frequencies. *Figure 3-8* shown the layout of the strain gauge bridge amplifier. Internal noise of the system was minimised by using as few components as possible. The final circuit was built in vera-board and is shown in *Figure 3-9*.

The strain gauges were connected in a full bridge configuration, with the two gauges mounted on the bar wired to compensate for both bending in the bar as well as temperature. The strain gauges used were KYOWA type KFG-2-120-C1-11. The other two strain gauges of the full bridge were glued onto a heat sink and mounted in the amplifier box. As the amplifiers were mounted next to the bar there would be little temperature difference between the two sets of strain gauges. If there were any temperature difference the level of the input signal would change. This would not effect the reading and the signal was zeroed in the data processing program (*Section 4.4.2.3*). The leads from strain gauges mounted on the bars were fed into the amplifier by a 9 pin D-type plug. The 9 pin D-type plug had gold plated pins to ensure a good connection. The cable from the strain gauges to the amplifier was screened and grounded at the amplifier.

Two separate power supplies were used, one for powering the amplifiers and the second for the strain gauge bridge. The leads for the power supplies were also screened and grounded at the amplifier.

The output for the amplifier to the data acquisition system was through co-axial cable and a BNC plug was mounted on the amplifier box.

3.2.4 Data Acquisition System

3.2.4.1 Preliminary tests

Preliminary tests were carried out by feeding the signal for the amplifiers into a *HEWLETT-PACKARD 54600A* digital oscilloscope with a *54658A* measurement/storage module attached. The data was transferred to a PC, by means of a RS-232 interface, where the data was saved. The resolution of the data was limited by the 8 bit resolution of the digital oscilloscope. This was not the only limitation of the oscilloscope, as the storage module could only capture 1000 data points, which limited the width of window that could be captured. This meant that the frequency required to enable the oscilloscope to capture both incident and reflected pulses on a single window was too narrow. It was therefore decided that a high speed data acquisition card would be purchased and a dedicated data acquisition system installed for the SHPB apparatus.

3.2.4.2 General description of data acquisition card

The high speed data acquisition card purchased was the ADLINK PCI-9812 card. The PCI-9812 has four independent channels that can sample at a maximum of 20MHz per channel. *Table 3.1* gives the general specifications for the card. For the complete details of the card the reader is referred to the users manual [42]

Table 3.1 General Specifications for the Data Acquisition Card

Maximum sample rate per channel	20MHz
Number of simultaneous input channels	4
Analog input resolution	12-bit
Bipolar signal input range	+/-5V or +/- 1V
Programmable sampling rate	20MHz to 156.25kHz

3.2.4.3 Operation of the data acquisition program

Microsoft Visual Basic was chosen to program the card as it provided a simple and user friendly way to create a user interface for the card. *Visual Basic* was also the language

that was used for linking *Matlab* and *Microsoft Excel.* See *Section 4.4.2.2* for more details on the *Excel-Matlab* link

Figure 3-10 shows the user interface for the data acquisition card. It was laid out so as to resemble that of an oscilloscope to minimise the time to train an operator. The parameters featured include:

- Sample frequency
- Trigger level setting
- Trigger type. Post-Trigger, Pre-Trigger, Delay-Trigger, Middle-Trigger and Soft-Trigger
- Trigger polarity
- Number of channels to be used
- Continuous scan or signal shot mode.

The additional features that were included in the system were as follows:

- The selection of the number of data points to be taken. (1000 to 24000 data points per channel)
- The ability to view the complete captured data or to the view only a portion of it.
- The ability to switch off a channel in the view box, without losing the data of the other channels, so as to view only the channel of interest.
- The ability to include details of the experiment such as the speed trap time, striker dimensions, bridge voltage, specimen material and dimensions, and a block in which to make comments and notes about the experiment.

Once the data was captured it could be saved. The standard *Microsoft SAVE* command dialog box was called for the saving operation. This made the system user friendly as most of the operators on the system would be familiar with *Windows.* The data was saved in a TXT file format as almost all programs can read a TXT file format and it is relatively

compact as it does not include any style typing that an Excel file might have. When the data was saved the time and date was automatically saved at the top of the file. *Figure 3-11* shows the layout of some typical saved data. The *Microsoft Visual Basic* coding for the data acquisition user interface can be found in *Appendix A.3*

3.2.4.4 Steps that were used to access the ADLINK card

The following provides a summary of the steps that were used to access the card and take a sample. If more detail is required, the reader is referred to the users manual [42] and the function reference manual [43]

1. Register the card. This initialises the hardware and software for the PCI-bus, this returns a numeric card ID.
2. Configure the card. This sets up the following: trigger mode, trigger source, trigger polarity, clock source, trigger level and post count.
3. Once the card has been registered and configured, a sample can be taken.
4. When the sample has been taken the A to D conversion must be stopped and the data stored in the buffer.
5. The binary data stored in the buffer is converted to a voltage and stored as an output.
6. When all testing is over the card is released. This tells the PC that the card is not in use.

3.2.5 Preliminary Testing of the System

3.2.5.1 Problems encountered with noise

When the system was first used there was significant noise on one of the lines. This noise was observed as a triangular wave form, *Figure 3-12*. When this signal was processed to calibrate the system it resulted in an error in the momentum balance of about 8%. By working through the whole system, looking to the source of the noise, it was found that the output cables from the amplifiers to the card were run too close to the video monitor

power supply and monitor signal line. The line was rerouted and the noise did not appear in the subsequent data signal.

The other form of noise came from cross coupling between the two output lines of the amplifiers. If the output lines were run too close to each other, they would introduce a small offset into each others line. *Figure 3-13* shows how the first line from amplifier 1 introduces a small offset in the lead up to the second reading from amplifier 2. If this reading was used for calibration the momentum calculation would have an error of 0.93%. This error can be seen in *Figure 3-13* as the momentum curve starts to rise from zero before the main body on the pulse has started. This error was overcome by separating the amplifier output cables. This reading was processed by only starting the momentum calculation for the second pulse at the beginning of the main body of the second pulse. The resultant error in momentum between the two pulses was then only 0.08%. (See Section 5 for more information on the calibration the system)

3.2.5.2 Debonding of strain gauges

In the first calibration test that was carried out, the stress in the bar was taken to approximately $300MPa$. At this stress level, the bar should not have experienced plastic strain as the yield stress is $480MPa$. This resulted in the debonding of the strain gauges after only one or two strikes. The debonding could be seen clearly in the signal as it did not have the typical trapezoidal shape. The strain gauges were also easily removed from the bar indicating that the bonding glue had failed. The strain limit was not exceeded as the cement used (cyanoacrylates base) has a strain limit of 3% [44] and the maximum strain in the bar was 0.15% at $300MPa$. By keeping the stress level in the bar to below $100MPa$ the debonding problem of the strain gauges was overcome. This indicates that there is a maximum strain rate limit that the cement can withstand under these shock loading conditions. Further work has to be done to find the cause of the debonding but this is beyond the scope of the current project.

3.3 Test Procedure

The following procedure was followed when performing a material test on the SHPB apparatus.

3.3.1 Installation of the Bars

The bars were mounted in the bar supports and secured down. The two bars were then setup with a spirit level to get them level and coplanar. The incident bar was first aligned with the barrel so that the striker impacted squarely and in the middle of the bar. The two bars were them rechecked to see that they were both aligned relative to each other. All supports were then secured. A last check was performed to ensure that none of the bars had moved.

3.3.2 Setup of the Electronics

The strain gauge leads from the bars were plugged into the amplifiers and tightened down, and the power supply to the amplifiers was set to $+7V$ and $-7V$. The maximum voltage that the amplifiers can take was $+18V$ and $-18V$ but the data acquisition card had a maximum overvoltage of $\pm 22V$ so to protect the card the voltage was set to $+7V$ and $-7V$. The strain gauge bridge voltage was set to a maximum of $+7V$ and $-7V$. At this voltage setting the maximum stress in the bar would be $72MPa$ and this gave a full range of $+5V$ and $-5V$ to the data acquisition card. If the bridge voltage was set to $+5V$ and $-5V$ then the maximum stress in the bar would be $120MPa$ and would correspond to a full range of $+5V$ and $-5V$ being fed into the data acquisition card. The bridge voltage was set to the voltage that would give near maximum voltage into the card for the predicated stress in the bar.

3.3.3 Setup of the Data Acquisition System

To run the data acquisition program the icon marked SHPB CAPTURE was double clicked, which loaded the program and displayed the user interface as shown in *Figure 3-10*. The amplifiers first had to be zeroed so as to have the input signal in the middle of the range on the card. This was done by setting the system to continuous scan mode with

a software trigger. This sets the system to scan the channel every $\frac{1}{4}$ second and display the result. This allowed the operator to adjust the strain gauge bridge zeroing resistor in such a way as to move the signal level to near the zero mark. It was not necessary to set the level to exactly zero as the data processing program tests for this and sets the level to zero. See *Section 4.4.2.3* for further detail on the zeroing of the data.

When the amplifiers has been zeroed the system was set to capture data, so the continuous scan is swiched off and single shot mode selected. The following also had to be set:

- The number of data points that must be sampled and the post trigger count had to be set. 15000 points was the typical setting for the lengths of bars of this setup. The post trigger count was set to 2000 as the default, or 1000 if the number of data points was less than 5000.
- The trigger level has to be set. The trigger level was typically set to $+0.4V$ to $+0.6V$ above the input signal level.
- The trigger mode must be set to **Middle-Trigger.** This trigger mode takes in data continuously until the input signal goes higher than the trigger level. When this happens the internal counter starts counting until it has reached the number of samples required minus the number of post trigger count. The result is that the required number of post trigger count are captured before the trigger event, with the remainder of samples captured after the trigger event.
- The appropriate sample frequency has to be set.

Once the card is setup, data capture is facilitated.

3.3.4 Charging and Discharging of the Gas Gun

The gas gun was charged to the desired test pressure and the striker was loaded into the barrel. For the tests that were carried out the test pressure was kept at 5 bar. The 300mm striker was not pushed more that 150mm down the barrel. With this setup the stress in the bar was kept to a maximum of 100MPa. When the test programme was completed the gas gun was depressurised and all valving closed.

3.3.5 Performing the Experiments

3.3.5.1 Specimen preparation

The specimen diameter and length were measured with a micrometer and these dimensions entered in the data acquisition system. Before the specimen was placed between the bars a light layer of thin grease is applied to the bar ends. This aided in reducing the friction effects as well as in keeping the specimen in place. The specimen was placed between the bars and aligned by eye, to be positioned in the middle of the bar.

3.3.5.2 Capturing and saving the data

The start button was pressed on the data acquisition system, the safety catch lifted and the fire button pressed. The captured data would then be displayed as in *Figure 3-10.* The data was saved by pressing the save button and entering the file name. The specimen was retrieved and placed in a small plastic bag with a label containing the file name, dimensions of the specimen and the date.

The test was considered completed once the data had been saved and the specimen bagged and labelled. The data can then be processed. (See *Section 4* for details on the data processing.)

3.4 Testing program

3.4.1 Compression Testing of Material on the SHPB

Three materials were tested to validate that the SHPB system was operating correctly. These materials were mild steel (EN1A), aluminium (6061-T6) and copper. The mild steel and copper were tested in the as received state as well as in the annealed state. The term 'as received' implies that the specimen has be machined and no additional heat treatment was performed. This is done to compare the difference in the material properties between the as received state and in the annealed state.

- As there was no set test procedure for tests conducted on a SHPB, the following parameters were used:

- Dimensions of striker used were: length of 300mm and diameter of 10mm.
- Pressure of gas gun was 5 bar.
- Maximum stress in the bars was $100MPa$.
- All specimens were lubricated before test.

The mild steel test specimens were $\phi 4 \times 3$ thick. Half of the specimens that were machined were annealed at $900°C$ for 10 minutes and allowed to cool in an oven, the other half were tested in the as received condition The aluminum specimens were $\phi 5 \times 2.5$ thick and were tested in the as received state. The annealed copper specimens were $\phi 4 \times 3$ thick and were annealed at $450°C$ for 10 minutes and allowed to cool in an oven. The as received copper specimens were $\phi 6 \times 3$ thick. The annealed copper specimen were smaller in diameter as more strain was wanted for the given striker length.

3.4.2 Quasi-static Tensile Tests

Standard tensile tests for mild steel (EN1A), aluminium (6061-T6) and copper were conducted in accordance with BS-18 [45]. These test were performed to provide a baseline with which to compare the dynamic with the static material properties. Similar to the dynamic compression tests, the Mild Steel and Copper were tested in the as received state and in the annealed state. The test parameters were as follows:

- The specimen manufactured according to BS-18 and D metric round tensile test pieces was used [45], which were $\phi 7.1$mm and a gauge length of 25mm.
- The specimens were tested on a Zwick 1482 testing machine.
- Head speed of 1.5mm per minute which relates to a strain rate of $0.001s^{-1}$.
- The test were conducted at room temperature ($20°C$).
- Half of the copper specimens were annealed at $450°C$ for 60 minutes and allowed to cool in an oven.
- Half of the mild steel specimens were annealed at $900°C$ for 60 minutes and allowed to cool in an oven.

3.5 Summary

This chapter has dealt with the experimental apparatus making up the SHPB system. The mechanical, electronic and data acquisition subsystems have been described and the operation of each of their components discussed.

The capturing of the data from the SHPB system can be summarised as follows. The measurement of the stress wave was achieved by means of $2mm$ strain gauges that were wired in a full bridge arrangement that compensates for bending and temperature. The signal from the full bridge was fed into a Burr-Brown INA110 fast settling instrumentation amplifier, which was mounted on custom built boards, where it was amplified by a gain of 1000. The signal was then fed into a ADLINK High Speed Data Acquisition Card where it was sampled, at a maximum rate of $20MHz$ and at 12 bit resolution, and stored.

The readings that were captured by the data acquisition system were used to determine the time dependent stress state of the specimen. The chapter which follows deals with the processing of the time dependent strain state data to obtain the stress vs. strain plots.

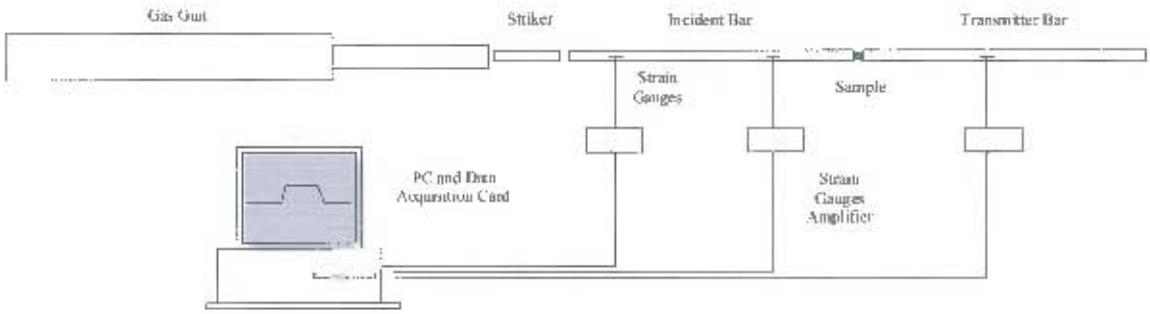

FIGURE 3-1. Schematic representation of the split Hopkinson pressure bar system.

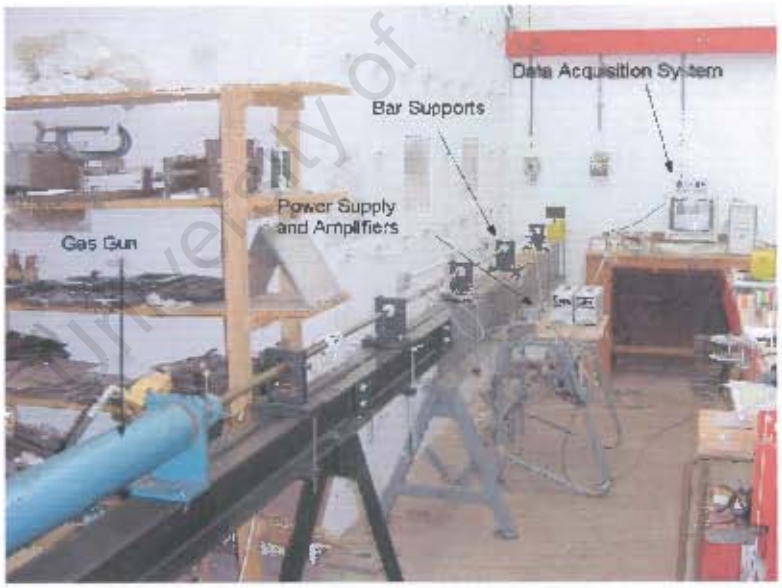

FIGURE 3-2. Photograph of the SHPB system

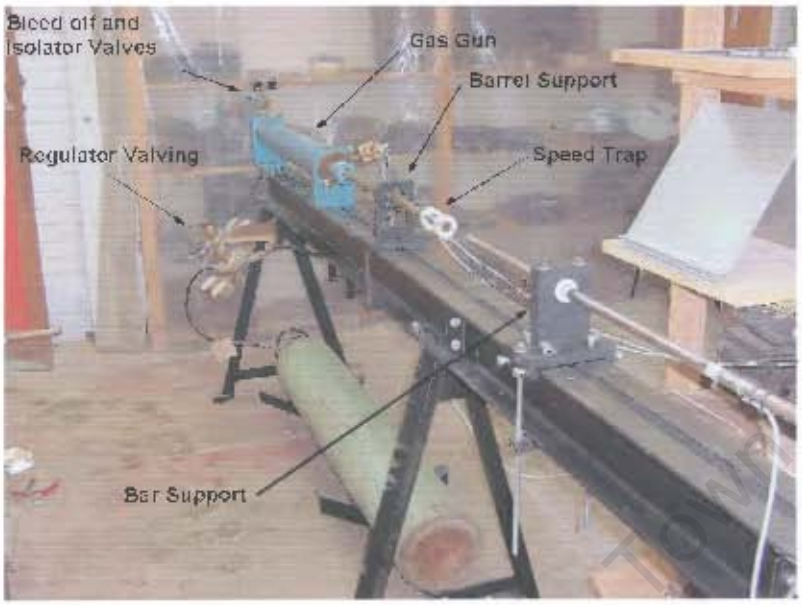

FIGURE 3-3. Photograph of air gun on stand

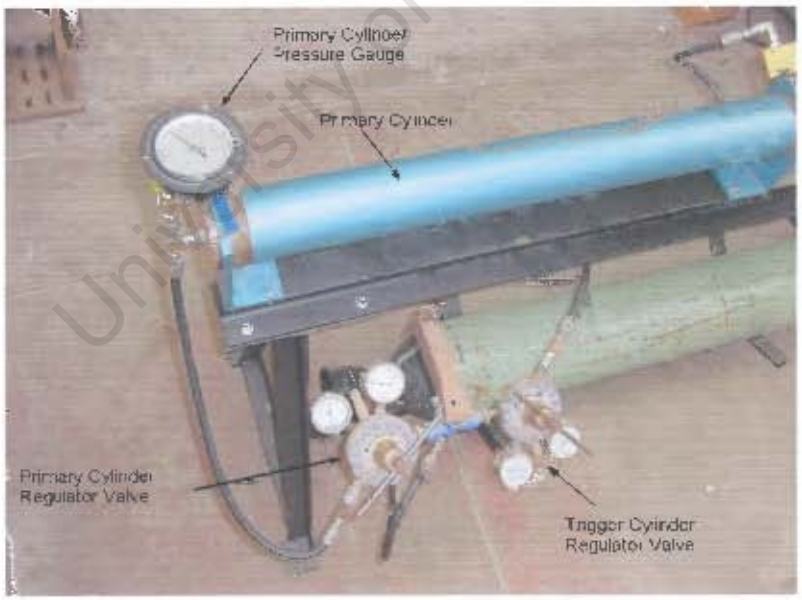

FIGURE 3-4. Photograph of the control valving for gas gun

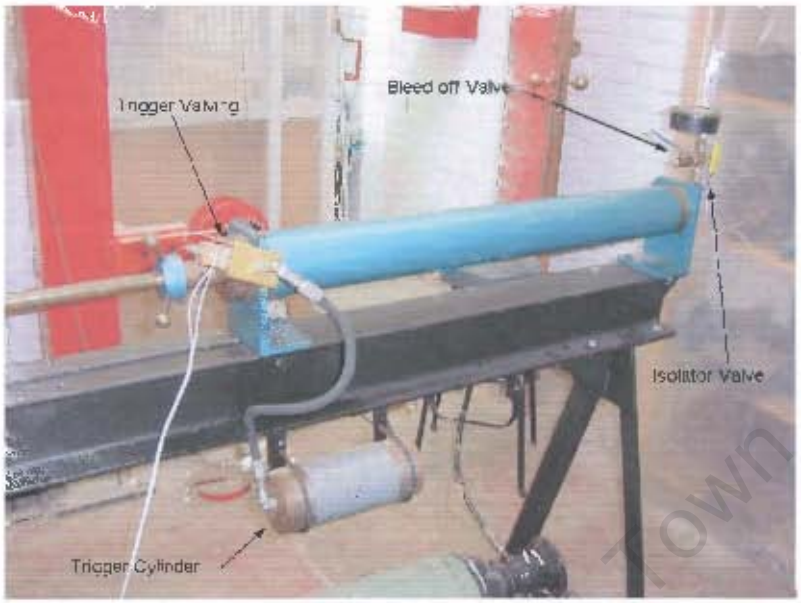

FIGURE 3-5. Photograph of trigger valving for gas gun

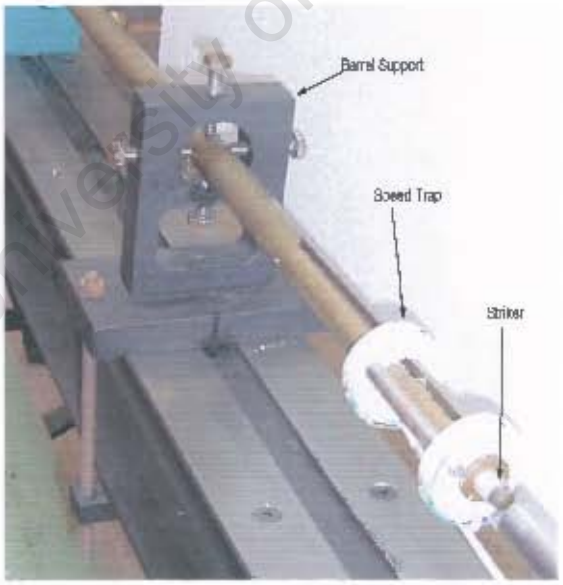

FIGURE 3-6. Photograph of the barrel support

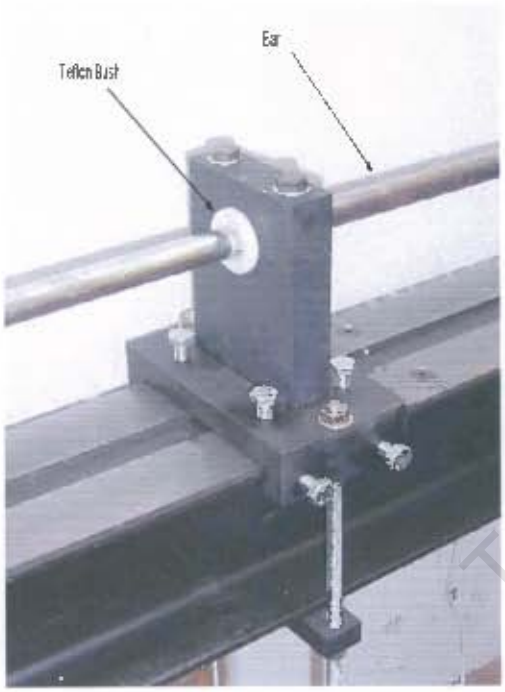

FIGURE 3-7. Photograph of the bar support

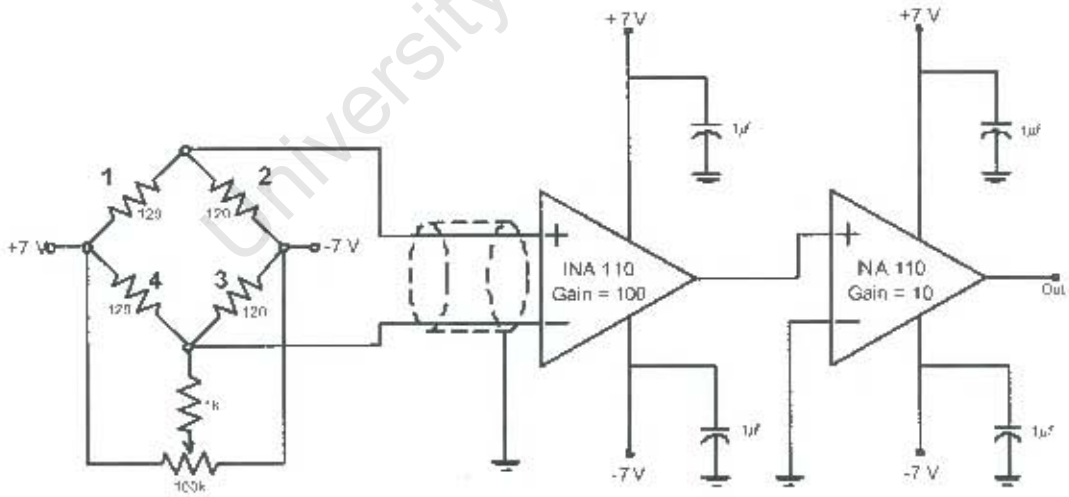

FIGURE 3-8. Sketch of the circuit diagram for the strain gauge bridge amplifiers

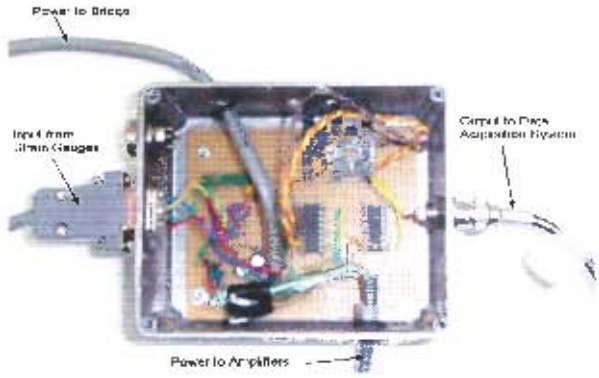

FIGURE 3-9. Photograph of strain gauge amplifier

FIGURE 3-10. Visual Basic user interface of the data acquisition system

Description of Data	Experiment No: copper 1			
Date:	6/14/01			
Time:	12:01:23			
Rate:	5 MHz			
Striker Data				
Length:	100	**Diameter:**	10	
Speed Trap Data				
Time:	9.81	**Trap Gap**	82.01	
Specimen Data				
Length:	3.01	**Diameter:**	5.02	**Material:** Copper
Bridge Voltage				
Voltage:	5 V			

Time	Channel 0	Channel 1
0.00000000	-0.080566	0.1513672
0.00000020	-0.070801	0.1391602
0.00000040	-0.073242	0.15625
0.00000060	-0.087891	0.1782227
0.00000080	-0.063477	0.1855469

FIGURE 3-11. Layout of the stored data

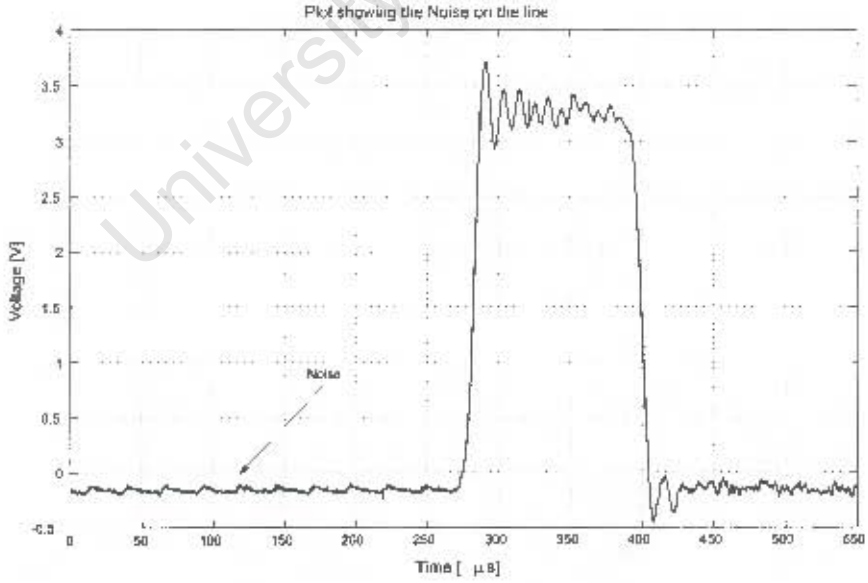

FIGURE 3-12. Plot showing the noise on the line

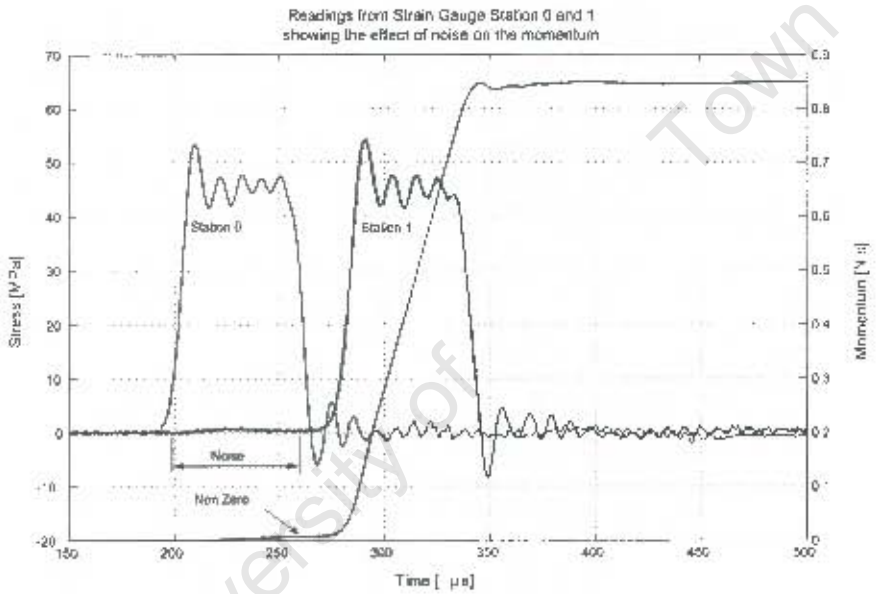

FIGURE 3-13. Plot showing the effect of cross coupling between station 0 and station 1 on the momentum of the system.

4

Data Processing

4.1 Introduction

As the signals were measured at some distance from the specimen, it was necessary to "shift" the signal to the bar/specimen interface in order to interpret the information in the stress wave. The "shifting" procedure is complicated by the fact that longitudinal stress waves that propagate through a round bar are subject to dispersion: the higher frequency components of a wave travel slower than the lower frequency components. This shifting of the pulse was achieved by "undispersing" the reflected and transmitted pulses and dispersing the incident pulse using the Pochhammer-Chree dispersion curves. The details of generating and incorporating the Pochhammer-Chree dispersion curves, to correct for dispersion, forms a major part of this chapter.

To improve the accuracy of the dispersion correction, the higher frequency components of the stress wave need to be included. This requires the inclusion of the higher Pochhammer-Chree dispersion modes in the dispersion correction program.

This chapter first establishes how the Pochhammer-Chree dispersion curves are generated and the basic Fourier analysis that was used to perform the dispersion correction. The operation of the program that performs the dispersion correction and the post processing is discussed in this chapter. That is, how the stress vs. strain plot was obtained from the time dependent strain state data.

4.2 Solution of the Equation of Motion

The solution to the equation of motion for a wave propagating in an infinitely long cylindrical bar was solved by Pochhammer (1876) and independently by Chree (1889). The solution relates the propagation velocity C_p to the wavelength Λ and is exact only for an infinitely long cylinder and is approximately correct for bars of finite length. An excellent

summary of the Pochhammer-Chree solution has been given by Love [27], which Bancroft [46] has, for ease of computation, rewritten in the following form.

$$(x-1)^2\,\phi(ha) - (\beta x - 1)\,[x - \phi(ka)] = 0 \tag{4.1}$$

where

$x = (1+\nu)\left(\frac{C_p}{C_0}\right)^2$	C_p = Phase velocity
$\beta = \frac{1-2\nu}{1-\nu}$	C_0 = Fundamental velocity = $\sqrt{\frac{E}{\rho}}$
$h = \gamma\sqrt{\beta x - 1}$	$\gamma = \frac{2\pi}{\Lambda}$, Λ = Wavelength
$k = \gamma\sqrt{2x - 1}$	$a = \frac{d}{2}$, d= Diameter of the bar
$\phi(ha) = (ha)\frac{J_0(ha)}{J_1(ha)}$	$\phi(ka) = (ka)\frac{J_0(ka)}{J_1(ka)}$

J_0 is the Bessel function of the first kind of order zero,

$$J_0(x) = \sum_{m=0}^{\infty} \frac{(-1)^m x^{2m}}{2^{2m}(m!)^2}$$

J_1 is the Bessel function of the first kind of order one,

$$J_1(x) = \sum_{m=0}^{\infty} \frac{(-1)^m x^{2m+1}}{2^{2m+1} m!\,(m+1)!}$$

4.2.1 Generating the Pochhammer-Chree Modes

The method for determining the Pochhammer-Chree modes is as follows:

1. Choose a value for the Poisson's ratio ν and γa, see *Figure 4-1.*
2. Find the value of x that will give the first zero for *Equation 4.1.* This is achieved by choosing values for $\frac{C_p}{C_0}$ until *Equation 4.1* is satisfied. The first zero crossing is the first Pochhammer-Chree mode. Subsequent zero crossings provide the higher modes.
3. Note that the first choice of $\frac{C_p}{C_0}$ is important, it is therefore recommended that the first choice of γa be almost zero and $\frac{C_p}{C_0} = 1$, then the next choice of x can be determined from the previous value of x.

Figure 4-2 provides a plot of *Equation 4.1.* The first zero is relatively simple to find as most computer programs will be able to find this root. The second and higher modes

are not as simple as the asymptotes tend to confuse the root finding algorithm and this results in the wrong mode being found. This can be overcome by writing additional rules into the algorithm or by resetting the start point when the wrong root was found. Both methods were used in plotting the first four Pochhammer-Chree modes. However, as more rules were entered into the root finding algorithm so the slower the process became.

The Pochhammer-Chree solutions of the first four modes of vibration are shown in *Figure (4-3)* for a material with a Poisson's ratio of 0.26. The graph has been normalised by dividing the phase velocity C_p by the fundamental velocity C_0. From *Figure (4-3)* it is evident that the propagation velocity decreases with decreasing wavelength, that is, a high frequency wave travels slower than a lower frequency wave.

4.2.2 Determining the Jump Points Between the Modes from the Phase Velocity.

From the phase velocity $C_p = \frac{\varpi}{K}$ where $K = \frac{2\pi}{\Lambda}$ and ϖ = angular frequency, it can be shown that the group velocity is $C_g = \frac{d\varpi}{dK}$ [23]. In this form the group velocity is of little use as Λ is dependent on the wave speed ($C = \Lambda f$) and on the size of the bar. A non bar-specific equation for the group velocity is therefore required. *Equation 4.2* provides a normalised expression for the group velocity which is not dependent on the bar size.

$$\frac{C_g}{C_0} = \left(\frac{1}{Y} - \frac{X}{Y^2}.\frac{dY}{dX}\right) \tag{4.2}$$

where

$$Y = \frac{C_g}{C_0} \quad C_g = \text{ Group velocity}$$
$$X = \frac{d.f}{C_0} \quad f = \text{ frequency [Hz]}$$

A plot of the first four Pochhammer-Chree modes showing the phase velocity and their corresponding group velocity is given in *Figure 4-4*. In this form the transition points can be determined by noting that the highest group velocity dominates the propagation speed of the wave [33]. *Figure 4-5* shows the jump points for the first four Pochhammer-Chree modes. The phase velocity for the first mode and first four modes are shown in *Figure 4-6*. This is the final form of the Pochhammer-Chree dispersion curves that have been used in the dispersion correction program in this thesis.

4.3 Method of analysis using the Pochhammer-Chree solution and the Fast Fourier Transform (FFT) to Correct for Dispersion

4.3.1 Fourier Theory

To explain how dispersion correction is achieved using the FFT it is necessary to discuss some Fourier notation and concepts. Only the essential concepts will be given as the details are lengthy and beyond the scope of this report. The reader is referred to Morrison [29] for more details.

The expression

$$f(t) \Leftrightarrow F(\varpi) \tag{4.3}$$

states that the Fourier transform of the function $f(t)$ from the time domain into the frequency domain is $F(\varpi)$ and the inverse Fourier transform of $F(\varpi)$ is $f(t)$.

When moving a pulse from one point in time to another point in time the **Time Shift Theorem** is used.

Time Shift Theorem

$$\text{Let } f(t) \Leftrightarrow F(\varpi)$$

$$\text{Then } f(t-\tau) \Leftrightarrow F(\varpi)\, e^{-j\varpi\tau} \tag{4.4}$$

This states that when a function $f(t)$ undergoes a time shift and becomes $f(t-\tau)$, it's Fourier transform is multiplied by a complex exponential $e^{-j\varpi\tau}$ [29].

4.3.2 Dispersion Correction

To shift and correct for dispersion the recorded pulse is first transformed into the frequency domain using the FFT. Then the individual frequency components are multiplied by $e^{-j\varpi\tau}$.

Where

- ϖ = radial frequency in *rad/sec* of the particular frequency component under consideration.

- $\tau = Z/C_p$ in seconds
- Z is the distance to move the pulse in meters. This is normally the distance from the strain gauge to the specimen/bar interface.
- C_p = Phase velocity of the particular frequency component under consideration, from the Pochhammer-Chree solution.

The inverse FFT is then performed and the corrected pulse is plotted.

4.4 Operation of the Dispersion Correction Program

In this section the operation of the dispersion correction program is discussed. The program is first described in a flow diagram and each major step is broken down.

4.4.1 Flow Chart Describing Dispersion Correction Program

The flow diagrams below *(Figures 4-7 and 4-8)* describe the procedure that the dispersion correction program follows. It also shows the *Excel* - *Matlab* transition points and the transition points between the Time Domain and the Frequency Domain.

4.4.2 Details of Dispersion Correction Program

The operation of the dispersion correction program is broken down and explained in this section. The Fourier analysis used for dispersion correction is discussed in *Section 4.3.*

4.4.2.1 Data from Data Acquisition Card

The data from the acquisition card is stored in a text file. *Section 3.2.4* describes the operation of the data acquisition card, the procedure for saving data and the format of the data. The data file that is to be processed is opened into *Excel.* The data has to be split-up into different sections before the dispersion correction can be implemented. These sections are the incident pulse (data set 1), reflected pulse (data set 2) and transmitted pulse (data set 3). *Figure 4-9* shows the signal from a compression test of a mild steel sprecimen (the incident bar was struck with a 300mm striker). The separation of the data

is done manually by looking at a plot of the data and selecting the time for the break point. The break point is chosen so that there is sufficient time before and after the pulse so that the pulse can be moved without 'wrap-around' occurring. The data sets are then copied into the *Excel* sheet that will correct for dispersion.

4.4.2.2 Data Transfer to Matlab

An *Excel* user-defined function is used to transfer the data that has to be processed in *Matlab*. This function also invokes the dispersion correction program in *Matlab* and then calls for the results when the program has run its course.

The user-defined function is defined in the *Microsoft Visual Basic* Module and there are three main functions that link *Excel* to *Matlab*. These are:

`MLEvalString` – Evaluate command in Matlab from Excel.

`MLPutMatrix` – Create or overwrite Matlab matrix with data from Excel worksheet.

`MLGetMatrix` – Write contents of Matlab matrix in Excel worksheet.

The following extract of the coding shows the initialisation statement for the user defined function:

```
Function Dispersion(dt, read1, dist, E, r, v, D, mode, x3, BSF, BSF1, BSF2,
BPF, BPF1, BPF2, undisp_reading, corr_v1)
```

The function is defined as Dispersion, this name is used in the *Excel* work sheet in the same way as one would used any other *Excel* function such as MAX or SIN. The variables in the brackets are data that is to be sent to *Matlab* or the location on the spreadsheet where data is to be placed when retrieved from *Matlab.*(See *Appendix A.3* for the full documented code of the user defined function.

4.4.2.3 Zeroing of the data

The data from the data acquisition card is not zeroed, this can be seen in *Figure 4-9*. This results from the manual setting of the bridge voltage to a position that will maximize the range of the signal. See *Section 3.3.3* for more information on the setting of the level of the signal. To zero the data the first 100 samples are used to get a mean value. This mean is subtracted from the data to bring the reading to zero.

4.4.2.4 Adjustment of the data length

The length of the data is adjusted so that the number of data points is even. The adjustment to an even number of data points serves to decrease the time required to perform the Fourier transform. The fastest Fourier transform occurs when the number of data points are of powers of two. If the number of data points is not a power of two, then an even number is preferable as they have less prime factors. See *Morrison* [29] or *Matlab Signal Processing Toolbox User's Guide* [47] for more information on the FFT algorithm. The adjustment to the length is done by testing if there is a remainder after dividing by two. If there is a remainder, the last data point is removed.

4.4.2.5 Calculation of variables necessary for the dispersion correction

The following variables are calculated from the corrected data length and are then used throughout the remainder of the program.

1. The fundamental speed of sound in the bar $\left(C_0 = \sqrt{\frac{E}{\rho}}\right)$ [m/s].
2. A vector of the time using the time interval between the samples (t) [s].
3. The period of the sample (T). This is the total time taken for the sample and is obtained from the largest value in the time vector.
4. The fundamental angular velocity $\left(\varpi_0 = \frac{2\pi}{T}\right)$ [rad/s]. This is the angular velocity between each data point in the frequency domain.
5. The vector of the angular velocity (ϖ_n) which is centered about the 0^{th} term and has a step size of ϖ_0.
6. The vector of the frequency (f) [Hz].

4.4.2.6 Transformation into the frequency domain

The data is transformed into the frequency domain with the built in Fast Fourier Transform function in *Matlab* . For details of the algorithm used see [47]. The transformed data that is generated by *Matlab* has the 0^{th} term on the left as can be seen in *Figure 4-10* (The normalised magnitude is plotted on logarithmic scale so as to make viewing possible). If

the data was to be used in this form the dispersion correction curves would have to be generated up to a frequency of 10 MHz. This is overcome by shifting the data so that the 0^{th} term is in the centre, i.e. with negative frequencies on the left and positive frequencies on the right of the 0^{th} term as shown in *Figure 4-11*. With this shift the dispersion correction curves have only to be generated up to a frequency of 5 MHz as the negative frequencies are a mirror of the positive ones. This shift also simplifies the procedure for correcting for the amplifier drop-off, amplifier phase shift and the filtering operations as they become symmetric about the 0^{th} term.

4.4.2.7 Compensation for amplifier drop-off and phase shift

The amplifiers used are Burr-Brown INA 110 instrumentation amplifiers. The data sheet indicates that the amplifier will, at a gain setting of 100, have a gain of 100 up to $100kHz$ and after that drop to a gain of 50 at $1MHz$. This was confirmed by testing the amplifiers with a digital oscilloscope and a signal generator and noting the gain. Refer to *Section 5.2* for the calibration of the amplifiers. The drop off was corrected by multiplying the magnitude of the frequencies above $100kHz$ by a function to bring the magnitude up to a gain of 100. The mapping function is shown in *Figure 4-12*. The phase shift was also tested and it was noted that there was a linear phase shift with a final shift of 170° at $800kHz$. The phase shift was corrected by adding the correct amount to the phase to bring it back to unity. The mapping function for the phase shift correction is shown in *Figure 4-13*.

4.4.2.8 Implementation of Band Stop and Band Pass filters

The inclusion of the ability to filter the data was undertaken to see the effect of removing certain frequencies, on the signal. This was done to see physically the group velocity and gain an understanding how the dispersion process breaks up the pulse, as reported by Lee [32].

The implementation of the band stop filter is relatively simple once the data has been moved into the frequency domain, as all that is needed is to zero the frequency band that is to be removed. This is shown in *Figure 4-14*. The Band Pass filter was implemented in a similar manner, except that one sets all other frequencies to zero except the ones required.

4.4.2.9 Calculation of the phase velocity from the Pochhammer-Chree modes

The Pochhammer-Chree curves are stored as a 3D plot. The axis being Poisson's ratio, the ratio of bar diameter to wavelength d/Λ and the normalised phase velocity C_p/C_0. From this 3D plot a single curve is extracted for the Poisson's ratio specified for the bar. The extraction of the curve is carried out by means of interpolating between the data points using a cubic function. From the Pochhammer-Chree curve (C_p/C_0 vs. d/Λ) the phase velocity for the individual frequencies is then calculated. In this calculation the diameter of the bar is taken into account and the final curve is a curve of C_p vs. f. This procedure of extracting the signal curve from a 3D plot of the Pochhammer-Chree curve is repeated for the number of modes that the operator wishes to use. Once all the curves have been calculated the jump points between modes are determined and finally a single curve is generated.

This single curve was generated for positive frequency only. The curve is mirrored about the 0^{th} frequency term to accommodate the negative frequency components. The final mapping function for the dispersion correction using four Pochhammer-Chree modes is shown in *Figure 4-15.*

4.4.2.10 Implementation of the phase shift to correct for dispersion

The phase of each frequency is then shifted by the amount calculated by the final mapping function. That is, the data, after being corrected for phase shift, drop-off and filtering, is multiplied by the complex exponential $e^{-j\omega_n \frac{Z}{C_P}}$. Note that only the phase of each frequency is modified and not the magnitude.

4.4.2.11 Transform from the frequency domain to the time domain

The data has now been corrected for dispersion and is transformed into the time domain with the Inverse Fast Fourier Transform function (IFFT). Before the data is transferred to *Excel,* a test was conducted to see that there were no imaginary components of the transformed data as a result of all the alterations to the signal. If there were this would indicate that one or more of the steps in the signal correction process was incorrect.

4.4.2.12 Transfer data to Excel spread sheet

At this point *Matlab* notifies *Excel* that the dispersion correction program is complete and the corrected data can be transferred. *Excel* then calls for the corrected data and pastes it into the *Excel* spreadsheet.

At this stage the data has been corrected for dispersion but has not been processed to obtain the stress-strain curve. In the following section the method of determining the stress-strain curve is discussed.

4.5 Post processing of data

4.5.1 Summary of One Dimensional Wave Propagation Theory

Wave propagation behavior for elastic bars is well understood and mathematically predictable [23] [24] [25]. From elementary wave theory the wave equation can be shown to be[7] [12] [26]

$$\frac{\partial^2 u}{\partial x^2} = \frac{1}{C_0^2} \cdot \frac{\partial^2 u}{\partial t^2}, \tag{4.5}$$

where $C_0 = \sqrt{\frac{E}{\rho}}$ is the fundamental longitudinal wave velocity, and u is the displacement.

From the wave equation the stress in the bar can be shown to be

$$\sigma = \rho C_0 v \tag{4.6}$$

were ρ is the density of the bar and v the velocity of the particles of the bar subjected to the pulse.

The stress at the incident bar/specimen interface is then

$$\sigma_{s1} = \frac{(\sigma_i - \sigma_r) A_{Bar}}{A_s(t)}, \tag{4.7}$$

and the stress at the specimen/transmitter bar interface is

$$\sigma_{s2} = \frac{\sigma_t A_{Bar}}{A_s(t)}. \tag{4.8}$$

Assuming incompressible plasticity, then $A_0.l_0 = A_s l_s$, (where A_0 is the original cross-sectional area, and A_s is the instantaneous cross-sectional area).

Note that once the ringing up of the specimen is complete and the specimen has attained a stable stress state then $\sigma_{s1} = \sigma_{s2}$.

From the displacement of the two bars the true strain of the specimen can found. The true strain is

$$\varepsilon_{true} = \ln\left(\frac{l}{l_0}\right) \tag{4.9}$$

And by differentiating the strain with respect to time gives the strain rate in the specimen

$$\dot{\varepsilon} = \frac{v_1 - v_2}{l_s(t)}. \tag{4.10}$$

For a detailed derivation of the above one dimensional wave propargation theory see *Section 2.4*

4.5.2 Obtaining the Stress, Strain and Strain Rate from the Input Signal

The data that has been handled so far has been a voltage reading from the strain gauge. This reading is converted to a stress by multiplying the voltage by the calibration factor (See *Section 5.6* for details on how the calibration factor was obtained). *Figure 4-16* shows the three readings (incident, reflected and transmitted) of a mild steel test shifted to the bar/specimen interface. As *Equation 4.7* uses two stress waves (incident and reflected) to calculate the stress in the sample it is termed "2-wave" analysis. And as *Equation 4.8* only uses one stress wave (transmitted pulse) to calculate the stress in the sample it is termed "1-wave" analysis. The strain and the strain rate are calculated in *Equations 4.9* and *4.10*, and finally the stress vs. strain curve for the material test can be plotted. *Figure 4-17* shows the stress vs. strain plot for the mild steel test. It also includes the strain rate vs. strain plot. The average of the strain rate plot was determined from the two points indicated on *Figure 4-17*. The first point was chosen so as to ignore the loading up of the specimen and the end point to ignore the unloading. When determining the average strain rate of the test these two points were used so as to have some reference.

4.6 Summary

In this chapter the data processing of the signal for the data acquisition system has been dealt with. This has included a brief discussion on the generation of the Pochhammer-Chree dispersion curves and the Fourier analysis that was used. This also includes how the higher modes of vibration were incorporated to improve the accuracy on the dispersion correction. The program that was written to perform the dispersion correction was discussed and finally a summary of the one dimensional wave propagation theory was given in order to establish some background for generating the stress-strain curve.

The chapter which follows deals with the calibration of the whole system, this includes the amplifiers, speed trap, determining the Young's modulus and Poisson's ratio for the bars and finally the dynamic calibration factor.

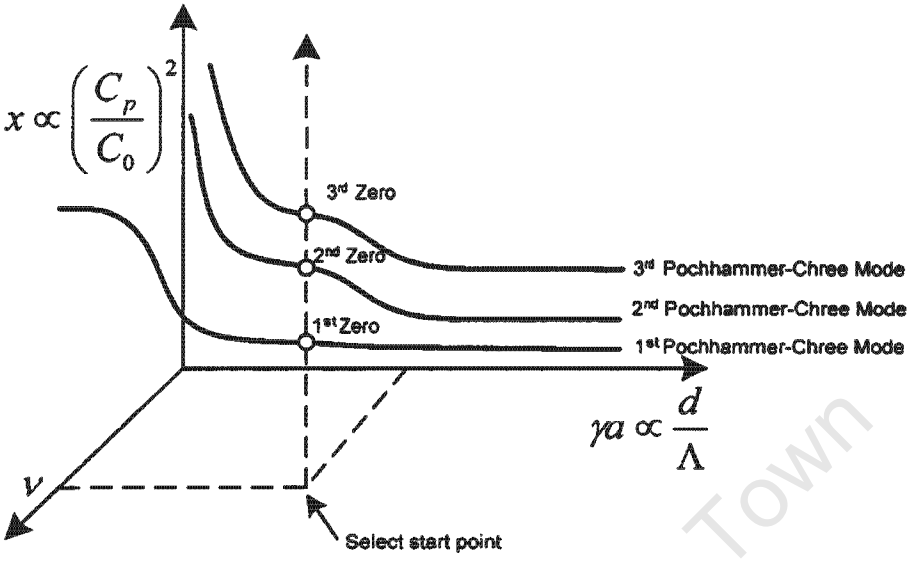

FIGURE 4-1. Method of determining the Pochhammer-Chree modes.

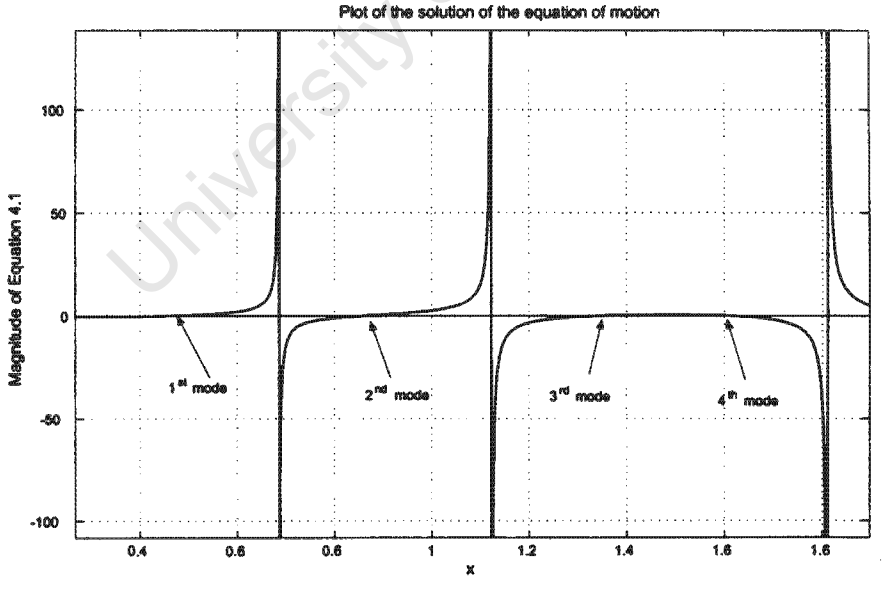

FIGURE 4-2. Plot of the solution of the equation of motion (*Equation 4.1*) with Poisson's ratio = 0.26 and $d/\Lambda = 2$ from which the zero crossings can be obtained.

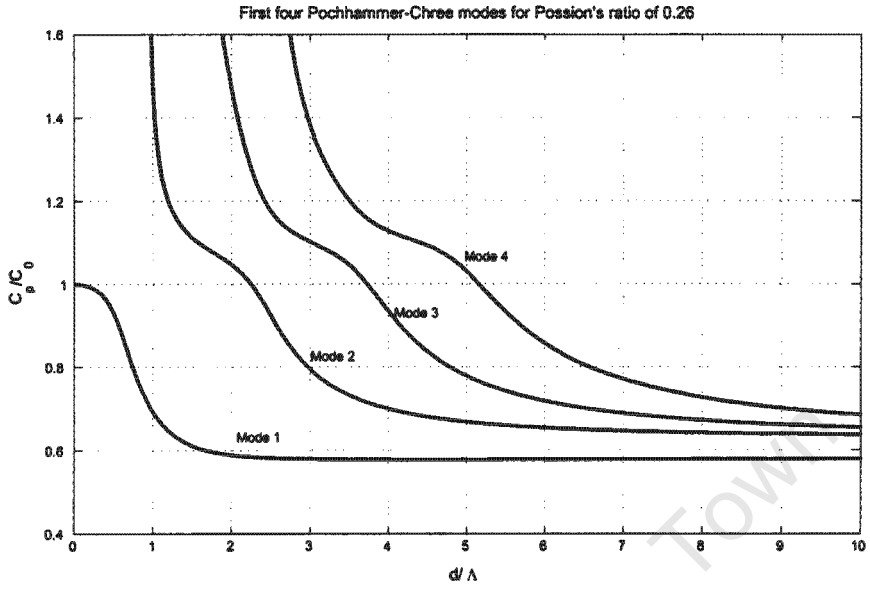

FIGURE 4-3. First four Pochhammer-Chree modes for Poisson's ratio of 0.26

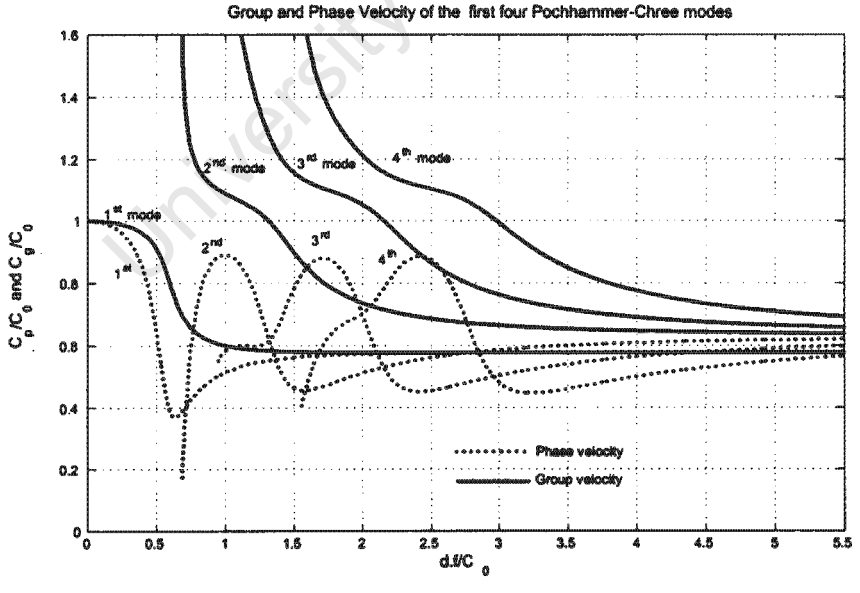

FIGURE 4-4. Group and Phase Velocity of the first four Pochhammer-Chree modes

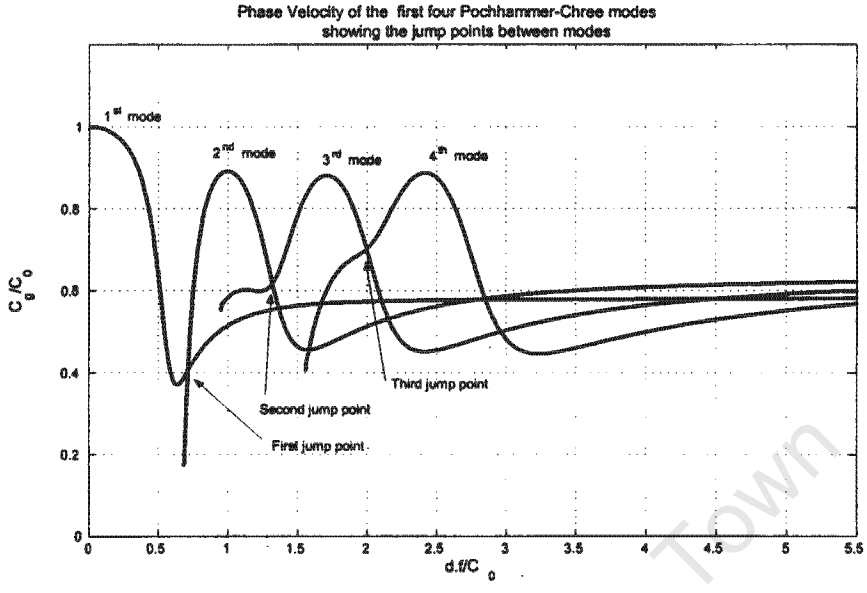

FIGURE 4-5. Phase Velocity of the first four Pochhammer-Chree modes showing the jump points between the modes.

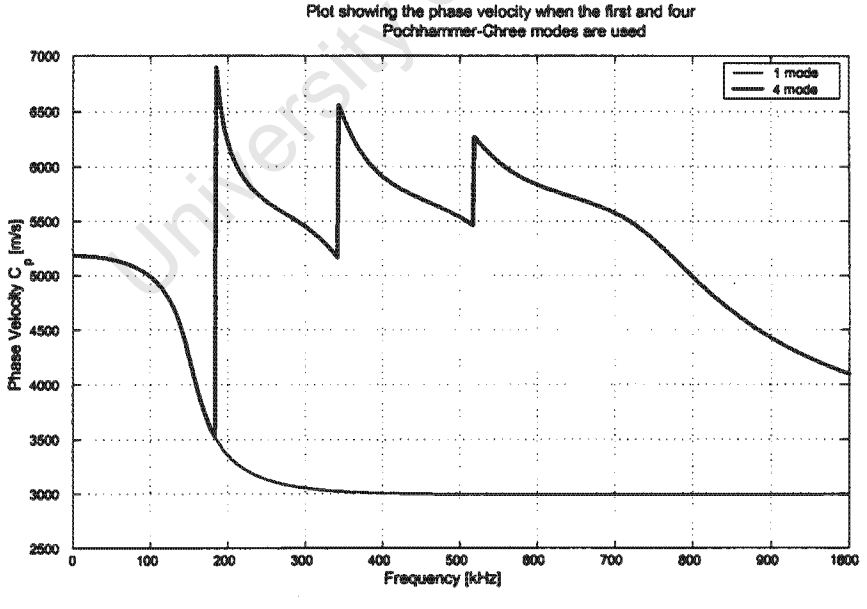

FIGURE 4-6. Plot showing the phase velocity when the first and four Pochhammer-Chree modes are used.

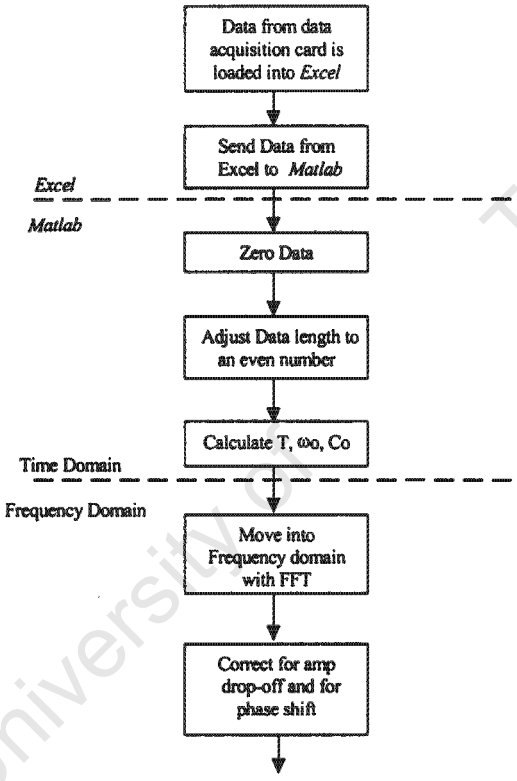

FIGURE 4-7. Flow diagram for dispersion correction program

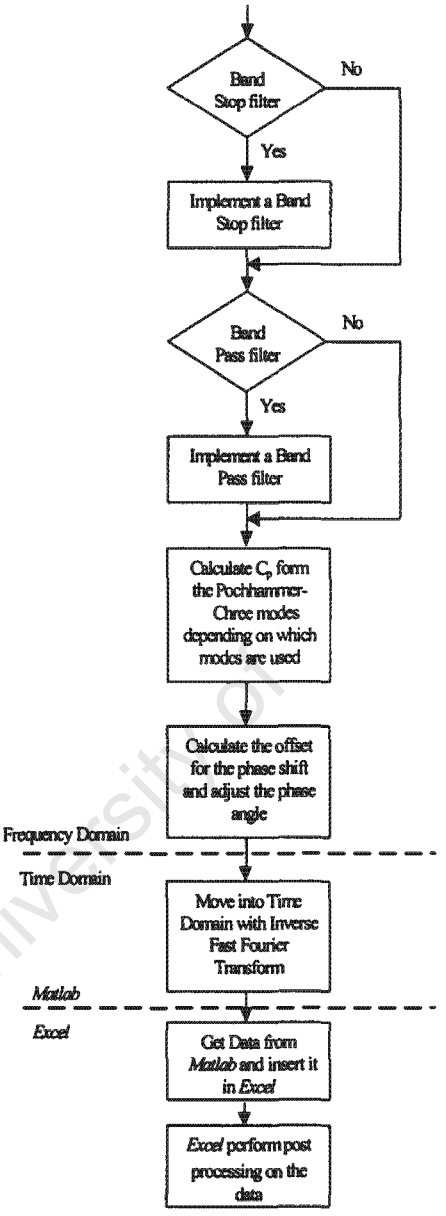

FIGURE 4-8. Flow diagram for dispersion correction program (continued)

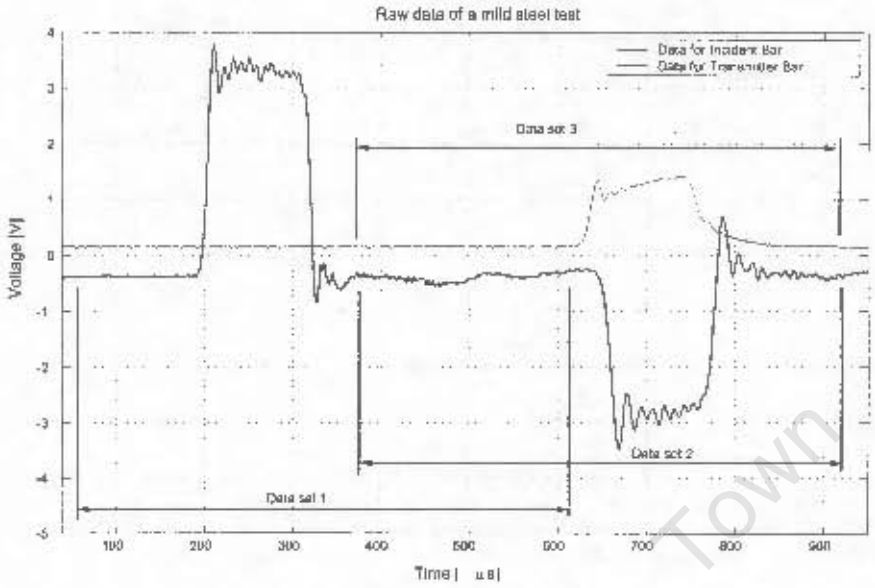

FIGURE 4-9. Raw Data from Acquisition System

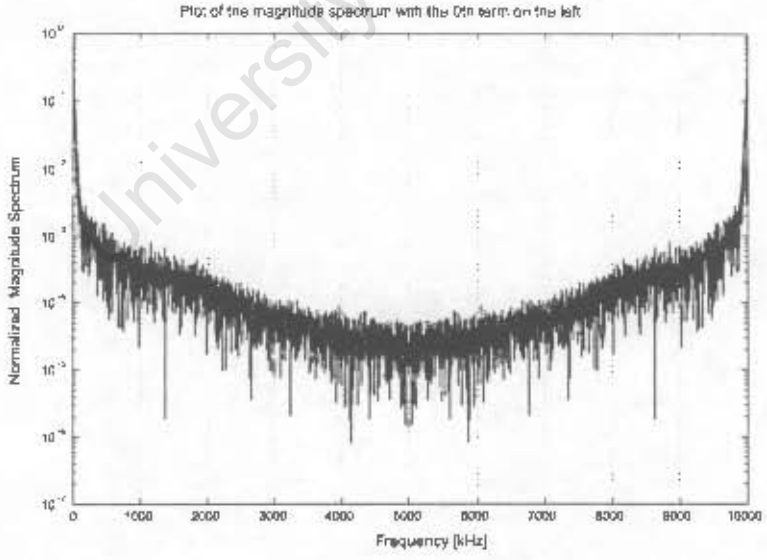

FIGURE 4-10. Plot of the magnitude spectrum with the 0^{th} term on the left.

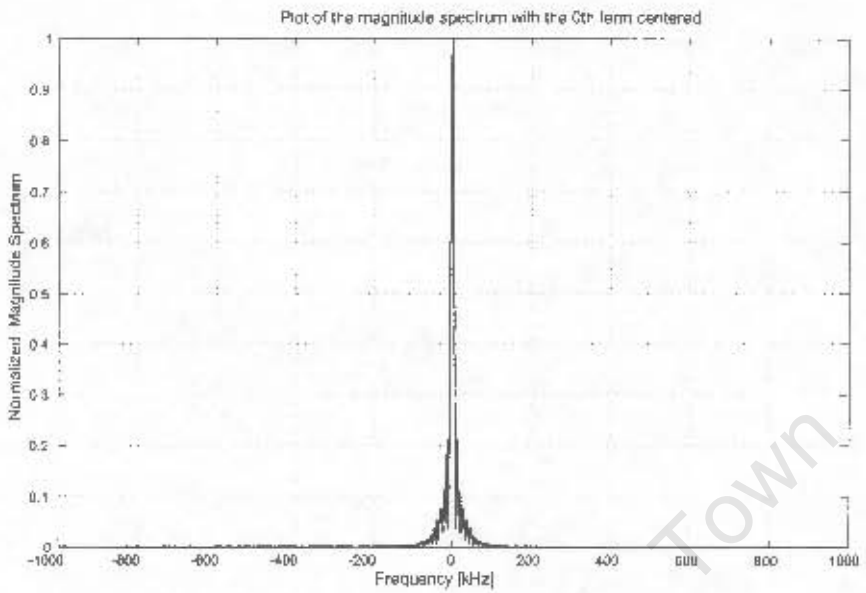

FIGURE 4-11. Plot of the magnitude spectrum with the 0^{th} term centered.

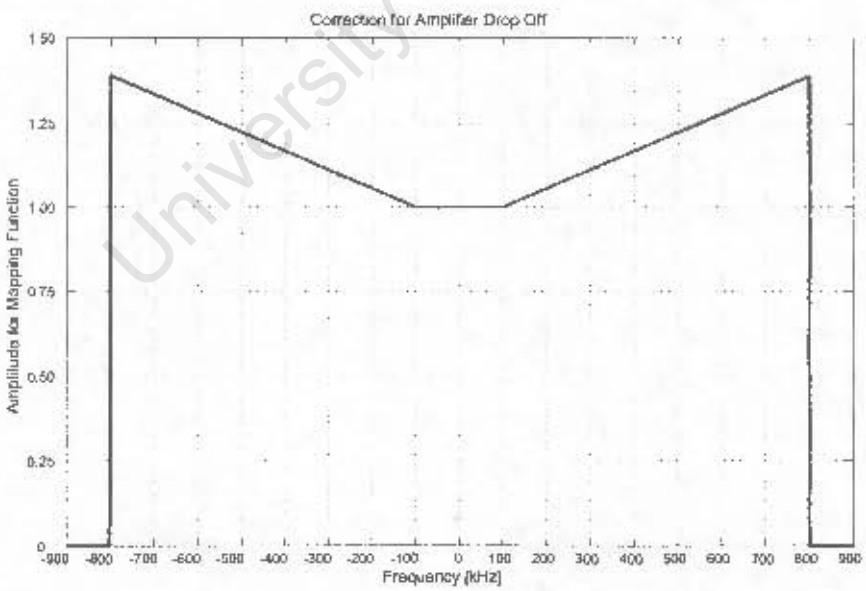

FIGURE 4-12. Mapping function to correct for amplifier drop off.

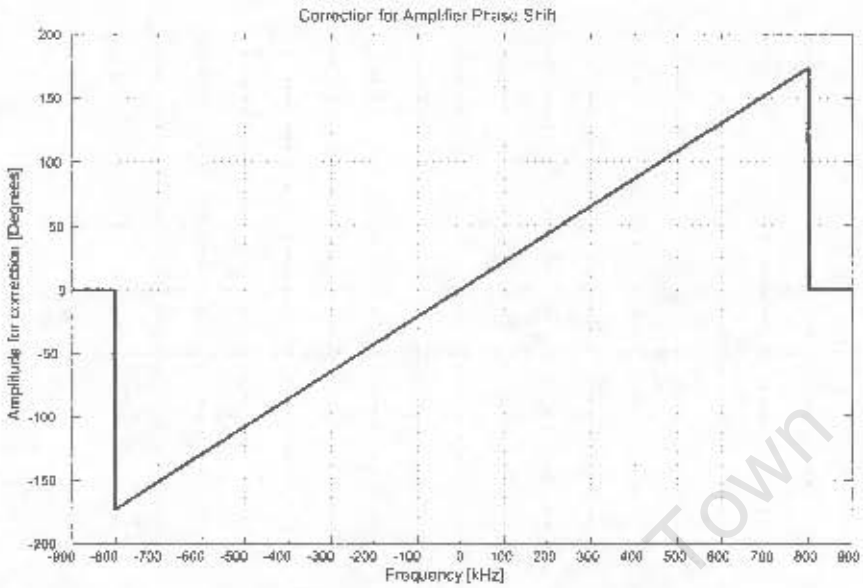

FIGURE 4-13. Mapping function to correct for amplifier phase shift.

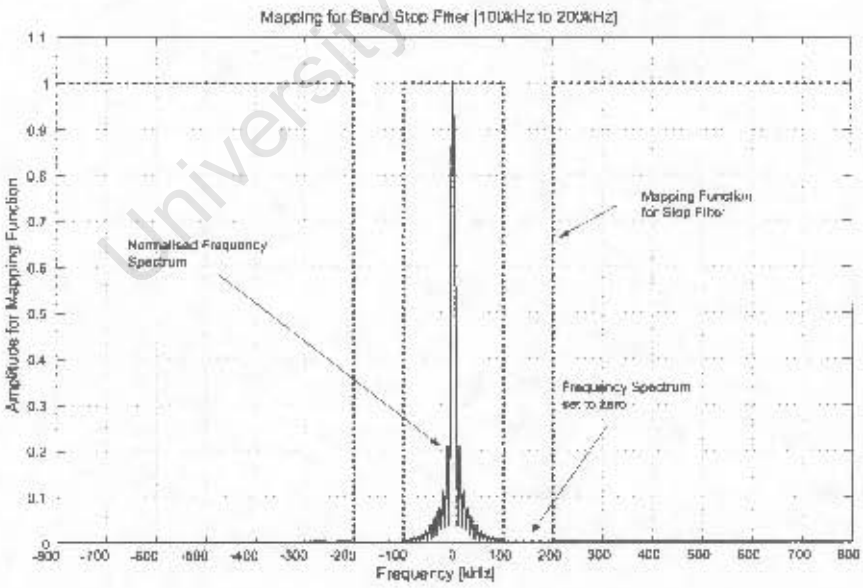

FIGURE 4-14. Mapping for Band Stop Filter [100kHz to 200kHz]

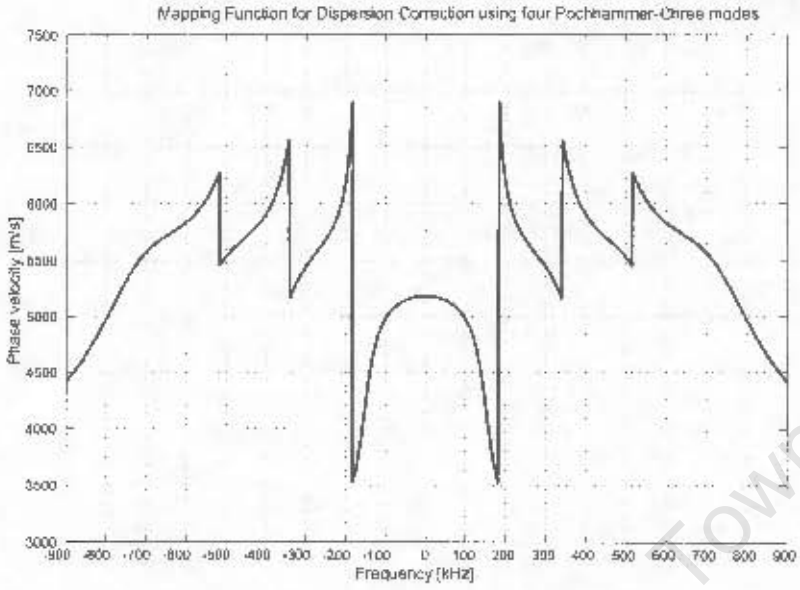

FIGURE 4-15. Mapping function for the dispersion correction using the first four Pochhammer-Chree modes

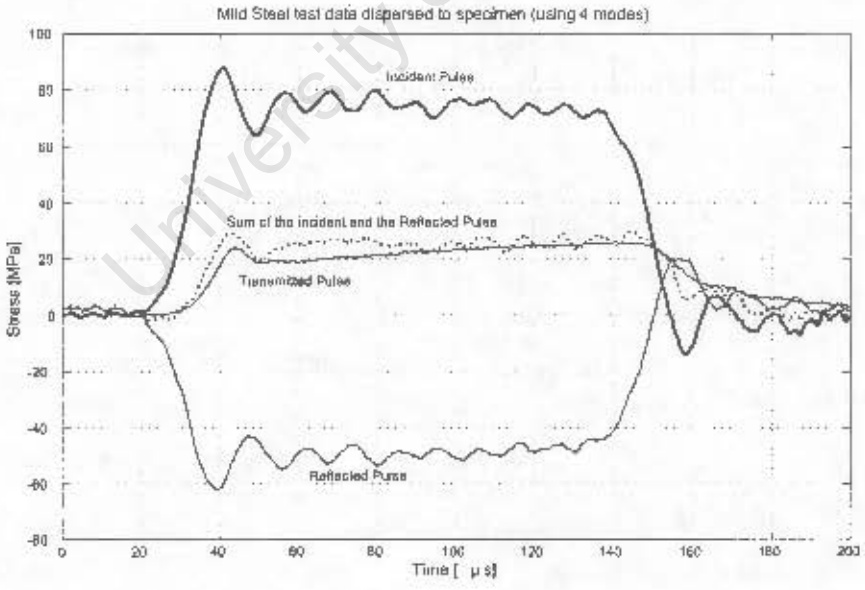

FIGURE 4-16. Mild Steel test data showing the incident and reflected pulse dispersed to the bar/specimen interface and the transmitted pulse undispersed to the specimen/bar interface.

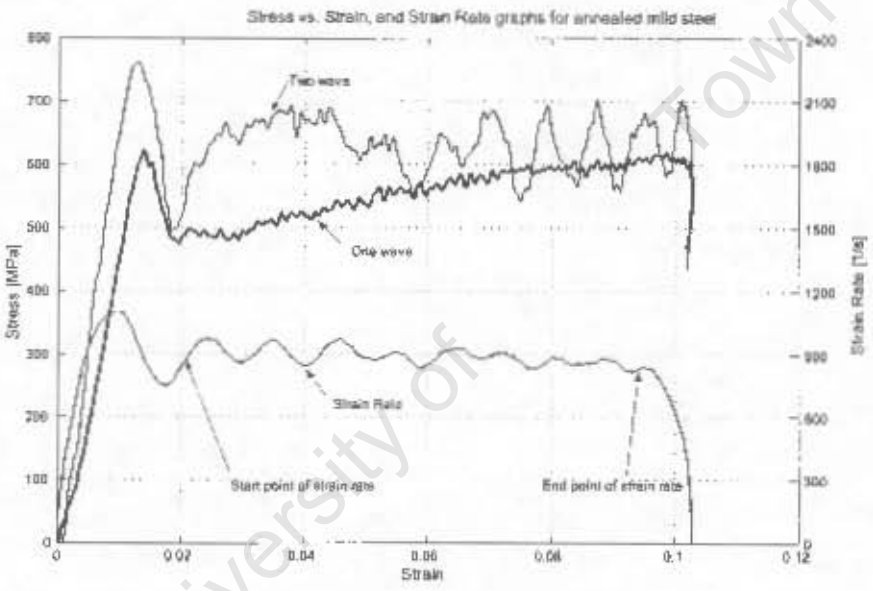

FIGURE 4-17. Stress vs. Strain, and Strain Rate graphs for annealed mild steel

5

Calibration of the SHPB System

5.1 Introduction

For meaningful interpretation of the material testing, it is necessary that the system be calibrated. This includes testing of the strain gauge amplifiers for gain drop-off and phase shift, so that any necessary corrections could be made. The speed trap had to be calibrated separately as it was then used in the calibration of the bars. The material constants for the bar (E and ν) have to be determined experimentally as they are used in determining the dynamic calibration factor, and in the dispersion correction program. After all of the above have been calibrated, the bars dynamic calibration factor can be determined. This final dynamic calibration factor was required to convert the voltage reading obtained, from the data acquisition system, to the appropriate stress level.

In this chapter the calibration of the above mentioned systems and constants are discussed. In addition the methods used to determine the Young's modulus and Poisson's ratio for the bar are described.

5.2 Calibration of Strain Gauge Bridge Amplifiers

The amplifier gain was tested by inputting a sinusoidal wave and noting the output response of the strain gauge bridge amplifier on a digital oscilloscope. The input frequency was adjusted from $10Hz$ to $1MHz$ to obtain the full frequency response of the amplifiers. The digital oscilloscope output indicates both the amplitude of the input as well as the output signal and from this the gain drop-off was determined. The phase difference between the two signals was also calculated by the digital oscilloscope.

A plot of the gain drop-off is shown in *Figure 5-1* and it can be seen that the amplifier gain is $1000V/V$ up to a frequency of approximately $100kHz$ as the data sheet indicated [48]. The gain then drops to 60% and 65% at a frequency of $800kHz$ for amplifiers 1 and

2. The correction function to restore the signal back up to a gain of 1000 is also shown with the corrected signal for the two amplifiers. *Figure 5-2* shows the phase shift of the two amplifiers and the corrected phase to restore the phase difference to zero. From these two figures it can be seen that the gain drop-off and the phase shift are corrected quite successfully by the correction functions, thereby improving the range of frequencies that can be used in the dispersion correction.

5.3 Calibration of the Data Acquisition Card

The zero and the maximum value ($+5V$) have to be set for each channel of the data acquisition card. The card calibration program is run and each channel is set individually. First, the zero is set by grounding the input and adjusting the multi-turn variable resistor on the card until the displayed value is zero. To set the maximum value, the input must be connected to a $+5V$ supply and then the variable resistor is adjusted on the card until the display reads $+5V$. The power supply that was used for the strain gauge bridge was used to set the card maximum. This was undertaken because the bridge reference voltage was important and by calibrating the card to the bridge voltage the two systems had a common reference voltage. Note that the card should be recalibrated every six months, or if it is removed from the PC. The calibration of the ADLINK PCI-9812 data acquisition card is covered in detail in the users manual [42].

5.4 Calibration of the Speed Trap

The gap between the two speed trap sensors was determined by installing the speed trap on the barrel in reverse, as explained below. The speed trap was installed in reverse because the triggering points of the infrared sensor are dependent from which side they are triggered. A micrometer depth gauge was inserted into the barrel until the first speed trap timing light was triggered. This was repeated several times to obtain an average for the depth. The depth gauge was then inserted until it triggered the second timing light. Again, this was repeated several times to obtain an average for the depth. The difference between the two measurements gave the distance between the two sensors. *Table 5.1* shows

the results of the calibration of the distance between the two sensors. After the test, the speed trap was turned around so that the striker would trigger the first sensor first.

Table 5.1 Calibration Results of Speed Trap

Distance to first sensor [mm]	15.49	15.44	15.50	15.45	15.46	15.47
Distance to second sensor [mm]	96.49	96.49	96.48	96.49	96.48	96.49
Distance between the sensors [mm]						81.02
Standard deviation of the average distance between the sensors [%]						0.0292

By taking three times the standard deviation of the average distance between the sensors and the specified error in the timer, the uncertainty in the speed reading was determined to be 0.1%

5.5 Determination of the Young's modulus and Poisson's ratio for the bars

In the dispersion correction program, the Young's modulus and Poisson's ratio for the bars have to be entered. Oscillations on the stress-strain plot will occur if the values for Young's modulus and Poisson's ratio are incorrect. These two constants have to be determined experimentally. Two methods, using the SHPB, for determining the Young's modulus and Poisson's ratio for the bar, are discussed below.

5.5.1 Two Strain Gauge Station Method

Two sets of strain gauges were cemented to each bar with a spacing of 500mm between them and 750mm from the ends of the bar. The bar was then struck with a 150mm striker and the signals from the two stations were recorded. A plot of two typical readings from the two strain gauge stations is shown in *Figure 5-3*. The reading from the first station was then dispersed to the second station with an assumed value of Young's modulus and Poisson's ratio. The manufacturer's value for Young's modulus, $210GPa$ was used as the start point. As Young's modulus affects the fundamental velocity ($C_p = \sqrt{\frac{E}{\rho}}$) of the pulse, it has the most effect on the position of the pulse. The Poisson's ratio has little effect on

the position of the pulse but influences the shape on the pulse. The Young's modulus was first adjusted until the two pulses were positioned on top of each other and then the Poisson's ratio was adjusted so that the first and second readings were the same shape.

Figure 5-4 shows the first reading shifted to the second reading, but with no dispersion correction. From this it can be seen that the main body of the pulses correlate, but the shape is not correct. This shows that the fundamental velocity is the dominant factor and the value for Young's modulus was correct. A plot of the two readings when the dispersion correction is applied to the first reading and shifted to the second reading is shown in *Figure 5-5*. As can be seen from this figure, the correlation between the two is good, indicating that the Young's modulus and Poisson's ratio values are correct. This method has the drawback that the two pulses overlapped and this made determination of Poisson's ratio by visual inspection difficult, which led to errors in the determination of the value for Poisson's ratio. There was little difference in the image when using a value for Poisson's ratio of 0.25 or 0.26.

The two strain gauge station method also allowed for the testing of the calibration of the amplifiers as the momentum for the two pulses should be the same. *Figure 5-3* also shows a trace of the momentum of the pulse. *Table 5.2* below shows the values of the momentum and energy calculation for the two pulses. From *Figure 5-3* and *Table 5.2* it can be seen that the momentum is conserved as the error between the two stations is only 0.08%. The energy calculation shows that there is energy lost in the bar as the pulse moves down it.

Table 5.2 Momentum and Energy of Two Consecutive Pulse

Momentum Channel 0 =	0.8459 N.s
Momentum Channel 1 =	0.8466 N.s
Error in Momentum between the two Channels =	**0.08%**
Energy Channel 0 =	0.9012 J
Energy Channel 1 =	0.8817 J
Error in Energy between the two Channels =	**2.21%**

This test was conducted five times and the average error in momentum was 0.1%. The amplifiers were then switched between the two stations and the test repeated. The average error in momentum was again only 0.1%. This indicated that the amplifier had the same gain, confirming the test done with the signal generator.

5.5.2 One Strain Gauge Station Method

In this method, when calibrating the bar one end is struck by the striker and the other end is free. Therefore the stress at the free end of the bar should be zero. If the incident pulse was dispersed to the free end and the reflected pulse undispersed to the free end, then the sum of the two should be zero. For this test the strain gauge was placed in the middle of the bar and struck with a 300mm striker. The trace from the single strain gauge station is shown in *Figure 5-6*. The incident pulse in *Figure 5-6* is in effect shifted to the right and dispersed, and the first reflected pulse shifted to the left and undispersed. The plot of the summation of the two pulses at the free end indicates if the value for Young's modulus and Poisson's ratio are correct.

The value for Young's modulus was first adjusted until the summation trace was almost zero. The value for Poisson's ratio was then adjusted. After several iterations the summation trace was almost zero and the final value for Young's modulus was $211GPa$ and Poisson's ratio was 0.26. A plot of the stress at the end of the bar using $E = 211GPa$ and $\nu = 0.26$ is shown in *Figure 5-7*. The slight oscillation in the beginning and the end of the pulse could not be removed by further adjustment of the Young's modulus and Poisson's ratio. These oscillations could be the result of end effects which are not corrected for by the standard dispersion correction technique. Note that when the correct value for Young's modulus and Poisson's ratio are used, the incident and reflected pulse cross on the zero line at the rear of the pulse.

A plot of the two pulses shifted to the free end of the bar is shown in *Figure 5-8*. The correct value of Young's modulus is used for this shift but no dispersion correction is implemented, this results in large oscillation on the summation plot. In addition, note that where the three traces cross at the rear of the pulse, they do not cross on the zero mark.

The next three figures (*5-9 - 5-11*) show the effect on the stress at the end on the bar due to the incorrect selection of Young's modulus and Poisson's ratio. When the Young's modulus is changed to $213GPa$, there is only a 1% change in the Young's modulus, whilst the Poisson's ratio remains at 0.26. There are however large oscillations in the summation pulse and the two pulses do not cross at zero at the rear of the pulse indicating the incorrect value of Young's modulus. This can be seen in *Figure 5-9*. *Figures 5-10* and *5-11* are plots of the stress at the end of the bar with the correct value of Young's modulus ($E = 211GPa$) but the Poisson's ratio has been changed to 0.24 and 0.30 respectively. Note that both curves have oscillations but the crossing of the incident and reflected pulse are almost on the zero mark. This again shows that the value Young's modulus has a larger effect than the Poisson's ratio.

This method of plotting the summation of the stresses at the end of the bar proved to be more effective in determining the values of Young's modulus and Poisson's ratio than moving one pulse onto another. Several tests were conducted for both bars and the Young's modulus for the two bars only differed by $0.25GPa$.

5.6 Determining the Calibration Factor of the System

5.6.1 Theoretical Calibration Factor

The theoretical calibration factor is the calculated constant that relates the logged voltage to the stress in the bar. This is determined as follows: The strain reading in the bar was determined from the strain gauge factor, strain gauge bridge voltage and the gain of the amplifiers [49][50]. As the bars do not go plastic, the stress in the bar could be calculated by multiplying the strain by Young's modulus ($\sigma = E\varepsilon$). The theoretical calibration factor was used as the starting point when determining the dynamic calibration factor.

5.6.2 Dynamic Calibration Factor

One method of determining the dynamic calibration factor of the bar was to determine the average value of strain in the strain-time pulse from the striker incident velocity [7][12]. As there are oscillations on the pulse, this method requires the user to be subjective when

determining the average value of the pulse. This method works if a long striker can be used for calibration as the average can then be determined more objectively. The gas vents for the barrel of the current system were only 200mm long. This limits the length of the striker that can be used for the calibration, as the striker would still be accelerating through the speed trap if it was too long. With this limitation only a 100mm long striker could used for the calibration tests. By using a 100mm striker the length of the pulse in the bar was too short to get an accurate estimate of the average strain value of the pulse, thus making this method too unreliable.

An alternative method was to use the energy and momentum of the pulse [3]. This method is advantageous as the values for the energy and momentum are determined by integrating the strain-time pulse so the need to estimate the average value is eliminated.

5.6.2.1 Calculation of the momentum and energy in a pulse.

Free body diagram of a section in the bar

The stress at a point in the bar is $\sigma(t) = E\varepsilon(t)$ and from this the force in the bar is $P(t) = A_{Bar}E\varepsilon(t)$. From the force, the impulse can be determined as

$$\begin{aligned} I &= \int_0^t P(t)\,dt \\ &= \int_0^t A_{Bar}E\varepsilon(t)\,dt \\ &= A_{Bar}E\int_0^t \varepsilon(t)\,dt. \end{aligned} \tag{5.1}$$

Energy can then be determined from the force in the bar and the velocity of the particles of the bar subjected to the pulse .($v(t) = \frac{E\varepsilon(t)}{\rho C_0}$).

$$\begin{aligned} Energy &= \int_0^t P(t)\, v(t)\, dt \\ &= \int_0^t A_{Bar} E\varepsilon(t) \times \frac{E\varepsilon(t)}{\rho C_0} dt \\ &= \frac{A_{Bar} E^2}{\rho C_0} \int_0^t \varepsilon(t)^2\, dt. \end{aligned} \tag{5.2}$$

In both the impulse and energy calculations the change in the area of the bar was very small and assumed to be constant.

5.6.2.2 *Method for determining the dynamic calibration factor from the energy and momentum of the pulse*

The dynamic calibration factor of the bar was determined by assuming a calibration factor and then calculating the energy and momentum of the pulse. From energy and momentum the incident velocity of the striker was then calculated. The initial starting point was the theoretical calibration factor, as the two should not be significantly different. The calibration factor was then adjusted until the calculated incident velocity of the striker matched the measured velocity. The derivation below shows how the incident velocity was obtained from the energy and momentum of the pulse.

The change in momentum in the striker was equal the momentum to the bar

$$\Delta I = m(v_i - v_r) = I_{bar}, \tag{5.3}$$

and the change in energy in the striker was equal to the energy in the bar (assuming the losses are small)

$$\Delta \mathrm{E} = m\left(v_i^2 - v_r^2\right) = \mathrm{E}_{bar} \tag{5.4}$$

With v_i = incident velocity, v_r = reflected velocity and m = mass of the striker. As the

reflected velocity was not measured. *Equation 5.3* is rearranged to make v_r the subject and substituted into *Equation 5.4* giving:

$$v_i = \frac{E_{bar}}{I_{bar}} + \frac{I_{bar}}{2m} \tag{5.5}$$

The 100mm striker was fired 15 times at each bar and the results are shown in the *Table 5.3* below.

Table 5.3 Results of dynamic calibration

Theoretical Calculated Calibration factor =	$14.41 MPa/V$
Average Dynamic Calibration factor =	$15.20 MPa/V$
Standard Deviation on Dynamic Calibration factor =	$0.1695 MPa/V$
Standard Deviation as a Percentage of Average Dynamic Calibration factor =	1.115%
Average Error between Dynamic and Theoretical Calibration factor =	5.47%

As can be seen from the above results there is a 5.47% error between the two methods. This could be due to:

- Energy lost in the collision of the striker due to local plasticity, noise and heat.
- Energy loss in the bar as the pulse travels down it.
- Error in the gauge factor of the strain gauge.
- Error in the gain of the amplifier.
- Error in the gauge bonding and alignment.

The calibration tests were performed at a strain gauge bridge voltage of $\pm 7V$ and as the bridge voltage is adjustable it was necessary to scale the calibration factor accordingly. The scaling factor was determined by calculating the theoretical calibration factor at the bridge voltages for $\pm 1V$ to $\pm 20V$ and then the percentage change between the calibration voltage and the bridge voltage was plotted. The dynamic calibration factor was then scaled according to the percentage change. This scaling was incorporated into the *Excel*

spreadsheet to adjust automatically the calibration factor when the bridge voltage was adjusted.

5.7 Summary

In this chapter the calibration of the SHPB system has been dealt with. This included the testing for amplifier gain and phase shift, and correction to bring the amplifier gain up to $1000V/V$ and phase shift back to zero. A brief description of the calibration of the data acquisition card and the speed trap had also been given. Two methods for fine tuning Young's modulus and Poisson's ratio have been discussed and the final value for Young's modulus and Poisson's ratio were set at $211GPa$ and 0.26 respectively. The dynamic calibration factor was determined and the method to scale the calibration factor to take into account the adjustable bridge voltage was given.

As the system was functioning correctly and calibrated, material testing could be undertaken to validate the setup. The chapter which follows incorporates the results of the material tests conducted. Operation of the experimental equipment and the data processing are also discussed.

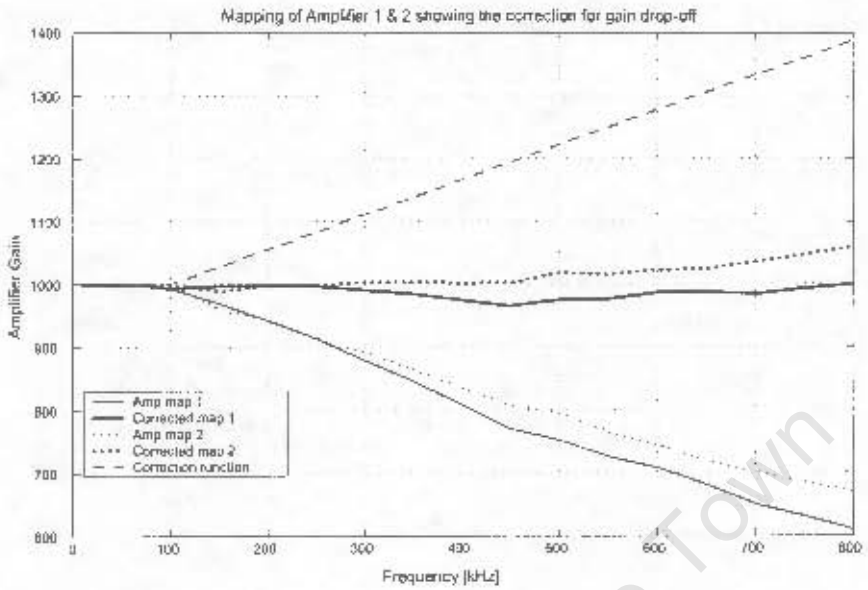

FIGURE 5-1. Mapping of amplifier 1 & 2 showing the correction for gain drop-off

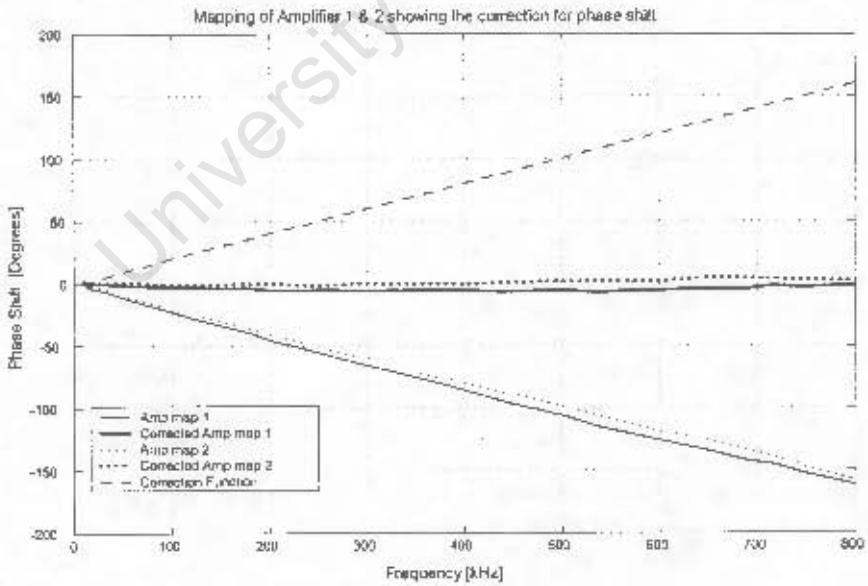

FIGURE 5-2. Mapping of amplifier 1 & 2 showing the correction for phase shift

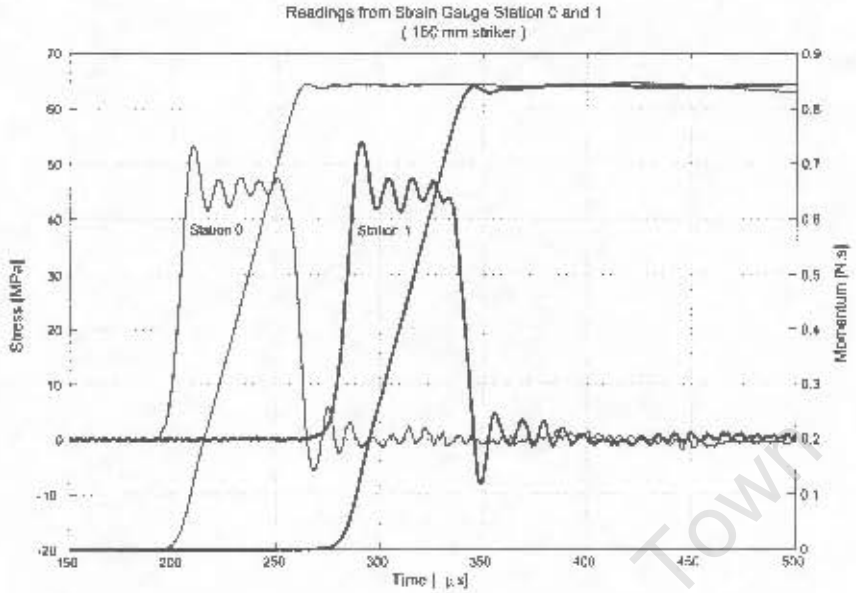

FIGURE 5-3. Readings from Strain Gauge Station 0 and 1 when the incident bar was struck by a 150 mm striker showing the conservation of momentum.

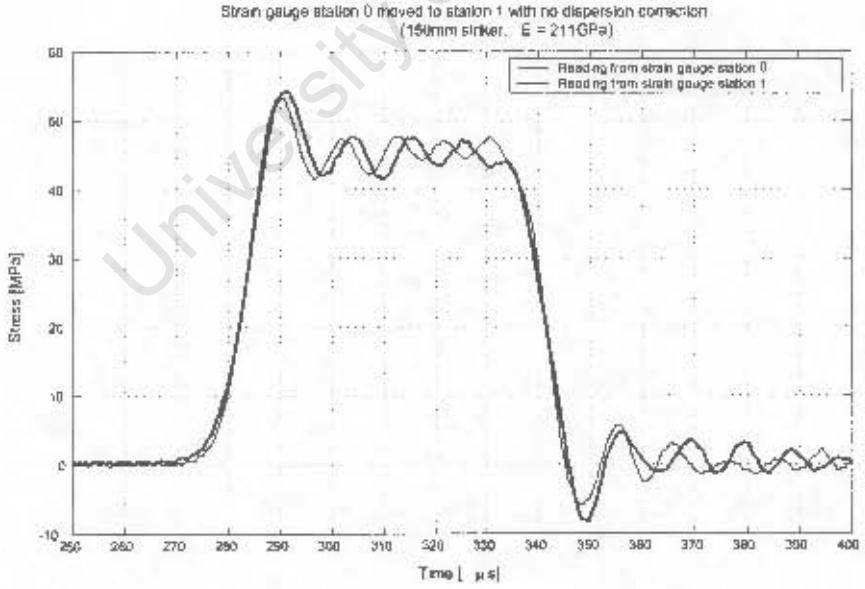

FIGURE 5-4. Strain gauge station 0 moved to station 1 with no dispersion correction ($150mm$ striker, $E = 211GPa$)

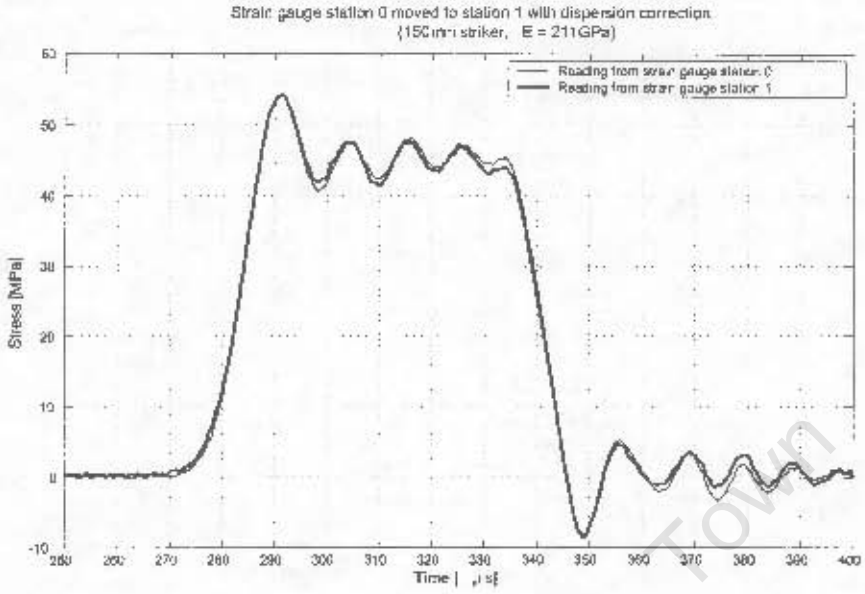

FIGURE 5-5. Strain gauge station 0 moved to station 1 with dispersion correction (150mm striker, $E = 211GPa$ and $\nu = 0.26$)

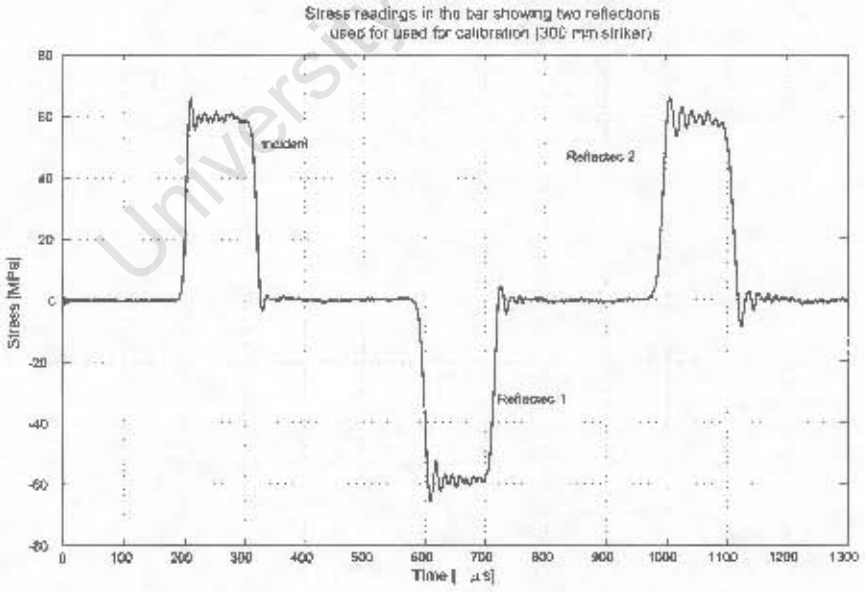

FIGURE 5-6. Stress readings in the bar showing two reflections used for calibration.

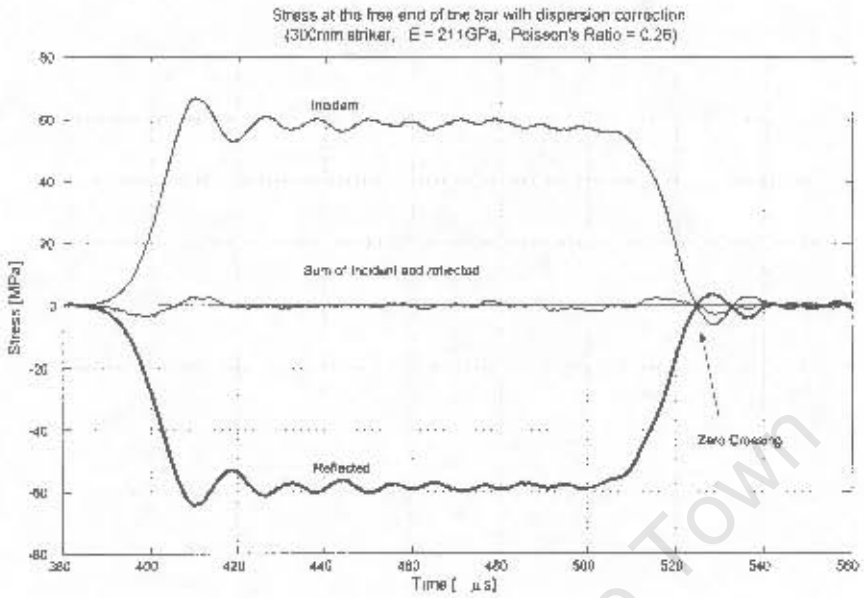

FIGURE 5-7. Stress at the free end of the bar with dispersion correction ($E = 211GPa$, $\nu = 0.26$)

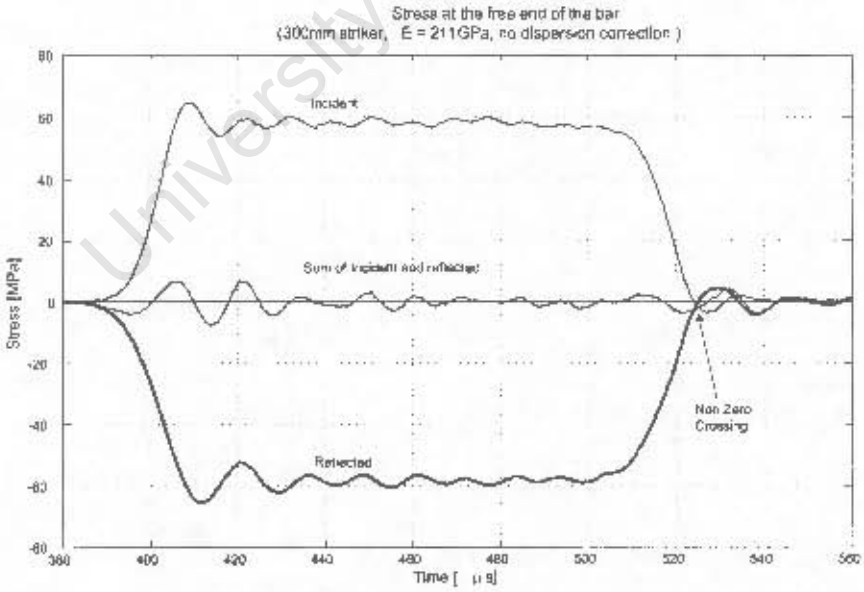

FIGURE 5-8. Stress at the free end of the bar with no dispersion correction ($E = 211GPa$)

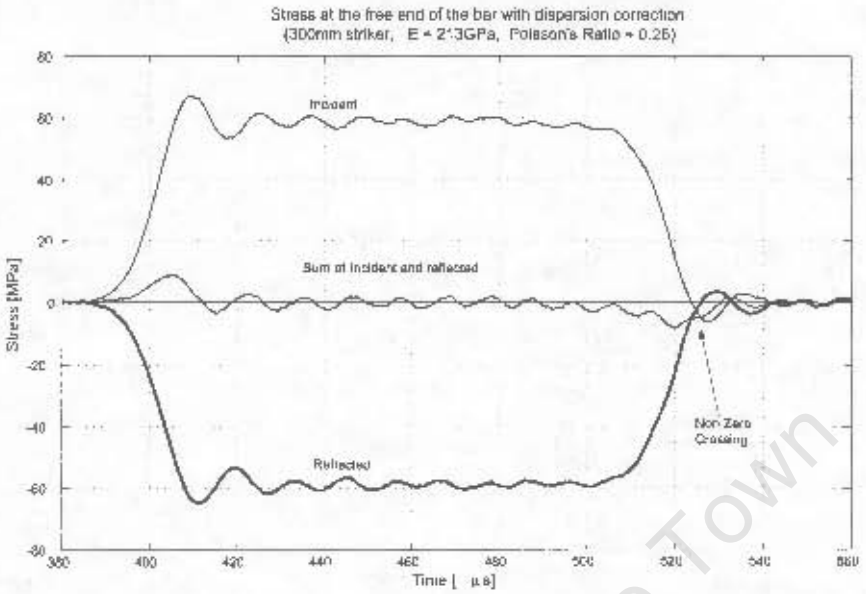

FIGURE 5-9. Stress at the free end of the bar with dispersion correction ($E = 213GPa$, $\nu = 0.26$)

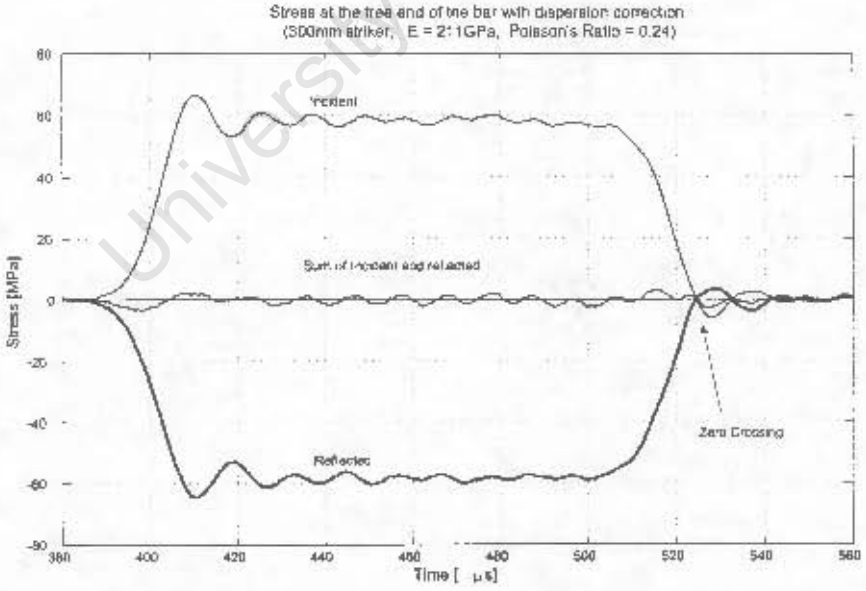

FIGURE 5-10. Stress at the free end of the bar with dispersion correction ($E = 211GPa$, $\nu = 0.24$)

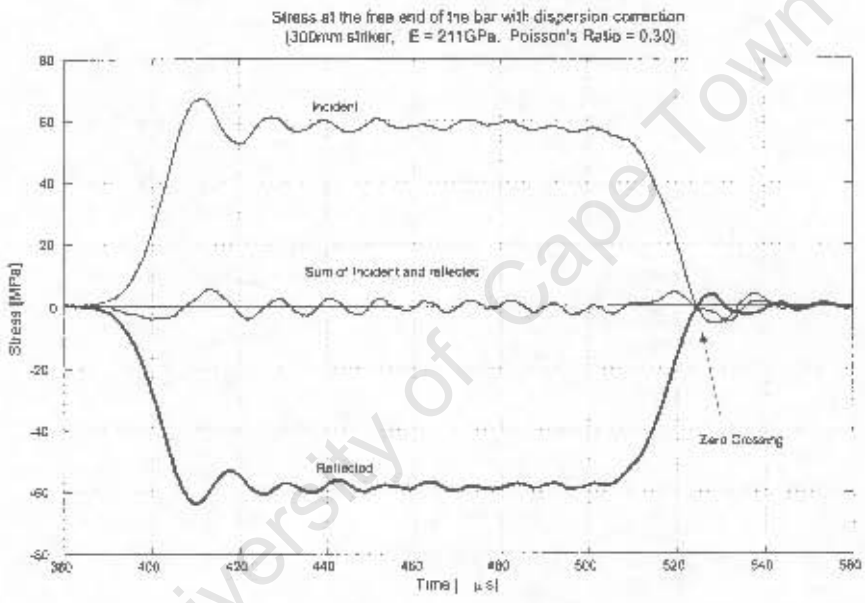

FIGURE 5-11. Stress at the free end of the bar with dispersion correction ($E = 211GPa$, $\nu = 0.30$)

6

Results and Discussion

6.1 Introduction

To test the SHPB system, three materials were tested and the results compared to constitutive models and published results. In this chapter the results of the tests conducted are presented and discussed, together with comments about the operation of the experimental equipment. This includes the operation of the gas gun system, the alignment of the bars, strain gauge bridge amplifiers and the calibration of the system. Finally, the data processing is reviewed.

6.2 Experimental Equipment

6.2.1 Operation of the Gas Gun System

The gas gun operation was simple and easy to use. There were however, some problems that were encountered when running the tests, these being:

- The barrel diameter was 12.7mm which restricted the striker diameter. This lead to the stress in the striker being higher than that of the bar and for high striker velocities the striker could go plastic. This limited the striker speed during the calibration test as the calibration method used was not valid when the striker went plastic.

- The barrel was too short to cut long gas vents. This then limited the length of the striker that could be used for calibration tests to 100mm, which resulted in inaccuracy for one of the calibration methods.

- The valving and barrel were designed to run at high velocities. This resulted in some scatter and poor reproducibility of the striker velocity, for the low velocity range.

6.2.2 Alignment of the Bars

The method for adjusting the bar position was simple to use and set (see *Section 3.2.2.6*). The alignment of the bars by eye was up to the interpretation of the operator. This resulted in no set method to ensure that the system was aligned, but the technique used was regarded as acceptable.

6.2.3 Strain Gauge Bridge Amplifiers

The strain gauge bridge amplifiers worked well for such a simple circuit. Only a small amount of noise in the signal could be attributed to the amplifiers. This noise could be further reduced if the circuit was mounted on a printed circuit board and not on vera-board. The zero setting of the strain gauge bridge was achieved by adjusting the multi-turn variable resistor that was mounted on the vera-board. This adjustment proved to be finicky as a small screw driver had to be inserted into a hole on the side of the amplifier box.

Having the gain set at $1000V/V$ and adjusting the bridge voltage for both amplifiers together, had limitations. *Figure 6-1* shows a typical incident pulse and the consequent transmitted pulse for the different materials tested using such an incident pulse. The level of the transmitted pulse is dependent on the type of material being tested and the size of the specimen. If large strains were needed in the specimen, for a given striker length, the specimen diameter had to be small compared to that of the bar, as the stress in the bars was limited to $100MPa$. This resulted in the magnitude of the transmitted pulse being low. From *Figure 6-1* it can be seen that if the bridge voltage was set so that the incident pulse would use the full rage of the data acquisition card, then the transmitted pulse would only use a fraction of the full range.

6.2.4 Data Acquisition System

The *ADLINK PCI-9812* data acquisition card was capable of capturing more data than was necessary for the tests that were conducted. For the normal test, the card was set on $10MHz$ and the number of samples set to 15000 per channel. At this setting the card was operating at half it's maximum sample rate and only at a small fraction of the sample capacity (Max sample is 64 M bytes [42]).

The *Visual Basic* user interface proved to be more than adequate for capturing the signal. It was simple to use and required little time to train an operator. The logging of all the additional data, such as the specimen dimensions and time of the speed trap, together with the signal voltage reading, made filing the test data simple and effective as all the information was maintained on one TXT file and not on loose paper.

6.2.5 Calibration of the System

The momentum and energy method used for calibration of the system proved to be repeatable with a standard deviation of 1.115%. From this method, the dynamic calibration factor was determined to be $15.20 MPa/V$ which only differed from the theoretical calibration factor by 5%.

The calibration between the two strain gauge stations could be checked during testing of material specimens as the momentum should be conserved. If there was a deviation between the two stations momentum, this would indicate an error and the system needed to be checked. For each test the momentum was checked and a typical test result for an annealed mild steel test is shown in *Figure 6-2*. For this test the error between the momentum of the incident and the sum of the absolute value of the reflected and the transmitted pulse was 0.1%. This was typical for this calibration test.

An additional feature of the calibration spreadsheet was the calculation of the energy for the three pulses captured. *Figure 6-3* shows the energy trace of the afore mentioned mild steel material test. From this the energy absorbed by the specimen could be determined and an estimate for the maximum temperature rise could be determined. The temperature rise was calculated as follows:

- From the dimensions and density, the mass of the of the specimen was determined $[kg]$.
- The energy in the transmitted and reflected pulses was subtracted from the energy in the incident pulse. This gave the maximum energy that the specimen could have absorbed $[J]$.

- By dividing the energy absorbed $[J]$ by the specimen by specific heat $[kJ/kg.^{\circ}C]$ and the mass $[kg]$, the change in temperature of the specimen was determined.
- By measuring the temperature of the specimen before the test, the final temperature could be determined by adding the change in temperature to the measuring the temperature.

6.3 Data Processing

6.3.1 Comparison between results that were corrected for dispersion and those without correction

To illustrate the effect that dispersion correction had on the three pulses (incident, reflected and transmitted) and finally on the stress-strain curve, an annealed mild steel test was processed with and without dispersion correction. When dispersion correction was implemented the first four Pochhammer-Chree modes were used. *Figure 6-4* shows a plot of the incident, reflected and transmitted pulse shifted to the bar specimen interface with and without dispersion correction being implemented. From *Figure 6-4* it can be seen that the incident and reflected pulses are affected significantly by the dispersion but the transmitted pulse to a lesser degree. This is a result of the larger quantity of higher frequency components present in the incident and reflected pulses. These higher frequency components are strongly affected by dispersion. The specimen does not allow the higher frequency components to be transferred to the transmitter bar, as they are plastically damped by the specimen, and thus the transmitted pulse does not suffer from dispersion as much.

From the set of corrected pulses the stress-strain curve was determined. *Figure 6-5 a)* presents a plot of the stress-strain curves generated for the three pulses that were not corrected for dispersion. The curve generated from the incident and reflected pulse has very large oscillations. The curve could not be used even if it were averaged as the curve would not represent the true shape. The curve generated from the transmitted pulse does have oscillations in the beginning but these settle down towards the end of the curve. The

oscillations at the beginning of the pulse are too large to smooth out by averaging as this would then alter the magnitude of the first peak which should be present.

Figure 6-5 b) shows the stress-strain curve when dispersion correction was implemented. From *Figure 6-5 b)* it can be seen that the stress-strain curve generated from the incident and reflected pulses have large oscillations. This curve does deviate in the beginning from the stress-strain curve generated from the transmitted pulse, but then settled down. If a longer striker were used, the stress-strain curve generated from the incident and reflected pulse could be averaged and should follow the curve from the transmitted pulse. These oscillations could also be reduced if the incident pulse was "pulse shaped" [7][51] (see *Section 6.3.2*). This is achieved by placing a thin piece of material, copper shim, at the end of the incident bar to absorb the higher frequency components, by increasing the rise time of the incident pulse. The stress-strain curve generated from the transmitted pulse has only minor oscillations. By smoothing the pulse these can be removed without altering the overall shape of the curve.

To show the effect of data processing with and without dispersion correction, the stress-strain curves generated by using the transmitted pulse were overlapped. From *Figure 6-5 c)* it can be seen that the two curves follow very similar lines, but there are differences especially at the beginning of the curve. The differences being:

- The rise of the corrected curve is sharper and this moves the peak of the yield point.
- The maximum value of the peak is also lower on the corrected curve.
- After the first peak there are oscillations on the uncorrected curve but these die out towards the end of the curve.

6.3.2 Pulse Shaping

At the end of the testing phase of the project, additional tests were undertaken to show the effects of pulse shaping on the incident pulse and the stress-strain curve. *Figure 6-6 a.* shows the incident, reflected and transmitted pulse dispersed to the bar specimen interface of an as worked copper specimen. As can be seen the three pulses show little oscillation. The

curve of the sum of the incident and reflected pulses follows that of the transmitted pulse reasonably well after an initial settling down period. *Figure 6-6 b.* shows the stress-strain curve generated from the three pulses and it can be seen that the oscillations previously present on the "Two wave" curve are considerably reduced. The two stress-strain curves converge more rapidly, compared with those lacking pulse shaping and the strain rate exhibits only small oscillations after the load up period. The convergence time of the two stress-strain curves was investigated by Wu and Gorham [51]. They showed that the inertia of the specimen strongly affected the time for the two curves to converge. By reducing the length to diameter ratio the two curves converged faster but there was a limit as frictional affects are increased.

6.3.3 The use of Higher Modes for Dispersion Correction

The higher Pochhammer-Chree modes were incorporated to improve the shape of the pulse and thus improve the shape of the stress-strain curve. To test this, an incident pulse was dispersed to the bar specimen interface using only the first mode and then subsequently using the first four modes. *Figure 6-7* shows that there is little difference between the two and only by zooming in on a section of the pulse can the difference be seen. The reason for this small difference was investigated further by looking at how much energy each mode contained. The pulse in *Figure 6-7* was transformed, with the FFT, into the frequency domain. The normalized magnitude spectrum was then plotted. The energy contained in each frequency was then progressively added up and plotted. Note the plot of the energy takes the zeroth term and then adds twice the energy in the following frequency terms. This is done to take into account the negative frequency components. In addition to this the first and first four Pochhammer-Chree modes are plotted.

From *Figure 6-8* it can be seen that the magnitude spectrum dies out rapidly and by $100kHz$ it is almost zero. From the plot of the energy it can be seen the the first mode contains 94.8% of the energy and the higher modes only 5.2%. This shows that the first mode dominates the dispersion correction which is in agreement with published investigations [21][28][30][32]. If the incident pulse was "pulse shaped" there would be hardly any energy contained in the high modes.

If explosives were used to load the bar, the rise time would be very short. This would lead to a larger amount of higher frequency components being generated. In this case, use of the higher Pochhammer-Chree modes would be required to correct for dispersion for this type of loading [33]. In addition to this, as the diameter of the bars increases the frequency at which one mode switched to the next decreases, as shown in *Figure 6-9*.

6.3.4 Correction for Gain Drop-off and Phase Shift

The effects of correcting for gain drop-off and phase shift were tested by overlapping two pulses, one corrected and the other not. The effect could only be seen by zooming into a section on the plot. This can be explained by looking at the amount of energy in the pulse that is being affected by the gain drop-off and phase shift. The gain drop-off starts at $100kHz$ and there is little phase shift up to $100kHz$ (see *Section 5.2*). From *Figure 6-8* it can be seen than 92% of the energy in the pulse is contained between $0Hz$ and $100kHz$. This meant that the gain drop-off and phase shift only affect 8% of the energy of the pulse and thus may be regarded as a small effect.

Note that the gain drop-off and phase shift correction only takes into account the response of the amplifier and not that of the strain gauge. Ueba [52] noted that for frequencies up to $100kHz$ there is little effect on the performance of the strain gauge. The testing of the response of the strain gauge was beyond the scope of this project.

6.3.5 Effect of Sample Frequency on the Dispersion Correction

The cut off frequency used was $800kHz$. This meant that the minimum sample frequency according to the Nyquist sampling theory is $1.6MHz$ [29]. This is not the only factor that had to be considered when selecting the sample frequency. When performing a time shift, the time by which the pulse must be moved must be divisible by the sampling time, i.e. one can only move a data point to the location of another data point. If this requirement is not met there will be an error in the shape of the pulse after the time shift. The maximum distortion in the pulse occurs when the time step of the shift lands midway between a sample time.

For dispersion correction the time of the time shift is not a fixed number as it is depen-

dent on phase velocity, which is frequency dependent. This means that it is not possible to step to the correct location as the time interval will not always be divisible by the sampling time. To reduce the error resulting from the incorrect time step, the sample frequency is increased. Tests were conducted to assess the required sample frequency and at $5MHz$ it was not possible to see the error caused by the incorrect time step. From this the sample frequency of $10MHz$ was selected to take into account any other factors.

6.4 Material Tests

6.4.1 Compression Test Results for Material Tested on the SHPB

All dynamic compression testing was undertaken using a ϕ10mm×300mm long striker. The stress level for the incident pulse was kept as close to a given level (85MPa) for the largest strain rate for each material. The stress level was then reduced by reducing the depth that the striker was pushed into the barrel, thus reducing the impact velocity.

Three materials were tested to evaluate the performance the SHPB. These were copper in the as received and the annealed condition, mild steel (EN1A) in the as received and the annealed condition and aluminum (6061-T6) in the as received condition. *Figure 6-10* shows selected test results for the all the dynamic compression tests conducted. Note that for the results shown in *Figure 6-10* only the stress-strain curve obtained from the transmitted pulse was used. The 'one wave' curve was used as it gives a representation of the stress state for the specimen [51][53]. The detail graphs for each material can be found in *Appendix B*.

From *Figure 6-10* it can be seen that there is a large difference in the stress-strain behavior between materials in the as received compared to those annealed condition. This indicates that the materials flow stress is higher in the as received condition, which was expected. By keeping the stress level constant for the largest strain rate for each material, it can be seen that the softer material strained more in the annealed condition than in the as worked condition. All three of the materials showed slight strain rate sensitivity, with the annealed mild steel being the most sensitive. This could be seen in the large increase of the upper and lower yield point as the strain rate increased.

6.4.2 Quasi-Static Tensile Test Results

Quasi-static tensile tests were conducted on the three materials according to BS-18, with six tests per material being conducted. Typical results for each material are shown in *Figure 6-11*. The detailed graphs for each material can be found in *Appendix B*. From *Figure 6-11* it can be seen that the three materials have the same general shape as the test results for the high strain rate tests, however the stress levels are lower in the tensile test, which was expected.

6.4.3 Comparison between the Test Data and the Johnson-Cook Model for Copper

The high strain rate tests on copper test were compared to Johnson-Cook constitutive model [2]. This model was selected as there were published constitutive constants available and the generation of constants for other models was beyond the scope of this project. The constitutive constants used in *Equation 6.1* were $A = 90MPa$, $B = 292MPa$, $n = 0.31$, $C = 0.025$ and $m = 1.09$ as taken from Johnson[2].

$$\sigma = [A + B\varepsilon^n][1 + C\ln\dot{\varepsilon}^*][1 - T^{*m}] \tag{6.1}$$

Figure 6-12 shows the dynamic compression test data as well as the quasi-static tensile test data for copper. Also plotted is the Johnson-Cook constitutive model for strain rates of $308s^{-1}$ and $1160s^{-1}$. From *Figure 6-12* it can be seen that the Johnson-Cook model deviates substantially at the low strains from the annealed dynamic compression test data, but at the higher strains the two start to converge. It can also be seen that the degree of strain rate sensitivity for the dynamic compression test and the Johnson-Cook model are quite similar. The annealing conditions could also have resulted in the stress level being lower. The annealing utilised for specimens of size ϕ4 x 3mm long, entailed being held at $450°C$, for 10 minutes, and allowed to cool in the oven. From *Figure 6-12* it can be seen that the Johnson-Cook model lies between that of the as received and annealed test results indicating that if the specimens had been only partially cold worked the stress level would probably have been higher.

The effect of heating of the specimen during the test was investigated. This was done to see if a rise in temperature could be the cause of the deviation between the model and the dynamic compression test. The maximum temperature that the specimen could have reached was calculated by determining the maximum energy that the specimen could have absorbed. From the maximum energy, the temperature was determined to rise from room temperature, $20°C$, to $30°C$. The results of the calculations can be seen in *Table 6.1*. This change in temperature could not have changed the stress level substantially and was subsequently ignored. Also added to the plots are curves of the Johnson-Cook model at temperature of $250°C$ for strain rates of $308s^{-1}$ and $1160s^{-1}$. They were added to show the it would require the temperature rise to $250°C$ before any noticeable change in stress level.

Table 6.1 Calculation results for maximum rise in temperature

Description	Value	Units
Energy in incident pulse	4.632	J
Energy in reflected pulse	3.453	J
Energy in transmitted pulse	0.064	J
Energy absorbed in specimen	1.114	J
Length of specimen	2.95	mm
Diameter of specimen	3.9	mm
Area of specimen	1.1945E-05	mm^2
Density	8954	kg/m^2
Mass	3.155E-04	kg
Specific heat	383.1	$J/kg.°C$
Maximum change in temperature	9.221	$°C$
Laboratory temperature	20.5	$°C$
Maximin temperature of specimen	29.2	$°C$

The annealed quasi-static and dynamic test data was then compared to published results. First dynamic test data was compared to published dynamic test data, at a strain

rate of $451s^{-1}$, by Zerilli [54]. The points published be Zerilli were plotted over the dynamic test data and are shown in *Figure 6-13*. From *Figure 6-13* is can be seen that the published curve shows close correlation with the test data. The next published results were generated by Follansbee [55]. The quasi-static results were compared and it can seen that the published stress strain curve by Follansbee is marginally higher and is shown in *Figure 6-13*. The dynamic test stress strain curve published by Follansbee, at a strain rate of $1800s^{-1}$, was slightly lower than the test data but had a similar trend. The deviation between the test data and the published data was deemed to be within acceptable limits. The deviation could be the result of different annealing conditions as Follansbee annealed at $600°C$ in a vacuum for 1h compared to the present test specimens which were annealed at $450°C$ for only 10 minutes.

6.4.4 Comparison between the Test Data with that of Published Results and the Cowper-Symonds Model for Mild Steel

The mild steel tests were compared using the Cowper-Symonds constitutive model. This model was selected as there were published constitutive constants available for mild steel. A plot of the dynamic compression test data and the quasi-static tensile test data is given in *Figure 6-14*. The mild steel dynamic test with strain rates of $360s^{-1}$ and $918s^{-1}$, and the tensile test (strain rate = $0.001s^{-1}$) were scaled using various constitutive constants for *Equation 6.2* to a reference strain rate of $1 \times 10^{-4}s^{-1}$ and then plotted. By scaling the test data to this references strain rate, the model could be tested as the lower yield point of the quasi-static and dynamic tests should correlate.

$$\frac{\sigma_0'}{\sigma_0} = 1 + \left(\frac{\dot{\varepsilon}}{D}\right)^{1/q} \tag{6.2}$$

The first case considered for dynamic uniaxial tests having small strains in the neighborhood of the yield strain with constitutive constants of $D = 40.4s^{-1}$ and $q = 5$ [1]. The next case utilised constants obtained from Abramowicz [38] with constitutive constants of $D = 802s^{-1}$ and $q = 3.585$. These constants were determined from more recent dynamic uniaxial tensile experiments performed at the Department of Mechanical Engineering at the University of Liverpool. The last case utilised calculated values from the test data,

with the constitutive constants being determined to be $D = 844s^{-1}$ and $q = 2.207$.

From *Figure 6-14* it can be seen that the first set of Cowper-Symonds curves are far from the test data indicating that the constitutive constants do not correlate well for the mild steel test. The second and third set of data lie on top of one another as the constitutive constants are very similar. For the second and third sets the upper yield point of the scaled quasi-static tensile test lies between the scaled dynamic compression tests, but then deviates as it moves away from the yield point. The lower yield points of the quasi-static and dynamic scaled test results do onto correlate exactly but are not far off. The deviation is not substantial and lies within an acceptable range. In order to adjust the lower yield points to coincide the values of $D = 2000s^{-1}$ and $q = 5$ had to be used.

There is a large scatter of test data was that has been published. Some of this test data was gathered by Jones [1] and compared to the Cowper-Symonds constitutive model with constants of $D = 40.4s^{-1}$ and $q = 5$. A copy of Jones's graph is shown in *Figure 6-15*. Added to Jones's graph is the data point of the mild steel tested at a strain rate of $918s^{-1}$. It can be seen that there is considerable scatter between the results of the different authors and that the added data point falls within the scatter. Jones related this scatter to the range of different mild steels tested, the difference in grain size, the heat treatment, and the variety of testing machines and data recording equipment used.

The mild steel test data was then compared to experimental data generated by Tanimura [56]. The data that Tanimura presented was for an annealed mild steel test at strain rates of $0.001s^{-1}$ and $2000s^{-1}$ and a copy of the stress-strain curve is shown in *Figure 6-16*. Selected points from the Tanimura curve were then plotted over the mild steel test data and is shown in *Figure 6-17*. From *Figure 6-17* it can be seen that there is very good correlation between the quasi-static and dynamic test data. The strain rate of the Tanimura curve is higher than that of the test data and this is reflected in the upper yield point being higher than that of the curve at a strain rate of $918s^{-1}$. The curve after the lower yield point correlated well except for the slight oscillation of the curve of Tanimura. These oscillations could be the result of no dispersion correction being applied to the captured data from the pressure bars. If the dynamic curve of *Figure 6-16* is compared to the uncorrected curve

of *Figure 6-5 c)* it is evident that the two curves follow the same trend indicating that no dispersion correction was applied.

6.4.5 Comparison of Test Data with that of Published Results and the Cowper-Symonds Model for Aluminum

The aluminum dynamic compression tests were compared to the quasi-static tensile test. From *Figure 6-18* it can be seen that the yield point of the quasi-static tensile test and dynamic compression test are very close, with the dynamic compression test being higher. This indicates that strain rate sensitivity is low for aluminum as shown by Lipshitz [36] and Jones [1]. The quasi-static tensile test then deviated from the dynamic compression test as the tensile test gives the engineering stress and the compression test give the true stress. The dynamic compression test data was then compared to data obtained from Namat-Nasser [57] and is shown on *Figure 6-18*. Data for strains lower than 0.03 could not be obtained for Namat-Nasser graph as there were large oscillations on the stress-strain curve indicating that dispersion correction was not implemented. Also plotted was data published by Jones[1]. The curve of Jones and Namat-Nasser have higher stress levels than that of dynamic compression tests. The test data curves deviate by an average value of $50MPa$ from that of the data of Jones and Namat-Nasser, but this could be due to the different state of work hardening the specimens were subjected to.

The aluminum dynamic compression tests was also compared to results obtained for the Cowper-Symonds constitutive model. The constitutive constants used in *Equation 6.2* were $D = 1238000s^{-1}$ and $q = 4$ as taken from Jones [1]. Again as in the mild steel test the dynamic compression test with strain rates of $224s^{-1}$ and $1176s^{-1}$ and the quasi-static tensile test (strain rate $= 0.001s^{-1}$) were scaled using constitutive constants for *Equation 6.2* to a strain rate of $1 \times 10^{-4}s^{-1}$ and then plotted. From *Figure 6-18* it can be seen that the yield point of the quasi-static test is higher than that of the two dynamic tests indicating the the constitutive constants are not correct. Jones did note that the two constitutive constants were obtained from an average of widely scattered experimental data.

6.5 Summary

In this chapter the operation of the gas gun system was discussed and the short comings of using the existing barrel were listed. The strain gauge bridge amplifiers and data acquisition system were discussed. The data processing program was evaluated. This included comparing results that were and were not corrected for dispersion, and merits for using higher modes for dispersion correction. It was found that the oscillations of the stress-strain curve were considerably reduced when dispersion was corrected for, and the first mode was dominant. The effect on sample frequency of the dispersion correction were discussed and sample frequency of 10MHz was chosen. Finally, the results of the tests carried out were compared with the constitutive models and published results. From this it was seen that there was good correlation between published data and the test data, but the model correlation was not as good. The selection of the constants used in the models was critical. In addition to this thestate of work hardening on the specimen alters the flow stress considerably.

Conclusions and recommendations for future work are given in the next chapter.

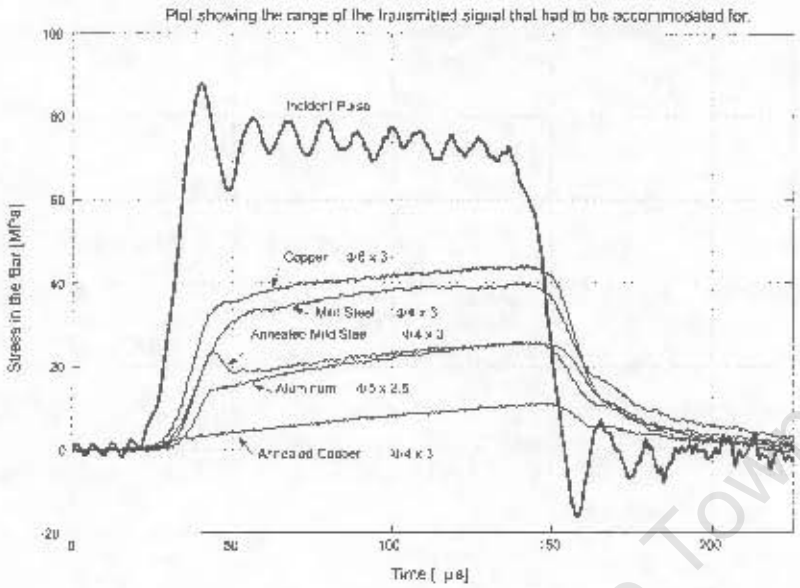

FIGURE 6-1. Plot showing the range of for which the transmitted signal had to be accommodated

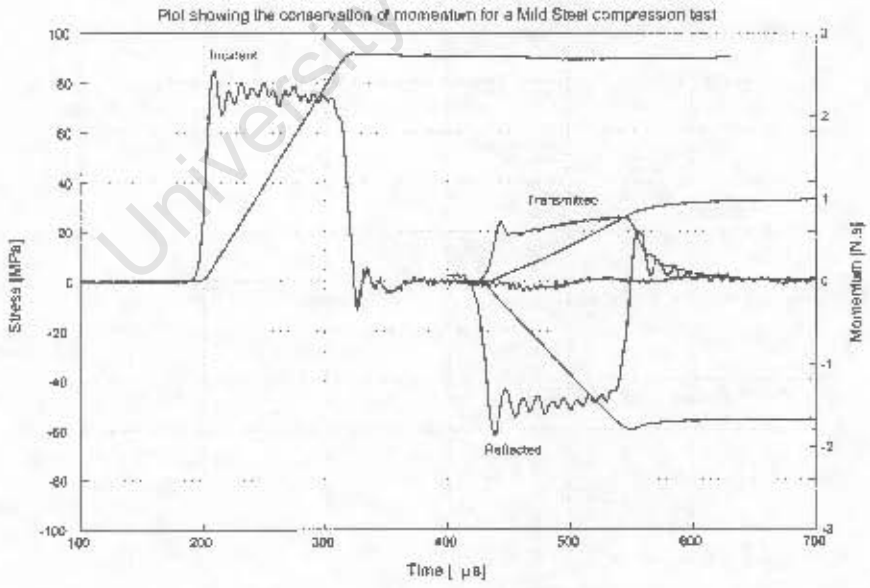

FIGURE 6-2. Plot showing the conservation of momentum for a mild steel compression test.

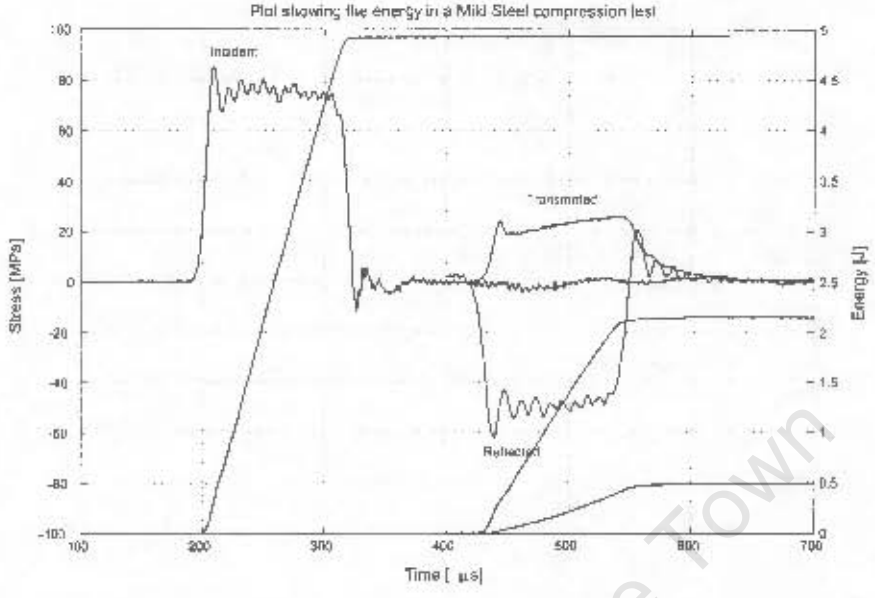

FIGURE 6-3. Plot showing the energy in a mild steel compression test

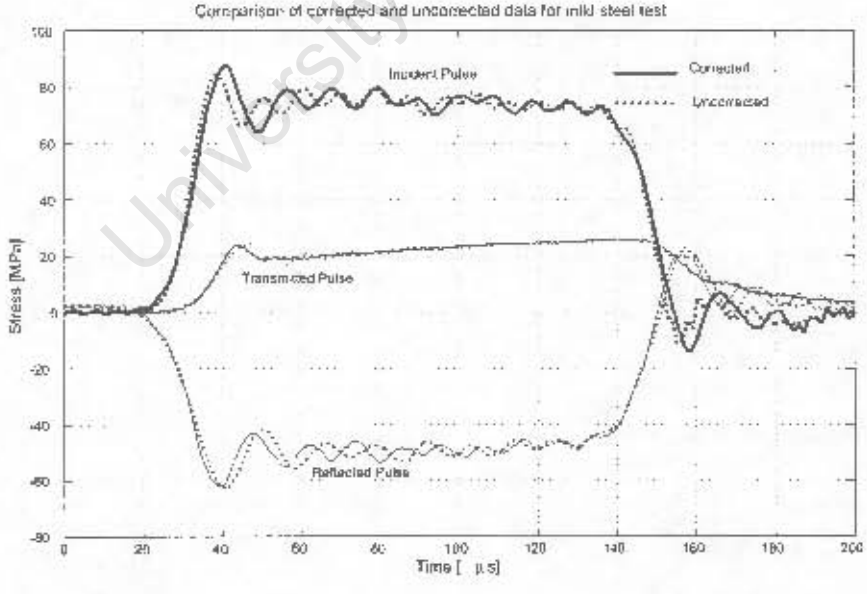

FIGURE 6-4. Comparison of corrected and uncorrected data for a mild steel test

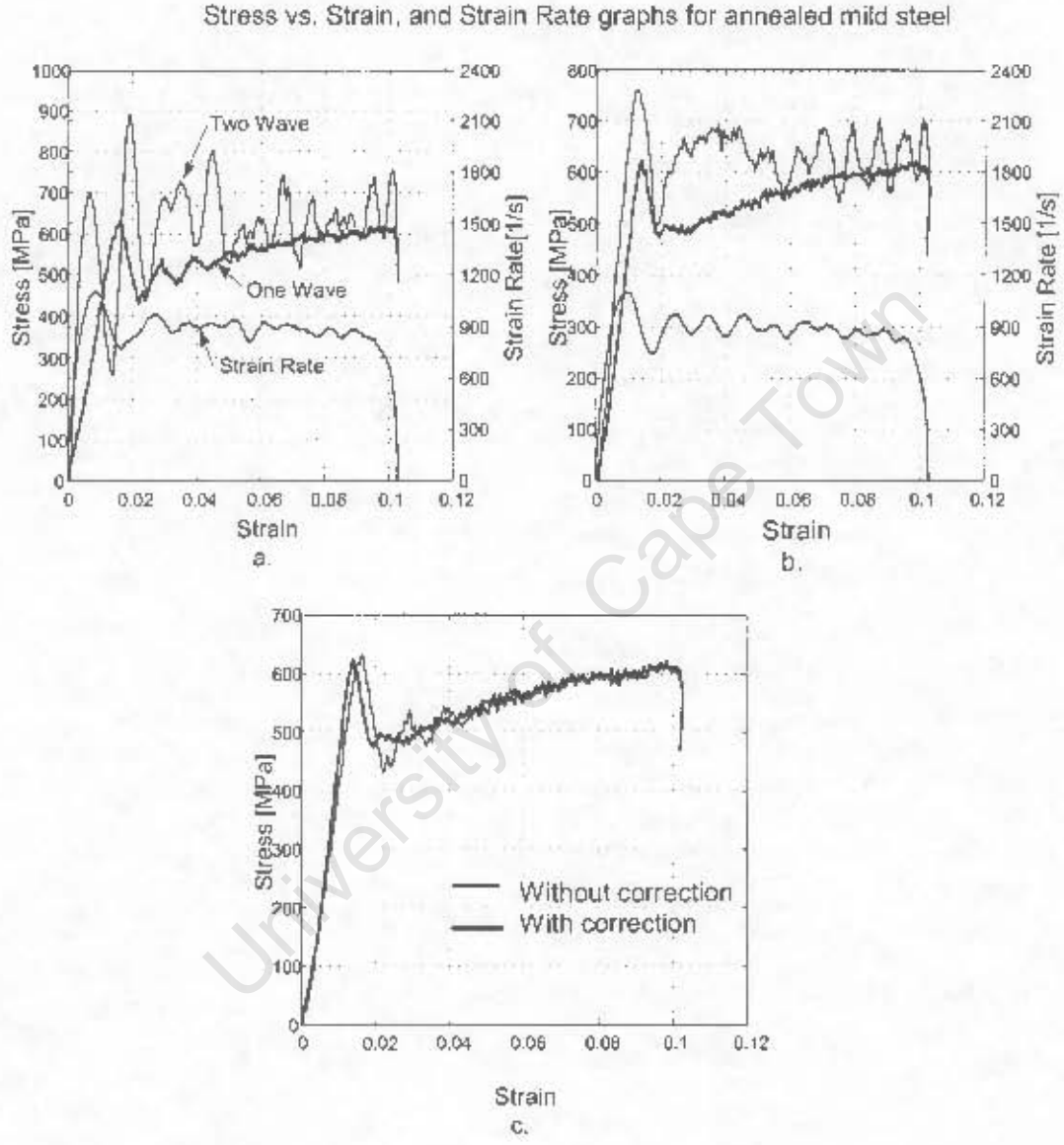

FIGURE 6-5. Stress vs. Strain, and Strain Rate graphs for annealed mild steel. a) without dispersion correction. b) with dispersion correction. c) comparison of the one wave stress-strain curves with and without correction

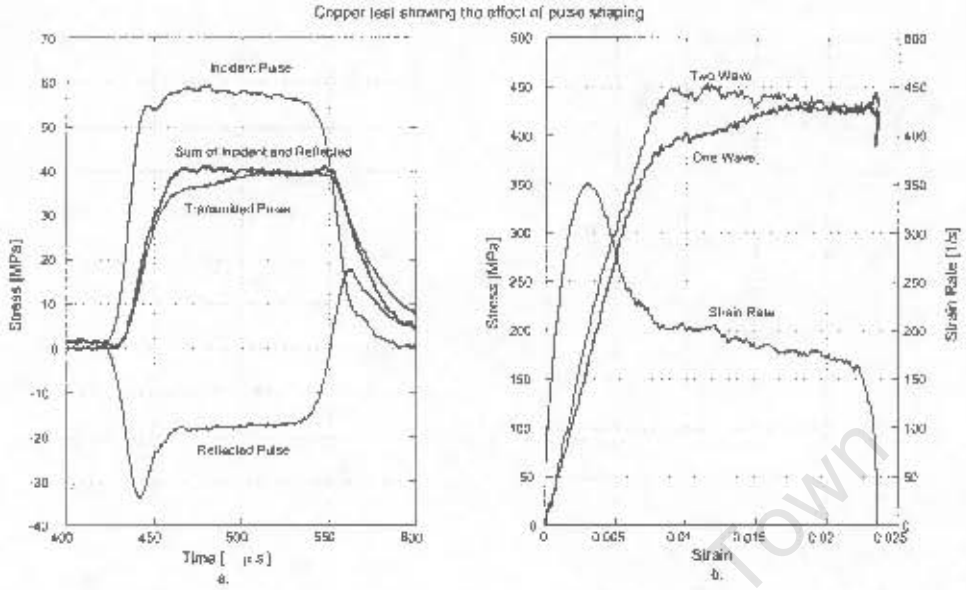

FIGURE 6-6. Copper test showing the effect of pulse shaping. a.) the stress reading in the bar and b.) the Stress-strain and strain rate plot.

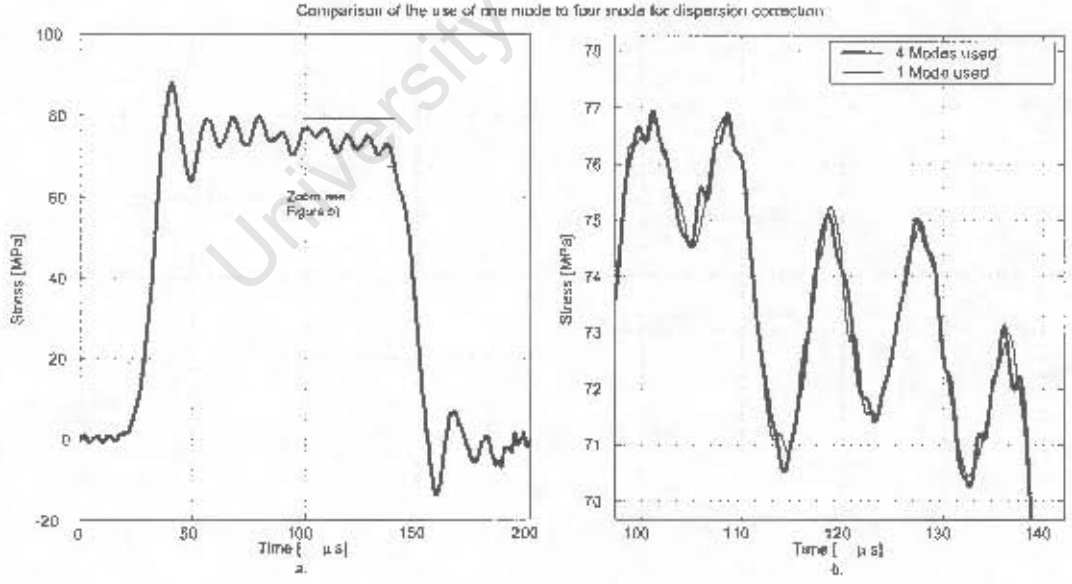

FIGURE 6-7. Comparison of the use of one mode to four mode for dispersion correction. a) plot of the waves, b) zoomed in section of waves.

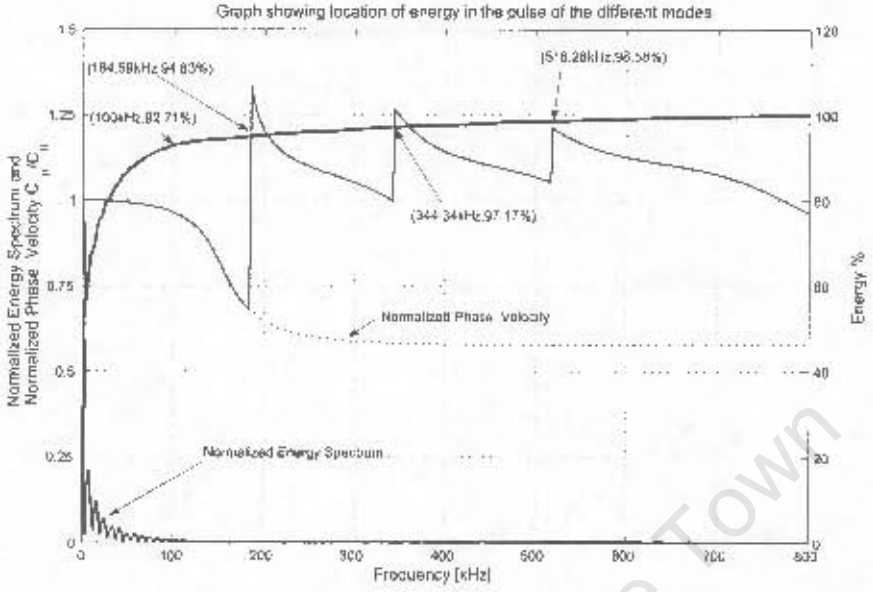

FIGURE 6-8. Graph showing location of energy in the pulse of the different modes

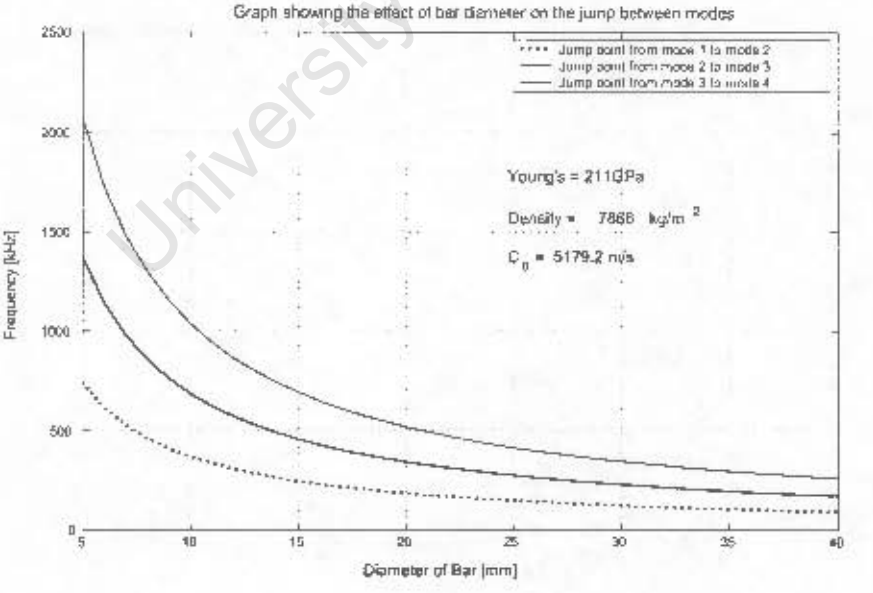

FIGURE 6-9. Graph showing the effect of bar diameter on the jump between modes

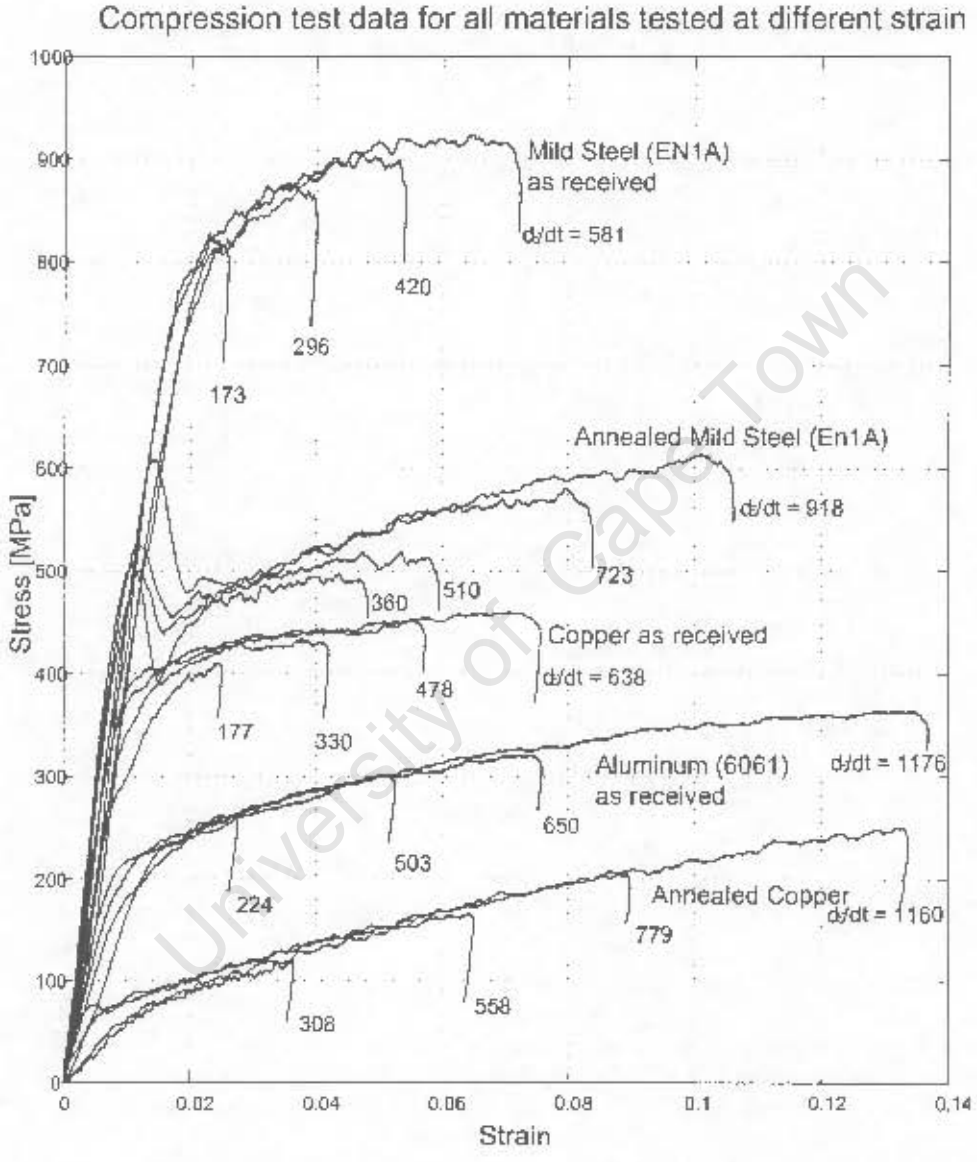

FIGURE 6-10. Compression test data for all the materials tested at different strain rates

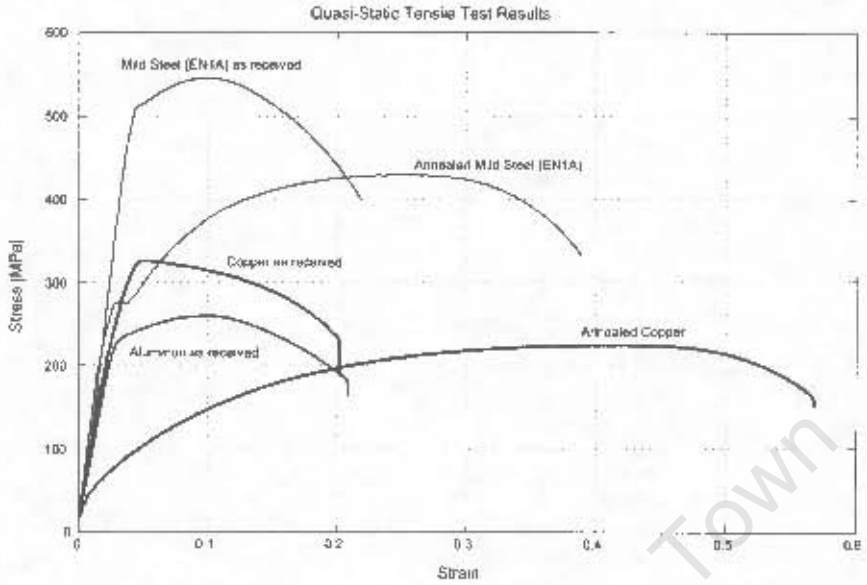

FIGURE 6-11. Quasi-static tensile test results showing typical behavior for all three materials tested

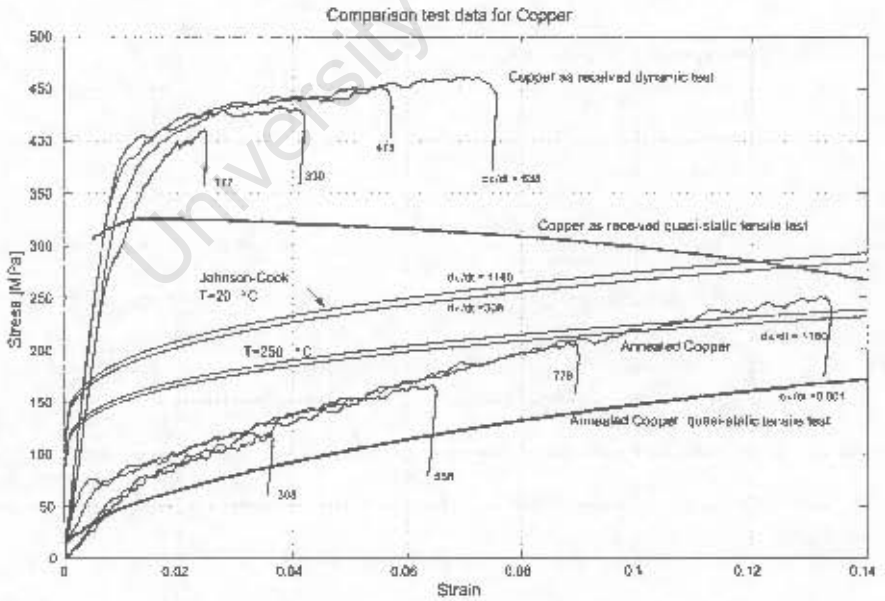

FIGURE 6-12. Comparison test data for Copper

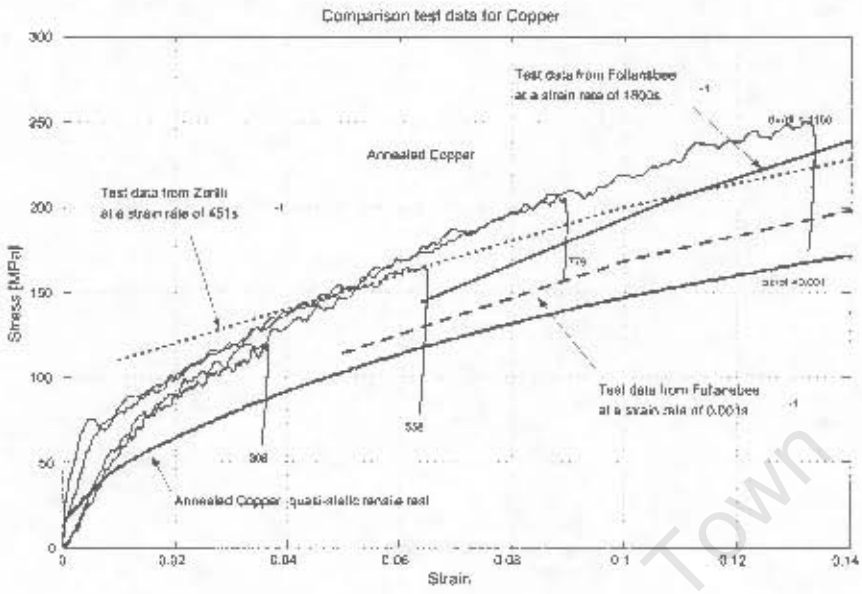

FIGURE 6-13. Comparison of annealed copper test data with published results

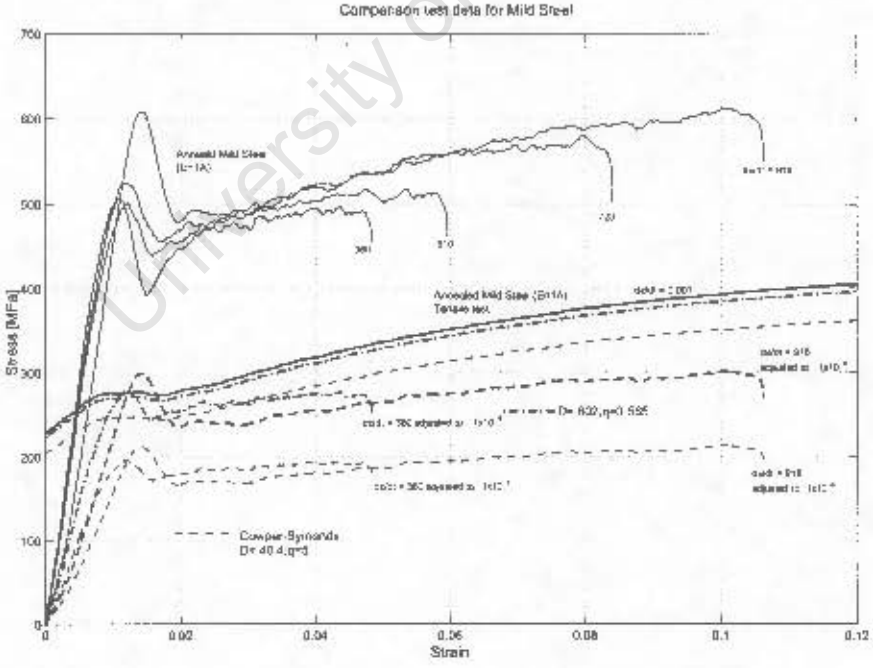

FIGURE 6-14. Comparison test data to the Cowper-Symonds constitutive model for mild steel

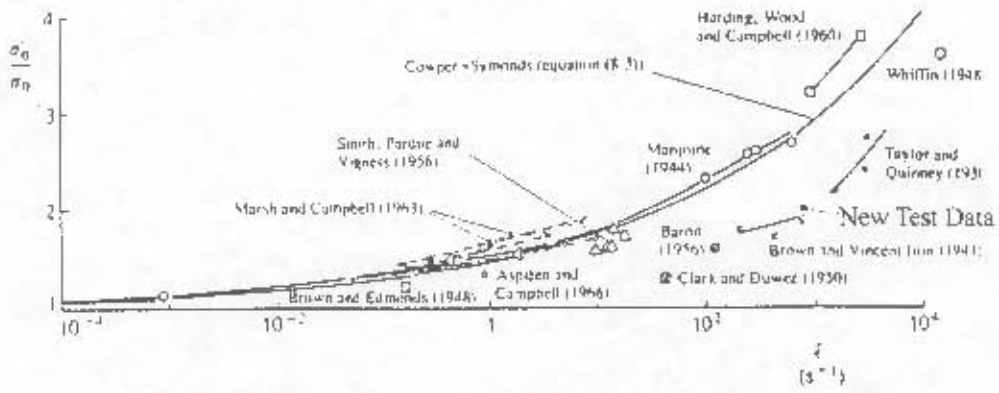

Figure 8.8 Variation of dynamic uniaxial lower yield stress of mild steel with strain-rate.[8.17] All test results were obtained in dynamic tension except the dynamic compression tests of Marsh and Campbell (1963), Aspden and Campbell (1966) and Whiffin (1948). Equation (8.3) is the Cowper-Symonds empirical relation which is introduced in § 8.3.2 ($D = 40.4\ s^{-1}$ and $q = 5$).

FIGURE 6-15. Graph showing the skater of test data used to generate the Cowper-Symonds coefficients for mild steel

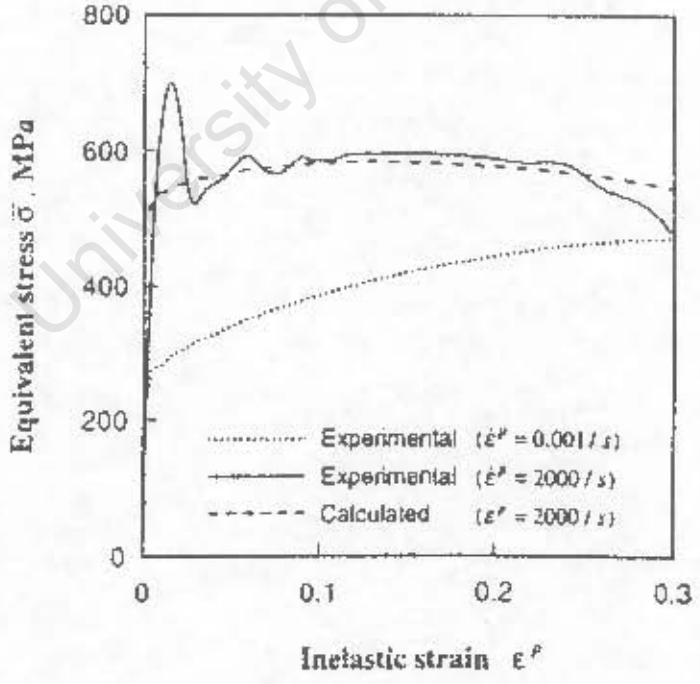

FIGURE 6-16. Copy of stress-strain curve from mild steel generated by Tanimura

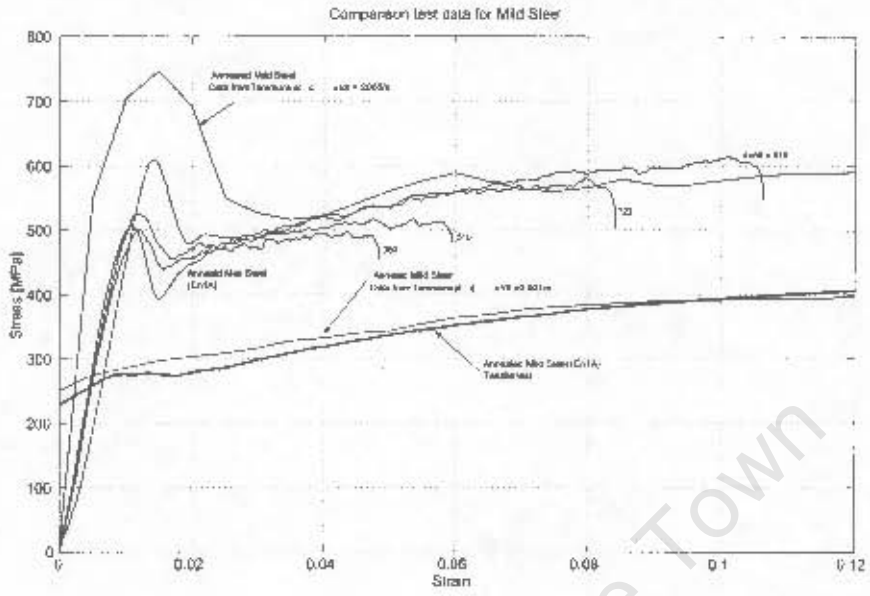

FIGURE 6-17. Comparison test data to the data obtaind from Tanimura for mild steel

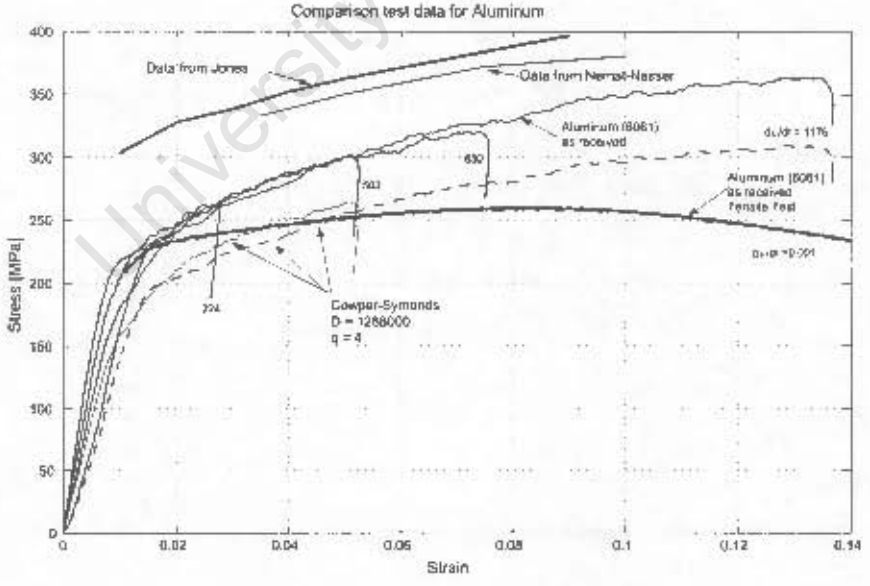

FIGURE 6-18. Comparison test data for aluminum

7

Concluding Remarks and Recommendations

7.1 Concluding Remarks

The system as a whole functioned well and enabled testing of different materials at various strain rates. Each component of the system was calibrated separately before the SHPB system was calibrated as a unit. The calibration tests conducted were repeatable and the dynamic calibration factor only deviated from the theoretical calibration factor by 5%, thus reconfirming the calibration of the system. The method for determining Young's modulus and Poisson's ratio of the bar was very successful, as the Young's modulus could be determined to within $1GPa$ and the Poisson's ratio to within 0.01. The dispersion correction program used was able to shift the pulses to the specimen interface and substantially reduce the oscillations on the stress strain plot. In addition to this, the use of pulse shaping further reduced the oscillations. The inclusion of the higher modes only improved the shape of the pulse marginally.

The *Visual Basic* user interface for the data acquisition facility was user friendly and the operation was very similar to that of an oscilloscope. The control valving for the gas gun and the gas gun itself was simple to use. The use of *Excel* as a frontend to *Maltab* worked well as the operator of the system was not required to know how to use *Matlab* to use the dispersion correction software. As a result, the time required to train an operator was considerably reduced. The zeroing of the strain gauge bridge was not user friendly as it had to be done by trimming a potentiometer by inserting a small screwdriver into a hole in the side of the amplifier.

The data acquisition system was more than adequate to capture the signal from the strain gauge amplifiers. The amplifiers gave sufficient gain to the signal to generate a stress-strain plot, but the gain was not sufficiently flexible to utilise the full resolution of

the data acquisition system. As the amplifier gain drop-off and phase shift was determined by using an 8-bit resolution digital oscilloscope the accuracy of the mapping function was limited. This could be improved by using the ADLINK card to map the gain drop-off and phase shift for each amplifier. Amplifier specific correction functions could then be generated thus improving the correction of the signal.

The barrel used for the gas gun was not ideal as the gas vents were too short. As a result of this, the dynamic calibration of the system could not be performed with a long striker. This resulted in an inaccuracy in one of the calibration methods. In addition to this the barrel bore was smaller than that of the bar. This resulted in the striker going plastic at high exit velocities. Consequently, the striker velocity was limited for the calibration method used.

As the bars were aligned by eye there was no method of determining the accuracy of the alignment. Consequently error could result from misalignment of the two bars.

The material tests conducted showed that the system could reliably produce stress-strain curves at different strain rates. The material models did not correlate well with the test data but there was good correlation with published data. There could be two main reasons for this. Firstly the material tests conducted showed that there is a large difference in the stress level of an as received specimen compared to one that was annealed. Thus, the microstructure and work hardening state of the specimen could well be the source of the discrepancy. Secondly the value used for the constitutive constants in the model significantly altered the predicted stress level. As a result the selection of the correct values is vital. With the SHPB system and data acquisition facility developed in this thesis, which is highly accurate and leads to consistent and repeatable results, this is now possible. Generation of such constitutive constants as function of the work hardening and microstructure is beyond the scope of the thesis.

7.2 Recommendations for Future Work

Although the SHPB system setup is functioning sufficiently well to test materials, the following modifications are recommended to improve the system:

1. The gain of the amplifiers should be made adjustable to exploit more fully the resolution of the data acquisition card. This could be achieved by either having a jumper of the second stage of the amplifier to allow for the gain to be set at $10V/V$ or $100V/V$, or installing a third stage in the amplifier with a programmable gain.

2. The variable resistor used to zero the strain gauge bridge could be mounted externally so as to make adjustment simpler.

3. After modifying the amplifiers, each amplifier is to be mapped using the ADLINK card.

4. A 20mm barrel should be sourced so that the striker and bar are the same diameter. The barrel must have sufficiently long gas vents to allow for the use of a long striker in the calibration tests.

5. The valving should be modified to improve the repeatability of the striker velocity at the low speeds.

6. An alignment system should be designed and installed to insure the accurate alignment of the bars.

As only limited testing was conducted, additional material testing and investigation should be performed to determine the cause of the deviation between the test data and the constitutive model. In addition to the items mentioned in *Section 7.1*, the effects of work hardening and temperature need to be considered in developing the stress-strain behavior of the material at high strain rates. From these tests the constitutive models could be modified to be more representative of the material. During testing the incident pulse should be pulse shaped, as there is a considerable reduction in the oscillations on the stress-strain curve in so doing.

References

[1] Jones Norman, *Structural Impact*, Cambridge University Press, 1989.

[2] Johnson R. G and W. H. Cook, "A constitutive model and data for metals subjected to large strains, high strain rates and high temperatures.," *Int. Symp. Ballistics, the Hague Netherlands*, vol. 7, pp. 541–547, 1983.

[3] P.H.Pope Gorham D.A. and J.E.Field, "An improved method for compressive stress-strain measurements at very high strain rates," *Proc. R. Soc. Lond.*, vol. A, no. 438, pp. 153–170, 1992.

[4] Lindholm U.S. and L.M. Yeakley, "High strain-rate testing: Tension and compression," *Exp. Mech.*, vol. 8, pp. 1 9, 1968.

[5] Davies E. D. H. and S. C. Hunter, "The dynamic compression testing of solids by the method of the split hopkinson pressure bar," *J. Mech. Phys. Solids*, vol. 11, pp. 155-179, 1963.

[6] Lindholm U.S., "Some experiments with the split hopkinson pressure bar," *J. Mech. Phys. Solids*, vol. 12, pp. 317–355, 1964.

[7] Gray G.T., *Classic Split Hopkinson Pressure Bar Technique*, to be published in ASM Volume 8 - Mechanical Testing, 1999

[8] Nicholas T., "Tensile testing of materials at high rates of strain," *Exp. Mech.*, vol. 21, no. 5, pp. 177 185, 1981.

[9] L. J. Griffiths Ellwood S. and D.J.Parry, "A tensile technique for material testing at high strain rates," *J. Phy. E. Sci. Instrum*, vol. 15, pp. 1169–1172, 1982.

[10] A.M. Rajenbran E. A. Strader Cross L. A., S. J. Bless and D. S. Dawicke, "New techniques to investigate necking in a tensile hopkinson bar," *Exp. Mech*, vol. 24, no. 3, pp. 184–194, 1984.

[11] Wang M. and M. Ham, "A kolsky bar tension, tension-tension," *Exp. Mech*, vol. 33, no. 1, pp. 7 – 14, March 1993.

[12] S.R. Reid Al-Mousawi M.M and W.F. Deans, "The use of the split hopkinson pressure bar techniques in high strain rate materials testing.," *J.Mech.Eng.Sci.*, vol. 221, no. C, pp. 273–292, 1997.

[13] J. D. Campbell Duffy J. and R. H. Hawley, "On the use of a torsional split hopkinson bar to study rate effects in 1100-0 aluminum," *J. Appl. Mech.*, vol. 38, pp. 83–91, 1971.

[14] Lambert E. D. and C. Allen Ross, "Strain rate effects on dynamic fracture and strength," *Int. J. of Impact Eng.*, vol. 24, pp. 985 998, 2000.

[15] Maigre H. and D. Rittel, "Dynamic fracture detection using the force-displacement reciprocity: Application to the compact compression nspecimen," *Int. J. of Fracture*, vol. 73, pp. 67–79, 1995.

[16] Rittel D. and H. Maigre, "An investigation of dynamic crack initiation in PMMA," *Mech. of Mall.*, vol. 23, pp. 229 239, 1996.

[17] E. Strader Rosenberg Z., D. Dawicke and S. J. Bless, "A new technique for heating specimens in the split hopkinson bar experiments using induction coil heaters," *Exp. Mech*, vol. 26, no. 3, pp. 275–278, 1986.

[18] Gilat A. and X. Wu, "Elevated temperature testing with the torsional split hopkinson bar," *Exp. Mech*, vol. 34, no. 2, pp. 166–170, 1994.

[19] D. Macdougall Trojanowski A. and J. Harding, "An improved technique for the experimental measurement of the specimen surface temperature during hopkinson bar tests," *Meas. Sci. Technol*, vol. 9, pp. 12 19, 1998.

[20] Hopkinson B.F.R.S, "A method of measuring the pressure produced in the detonation of explosives by the impact of bullets," *Phil. Trans. Roy. Soc. Lond.*, vol. 213, pp. 437 456, 1914.

[21] Davies R.M., "A critical study of the hopkinson pressure bar," *Phil. Trans. R. Soc. Lond.*, vol. 240, pp. 375–457, 1948.

[22] Kolsky H., "An investigation of the mechanical properties of materials at very high rates of load," *Proc. R. Soc. Lond.*, vol. B62, pp. 676–700, 1949.

[23] Achunbach J. D., *Wave Propagation in Elastic Solids*, vol. 16, North-Holland Publishing Company, 1973.

[24] A.B.Coppens Kinsler L.E., A.R. Frey and J.V.Sanders, *Fundamentals of Acoustics*, John Wiley and Sons, 1982.

[25] Spotts M. F., *Mechanical Design Analysis*, Prentice-Hall, Inc., 1964.

[26] Follansbee P.S. and C. Frantz, "Wave propagation in the split Hopkinson pressure bar," *J. Eng. Mat and Tech.* vol. 105, pp. 61–66, 1983.

[27] Love A.E.H., *A Treatise on the Mathematical Theory of Elasticity*, Dover. 1944

[28] Hsieh D.Y. and H. Kolsky, "An experimental study of pulse propagation in elastic cylinders," *Proc. Phys. Soc.*, vol. 71, 1958.

[29] Morrison N., *Introduction to Fourier Analysis*, Wiley Interscience, 1994.

[30] Yew E.H. and C.S. Chen, "Experimental study of dispersive waves in beam and rod using FFT," *J.Appl.Mech.*, vol. 45, pp. 940–942, 1978.

[31] Gorham D.A., "A numerical method for the correction of dispersion in pressure bar signals," *J. Phys. E: Sci. Instrum.*, vol. 16, pp. 477–479, 1983.

[32] Lee C.K.B and R.C. Crawford, "A new method for analysing dispersed bar gauge data.," *Meas. Sci. Technol.*, vol. 4, pp. 931–937, 1993.

[33] Lee C.K.B and R.C. Crawford, "Evidence of higher pochhammer-chree modes in an unsplit hopkinson bar," *Meas. Sci. Technol.*, vol. 6, pp. 853–859, 1995.

[34] Marsh K.J. and J.D. Campbell, "The effects of strain rate on the post-yield flow of mild steel," *J. Mech. and Phy. of Solids*, vol. 11, pp. 49–63, 1963.

[35] Hauser F.E., "Techniques for measuring stress-strain response at high strain rates," *Experimental Mechanics*, vol. 6, pp. 395–402, 1966.

[36] J.M.Lipshitz and H.Leber, "Data processing in the split hopkinson pressure bar test," *Int.J.Impact*, vol. 15, no. 6, pp. 723 733, 1994.

[37] Hibbitt, Karlsson and Sorensen Inc., *ABAQUS Theory Manual Version 5.8*, 1998.

[38] Abramowicz W and N. Jones, "Dynamic progressive buckling of circular and square tubes." *Int. J. Impact Engng*, vol. 4, no. 4, pp. 243–270, 1986.

[39] P.W. Bridgman, *Studies in Large Plastic Flow and Fracture*, McGraw - Hill, 1952.

[40] U.S. Lindholm Johnson G. R., J.M. Hoegfeldt and A. Nagy, "Response of various metals to large torsional strains over a large range of strain rates - part 1: Ductile materials," *ASME J. Eng Mat. and Tech.*, vol. 105, no. 1, pp. 42 – 47, January 1983.

[41] U.S. Lindholm Johnson G. R., J.M. Hoegfeldt and A. Nagy, "Response of various metals to large torsional strains over a large range of strain rates - part 2: Less ductile materials," *ASME J. Eng Mat. and Tech.*, vol. 105, no. 1, pp. 48 – 53, January 1983.

[42] ADLINK Technology Ink., *Users' Guide*, 2.23 edition, December 16 1999.

[43] ADLINK Technology Ink., *Function Reference Manual*, 3.01 edition, June 4 2000.

[44] Hannah R.L. and R.T. Reese, "Strain gauge adhesives - operating characteristics," *Experimental Techniques*, pp. 19–21, 1994.

[45] British Standards Institution, *BS-18, Part 2 Methods for Tensile Testing of Mtetals.*, 1971.

[46] Bancroft D., "The velocity of longitudinal waves in cylindrical bars," *Physical Review*, 1941.

[47] The MathWorks, Inc, *Signal Processing Toolbox User's Guide. Matlab*, 1998, Version 4.

[48] Burr-Brown Corporation, U.S.A, *Fast-Settling FET-Input Instrumentation Amplifier*, 1993.

[49] Beckwith G. T. and R. D. Marangoni, *Mechanical Measurements*, Addison-Wesley Publishing Company, 4 edition, 1990.

[50] Holman J.P., *Experimental Methods for Engineers*, McGraw-Hill, Inc., 6 edition, 1994.

[51] Wu X.J. and D.A. Gorham, "Stress equilibrium in the split Hopkinson pressure bar test," *J. Phys IV France*, vol. 7, pp. 91–96, 1997.

[52] Ueda K. and A. Umeda, "Dynamic response of strain gauges up to 300kHz.," *Experimental Mechanics*, vol. 38, no. 2, pp. 93–98, June 1998.

[53] Berthholf L.D. and C.H. Karnes, "Two-dimensional analysis of the split Hopkinson pressure bar system," *J. Mech. Phys. Solids*, vol. 23, pp. 1–9, 1975.

[54] Zerilli F. J. and R. Armstrong, "Dislocation-mechanics-based constitutive relations for material dynamics calculations," *J. Appl. Phys.*, vol. 61, no. 5, pp. 1816–1825, March 1987.

[55] Follansbee P. S. and U. F. Kocks, "A constitutive description of the deformation of copper based on the use of the mechanical threshold stress as an internal state variable," *Acta metall.*, vol. 36, no. 1, pp. 81–93, 1988.

[56] K. Mimura Tanimura S. and W. Zhu, "A dynamic constitutive equation and its experimental verification," *J.Phys. IV France*, vol. 10, pp. 33–38, 2000.

[57] J.B. Isaacs Nemat-Nasser S and J.E.Starrett, "Hopkinson techniques for dynamic recovery experiments," *Proc. R. Soc. Lond.*, vol. 435, pp. 371–391, 1991.

Appendix A

Computer Coding

The commented source code for the programs used for the SHPB apparatus are given in this section.

A.1 Source code for dispersion user defined function

The following coding is used to create a user defined function in the *Microsoft Visual Basic* attachment of *Excel*. This user-defined function sends data to *Matlab*, executes the dispersion correction program in *Matlab*, and then retrieves the corrected data. Finally, it inserts the corrected data into the *Excel* worksheet.

Define user function

```
Function Dispersion(dt, read1, dist, E, r, v, D, mode, x3, BSF,
 BSF1, BSF2, BPF, BPF1, BPF2, undisp_reading, corr_v1)
MLEvalString ''clear''                    Clears all the variables in the Matlab workspace
MLEvalString ''cd c:\matlabr11\work''     Sets the path to the program
```

Sends the following data to *Matlab*:

```
MLPutMatrix ''dt'', dt                    Time interval between the samples
MLPutMatrix ''x'', read1                  Data to be corrected for dispersion
MLPutMatrix ''z1'', dist                  Distance to disperse reading
MLPutMatrix ''E'', E                      Young's modulus
MLPutMatrix ''r'', r                      Density of the Bar
MLPutMatrix ''v1'', v                     Poisson's ratio
MLPutMatrix ''do'', D                     Bar diameter
MLPutMatrix ''mode'', mode                Which mode to use for the correction
```

Filtering of the data

```
MLPutMatrix ''x3'', x3                    Cut off Frequency
```

'Band Stop filter

```
MLPutMatrix ''bsf'', BSF          if = 1 a band stop filter is applied to the data
MLPutMatrix ''bsf1'', BSF1          Lower frequency for the band stop filter
MLPutMatrix ''bsf2'', BSF2          Upper frequency for the band stop filter
'Band pass filter
MLPutMatrix ''bpf'', BPF          if = 1 a band pass filter is applied to the data
MLPutMatrix ''bpf1'', BPF1          Lower frequency for the band pass filter
MLPutMatrix ''bpf2'', BPF2          Upper frequency for the band pass filter
```

All the necessary data is now available in the *Matlab* work space for the dispersion correction to be implemented

```
MLEvalString ''undisp_pulse8''      Call the dispersion correction program
MLGetMatrix ''xro1'', undisp_reading  Get the zeroed but not corrected data
MLGetMatrix ''x'', corr_v1          Get the corrected data
End Function                    End of the function
```

A.2 Source code for dispersion correction program

The program accepts the data for *Excel* and performs the following functions on it:

1. Zeroes the data.
2. Adjusts the number of the data points so that there is an odd number of points.
3. Corrects of the amplifier amplitude drop-off and phase shift.
4. Applies a band pass filter and band stop filter if needed.
5. Maps the dispersion correction curves for the first four vibration modes.
6. Performs the dispersion correction.
7. Returns the corrected data to *Excel*

The following data is supplied by *Excel*:

`E =` Young's modulus

`r =` Density

`v1 =` Poisson's ratio

`do =` Bar diameter

`x =` Signal Data

`dt =` Time step between samples

`x3 =` Cut off frequency

`z1 =` Distance that signal is to be moved

`bsf =` if = 1 a band stop filter is applied to the data

`bsf1 =` Lower frequency for the band stop filter

`bsf2 =` Upper frequency for the band stop filter

`bpf =` if = 1 a band pass filter is applied to the data

`bpf1 =` Lower frequency for the band pass filter

`bpf2 =` Upper frequency for the band pass filter

Move the reading to the zero level by taking the first 30 points and finding the offset

```
x = x.';
graph_offset1 = mean(x(1:30));
```

```
x = x - graph_offset1;
```

Make N an even number

```
test_x = rem(length(x),2);                %Find remainder
if test_x == 0;      %test for odd or even number of points
    N = length(x);
else
N = length(x) - 1;
end
```

Adjust signal to new length

```
x = x(1:N);
t = 0:dt:(N)*dt;
```

Calculate new period, angular velocity and frequency for new length

```
T = t(N);                 %set the time period of the new length
wo = 2*pi/T;              %calculate the fundamental angular frequency for the FFT di-
```

visions

```
nc = -fix(N/2) : fix(N/2);
wn = nc.*wo;              %setup a vector for the angular frequency
C0 = sqrt(E/r);
ff = wn./(2*pi);      %setup a vector for the frequency for correction of the amps
```

Move into the frequency domain using the Fast Fourier Transform

```
y = fft(x);
ys1 = fftshift(y);              %Center around 0^th term
```

Correct for amp drop-off

Define amplifier characteristics

```
x1 = 100000;
x2 = 1000000;
y1 = 1;
y2 = 1.5;
```

Set upper cutoff point

```
if x3<x1
 x1 = x3;
```

```
end
```

Calculate the slope of the correction line

```
m = (y2 - y1)/(x2 - x1);
c1 = y2 - m*x2;
```

Generate the function that is used to pull-up the amplifier drop-off

```
corr = ones(1,length(wn));
corr1 = corr.*(ff <= x1 & ff >= -x1);
corr2 = corr.*(ff .* m + c1 ).*(ff>x1 & ff<x3);
corr3 = corr.*(ff .* -m + c1 ).*(ff<-x1 & ff>-x3);
corr = corr1 + corr2 + corr3;
```

Multiply the signal by the correction function.

```
ys2 = ys1.*corr;
```

Correct for phase shift

```
slope = 3.7786e-6;          % From trend line of phase shift
```

Generate the function that is used to correct for the amplifier phase shift

```
phase_corr = ones(1,length(wn));
phase_corr1 = phase_corr.*(ff .*slope).*(ff >= 0);
phase_corr2 = phase_corr.*(ff .* slope ).*(ff < 0);
phase_corr = phase_corr1 + phase_corr2 ;
```

Multiply the signal by the correction function.

```
ys = ys2.*exp(phase_corr*i);
```

Band Stop filter

Test if Band Stop filter is to be used

```
if bsf == 1;
```

Generate a 0-1 vector to cut out the required frequencies

```
bandstop = ones(1,length(wn));
bandstop1 = bandstop.*((ff >= -bsf2) & (ff <= -bsf1));
bandstop2 = bandstop.*((ff <= bsf2) & (ff >= bsf1));
bandstop = (bandstop1 + bandstop2);
bandstop = (bandstop ==0);
```

Multiply the data by the 0-1 vector

```
ys =ys .* bandstop ;
end
```

Band Pass Filter

Test if Band Pass Filter is to be used

```
if bpf == 1;
```

Generate a 0-1 vector to pass the required frequencies

```
bandpass = ones(1,length(wn));
bandpass1 = bandpass.*((ff >= -bpf2) & (ff <= -bpf1));
bandpass2 = bandpass.*((ff <= bpf2) & (ff >= bpf1));
bandpass = bandpass1 + bandpass2;
```

Multiply the data by the 0-1 vector

```
ys =ys .* bandpass ;
end
```

Generate the velocity used for dispersion

```
if mode == 1                %use only mode one for dispersion correction
load P_C_mode1.mat          %load the data for the first dispersion curves
d_la = d_la.';
n = 1:length(d_la);
fo = 1/T;
f = fo .*n;
```

Interpolate to extract the curve for the particular Poisson's ratio

```
Cn_Co_at_v_mode1 = interp2(d_la,v,Cn_Co.',d_la,v1,'cubic');
```

Calculate the velocity by (Cn/Co)*Co

```
Cn_P_C_mode1 = Cn_Co_at_v_mode1 .* C0;
la_1 = d_la./do;
```

Calculate the frequency f = Cn/la for the generated curves

```
f_P_C_mode1 = Cn_P_C_mode1.*la_1;
```

Interpolate to obtain Phase velocity for all the frequencies for the input data

```
Cn = interp1(f_P_C_mode1,Cn_P_C_mode1,f,'cubic');

elseif mode == 2            %use only mode one and two for dispersion correction
```

```
load P_C_mode1.mat          %load the data for the first dispersion curves
d_la = d_la.';
n = 1:length(d_la);
fo = 1/T;
f = fo .*n;
load Df_Co_1_2.mat                  % load jump point from mode 1 to mode 2
Interpolate to extract the value for the particular Poison's ratio
Df_Co_jump_1_2 = interp1(v,Df_Co_1_2,v1,'cubic');
Calculate the jump point from mode 1 to mode 2
f_jump_1_2 = Df_Co_jump_1_2.*C0/do;
Interpolate to obtain Phase velocity for all the frequencies for the input data
Cn_Co_at_v_mode1 = interp2(d_la,v,Cn_Co.',d_la,v1,'cubic');
Calculate the velocity by (Cn/Co)*Co
Cn_P_C_mode1 = Cn_Co_at_v_mode1 .* C0;
load P_C_mode2.mat          %load the data for the second dispersion curves
d_la = d_la.';
Interpolate to obtain Phase velocity for all the frequencies for the input data
Cn_Co_at_v_mode2 = interp2(d_la,v,Cn_Co.',d_la,v1,'cubic');
Calculate the velocity by (Cn/Co)*Co
Cn_P_C_mode2 = Cn_Co_at_v_mode2 .* C0;
la_1 = d_la./do;                        %Calculate 1/la
Calculate the frequency f = Cn/la for the first mode
f_P_C_mode1 = Cn_P_C_mode1.*la_1;
Calculate the frequency f = Cn/la for the second mode
f_P_C_mode2 = Cn_P_C_mode2.*la_1;
```

Interpolate to obtain Phase velocity for all the frequencies for the input data with reference to the first mode

```
Cn_mode1 = interp1(f_P_C_mode1,Cn_P_C_mode1,f,'cubic');
Cn_mode2 = interp1(f_P_C_mode2,Cn_P_C_mode2,f,'cubic');
```

Cut off the higher Phase velocity for the first mode and the lower Phase velocity for the second mode

```
Cn = Cn_mode1.*(f < f_jump_1_2) + Cn_mode2.*(f >= f_jump_1_2);


elseif mode == 3          %use the first three modes for dispersion correction
load P_C_mode1.mat        %load the data for the first dispersion curves
d_la = d_la.';
n = 1:length(d_la);
fo = 1/T;
f = fo .*n;
load Df_Co_1_2.mat        % load jump point from mode 1 to mode 2
Interpolate to extract the value for the particular Poisson's ratio
Df_Co_jump_1_2 = interp1(v,Df_Co_1_2,v1,'cubic');
Calculate the jump point from mode 1 to mode 2
f_jump_1_2 = Df_Co_jump_1_2.*C0/do;
Interpolate to obtain Phase velocity for all the frequencies for the input data
Cn_Co_at_v_mode1 = interp2(d_la,v,Cn_Co.',d_la,v1,'cubic');
Calculate the velocity by (Cn/Co)*Co
Cn_P_C_mode1 = Cn_Co_at_v_mode1 .* C0;
load P_C_mode2.mat %load the data for the second dispersion curves
d_la = d_la.';
Interpolate to obtain Phase velocity for all the frequencies for the input data
Cn_Co_at_v_mode2 = interp2(d_la,v,Cn_Co.',d_la,v1,'cubic');
Calculate the velocity by (Cn/Co)*Co
Cn_P_C_mode2 = Cn_Co_at_v_mode2 .* C0;
load P_C_mode3.mat        %load the data for the third dispersion curves
d_la = d_la.';
load Df_Co_2_3.mat                %jump point from mode 2 to mode 3
Interpolate to extract the value for the particular Poisson's ratio
Df_Co_jump_2_3 = interp1(v,Df_Co_2_3,v1,'cubic');
Calculate the jump point from mode 2 to mode 3
f_jump_2_3 = Df_Co_jump_2_3.*C0/do;
Interpolate to obtain Phase velocity for all the frequencies for the input data
```

```
Cn_Co_at_v_mode3 = interp2(d_la,v,Cn_Co.',d_la,v1,'cubic');
```

Calculate the velocity by (Cn/Co)*Co

```
Cn_P_C_mode3 = Cn_Co_at_v_mode3 .* C0;
la_1 = d_la./do;                          %Calculate 1/la
```

Calculate the frequency (f = Cn/la) for the first three modes

```
f_P_C_mode1 = Cn_P_C_mode1.*la_1;
f_P_C_mode2 = Cn_P_C_mode2.*la_1;
f_P_C_mode3 = Cn_P_C_mode3.*la_1;
```

Interpolate to obtain Phase velocity for all the frequencies for the input data with reference to the first mode

```
Cn_mode1 = interp1(f_P_C_mode1,Cn_P_C_mode1,f,'cubic');
Cn_mode2 = interp1(f_P_C_mode2,Cn_P_C_mode2,f,'cubic');
Cn_mode3 = interp1(f_P_C_mode3,Cn_P_C_mode3,f,'cubic');
```

Generate the Phase Velocity curve using the first three modes.

```
Cn = Cn_mode1.*(f < f_jump_1_2) + Cn_mode2.*((f >= f_jump_1_2)&
(f < f_jump_2_3)) + Cn_mode3.*(f >= f_jump_2_3);


elseif mode ==4          %use the first four modes for dispersion correction
load P_C_mode1.mat'      %load the data for the first dispersion curves
d_la = d_la.';
n = 1:length(d_la);
fo = 1/T;
f = fo .*n;
load Df_Co_1_2.mat           %jump point from mode 1 to mode 2
```

Interpolate to extract the value for the particular Poisson's ratio

```
Df_Co_jump_1_2 = interp1(v,Df_Co_1_2,v1,'cubic');
```

Calculate the jump point from mode 1 to mode 2

```
f_jump_1_2 = Df_Co_jump_1_2.*C0/do;
```

Interpolate to obtain Phase velocity for all the frequencies for the input data

```
Cn_Co_at_v_mode1 = interp2(d_la,v,Cn_Co.',d_la,v1,'cubic');
```

Calculate the velocity by (Cn/Co)*Co

```
Cn_P_C_mode1 = Cn_Co_at_v_mode1 .* C0;
load P_C_mode2.mat      %load the data for the second dispersion curves
d_la = d_la.';
```

Interpolate to obtain Phase velocity for all the frequencies for the input data

```
Cn_Co_at_v_mode2 = interp2(d_la,v,Cn_Co.',d_la,v1,'cubic');
```

Calculate the velocity by (Cn/Co)*Co

```
Cn_P_C_mode2 = Cn_Co_at_v_mode2 .* C0;
load P_C_mode3.mat          %load the data for the third dispersion curves
d_la = d_la.';
load Df_Co_2_3.mat              %jump point from mode 2 to mode 3
```

Interpolate to extract the value for the particular Poisson's ratio

```
Df_Co_jump_2_3 = interp1(v,Df_Co_2_3,v1,'cubic');
```

Calculate the jump point from mode 2 to mode 3

```
f_jump_2_3 = Df_Co_jump_2_3.*C0/do;
```

Interpolate to obtain Phase velocity for all the frequencies for the input data

```
Cn_Co_at_v_mode3 = interp2(d_la,v,Cn_Co.',d_la,v1,'cubic');
```

Calculate the velocity by (Cn/Co)*Co

```
Cn_P_C_mode3 = Cn_Co_at_v_mode3 .* C0;
load P_C_mode4.mat              %load the data for the fourth dispersion curves
d_la = d_la.';
load Df_Co_3_4.mat              %jump point from mode3 to mode4
```

Interpolate to extract the value for the particular Poison's ratio

```
Df_Co_jump_3_4 = interp1(v,Df_Co_3_4,v1,'cubic');
```

Calculate the jump point from mode 3 to mode 4

```
f_jump_3_4 = Df_Co_jump_3_4.*C0/do;
```

Interpolate to obtain Phase velocity for all the frequencies for the input data

```
Cn_Co_at_v_mode4 = interp2(d_la,v,Cn_Co.',d_la,v1,'cubic');
```

Calculate the velocity by (Cn/Co)*Co

```
Cn_P_C_mode4 = Cn_Co_at_v_mode4 .* C0;
la_1 = d_la./do;                        %Calculate 1/la
```

Calculate the frequency (f = Cn/la) for the first four modes

```
f_P_C_mode1 = Cn_P_C_mode1.*la_1;
f_P_C_mode2 = Cn_P_C_mode2.*la_1;
f_P_C_mode3 = Cn_P_C_mode3.*la_1;
f_P_C_mode4 = Cn_P_C_mode4.*la_1;
```

Interpolate to obtain Phase velocity for all the frequencies for the input data with reference to the first mode

```
Cn_mode1 = interp1(f_P_C_mode1,Cn_P_C_mode1,f,'cubic');
Cn_mode2 = interp1(f_P_C_mode2,Cn_P_C_mode2,f,'cubic');
Cn_mode3 = interp1(f_P_C_mode3,Cn_P_C_mode3,f,'cubic');
Cn_mode4 = interp1(f_P_C_mode4,Cn_P_C_mode4,f,'cubic');
```

Generate the Phase Velocity curve using the first three modes.

```
Cn = Cn_mode1.*(f < f_jump_1_2) + Cn_mode2.*((f >= f_jump_1_2)&
(f < f_jump_2_3)) + Cn_mode3.*((f >= f_jump_2_3)&(f < f_jump_3_4))
+ Cn_mode4.*(f >= f_jump_3_4);
end
```

Copy the last value of the phase velocity of the P_C curve to the frequencies not covered by the curves

```
CnZ = zeros(1,N);
CnZ(1:length(Cn)) = Cn;
CnZ(length(Cn)+1:length(CnZ)) = Cn(length(Cn));
Cn = CnZ;
Cn(1) = C0;          %Set the first speed reading to fundamental wave speed
Cnc = zeros(1,N);    %Generate a vector of zeros the same length as the data
Cnc(fix(N/2)+1:N) =Cn(1:(fix(N/2)));
```

Copy the P_C curve to the negative frequencies

```
nn = 2;
for ii = (fix(N/2)):-1:1
CC1(ii) = Cn(nn);
nn = nn + 1;
end
Cnc(1:fix(N/2))= CC1;
```

Calculate the offset for the dispersion correction used in the time shift

```
offset = exp(-wn.*(z1./Cnc)*i);          %Calculate the offset
```

Multiply the data by the offset to correct for dispersion

```
yc = offset.*ys;                         %Offset phase angle
```

Use the Inverse Fast Fourier Transform to get back into the time domain

Shift the data so that it is not centered around the 0th term but the 0th term is on the left.

```
yc11 =fftshift(yc);
x2 = ifft(yc11);
```

Extract the real part of the data. The imaginary part is zero but must be removed

```
xro =real(x2);
```

Transform the data into a column vector to be sent to Excel.

```
xro1 = xro.';
x = x.';
```

A.3 Source code for data acquisition card

The following code is used to control the ADLINK data acquisition card. For details of the functions used that control the card see the Function Reference Manual [43].

```
Define Variables
Dim CardNumber As Integer
Dim card_ID As Integer      'Numeric card ID that corresponds to the card initialized
Dim voltage_range As Integer          'Input range of the card
Dim dma_size As Long                  'memory size for sample
Dim sample_rate As Single
Dim dt As Double
Dim channels_used As Integer 'is the time interval between samples
Dim trigger_mode As Integer
Dim trigger_source As Integer
Dim trigger_polarity As Integer
Dim clock_source As Integer
Dim trigger_level As Integer
Dim post_count As Integer
Dim aquired_data_buffer(1000000) As Integer
Dim A_D_status As Byte      'status of the A to D convertion, if true (1) then the
convertion is complete
Dim A_D_count As Long       'number of A to D converted during the sample
Dim computed_voltage(1000000) As Double
Dim voltage_out() As Double
Dim number_of_samples As Long
Dim count_num As Long
```

Set the value of the post trigger count.

This sub function enters a value into the post trigger count text box dependent on the number of samples selected.

```
Private Sub cboDataSize_click()
```

```
If cboDataSize.Text < 4000 Then 'if data size is < 4000
txtPostCount.Text = cboDataSize.Text-500
Else 'if data size is > 4000
txtPostCount.Text = cboDataSize.Text - 2000 'post trigger count = data size-2000
End If
End Sub
```

Draw the trigger level on the screen when a new trigger level is selected.

```
Private Sub cboTrigLvl_Click()
picScreen.Cls                'Clear the screen displaying the received data
DrawTrigLvl trigger_level    'Call the function to draw the trigger level in.
End Sub
```

Draw all the data on one screen when the *show all data* is clicked.

```
Private Sub chkAllData_Click()
ShowData channels_used
If chkAllData.Value = 1 Then
hsbData.Enabled = False
Else
hsbData.Enabled = True
End If
End Sub
```

Show or remove the data trace on the screen dependant on which channel the user wishes to display.

```
Private Sub chkChn_Click(Index As Integer)
ShowData channels_used
End Sub
```

Start the continuous scan.

```
Private Sub cmdCSStart_Click()
```

```
tmrCStartTimer.Enabled = True
End Sub
```

Stop the continuous scan.

```
Private Sub cmdCSStop_Click()
tmrCStartTimer.Enabled = False
End Sub
```

Release the car when the EXIT button is pressed.

```
Private Sub cmdExit_Click()
If card_ID >= 0 Then Release_Card (card_ID) ' test to see if the card has been
```

registered and if so release it

```
End
End Sub
```

Calls the save sub routine when the save button is pressed.

```
Private Sub cmdSave_Click()
Call mnuSave_Click
End Sub
```

When the start button is pressed the Start sub routine is called. The sub routine initializes the card, captures the data, converts the binary number into a voltage and then calls the display sub routine.

```
Private Sub cmdStart_Click()
```

General variable used during the acquisition

```
Cls
Dim result As Long
Dim result1 As Long
Dim result2 As Long
hsbData.Value = 0
```

Clear the buffer

```
For i = 0 To 1000000
    aquired_data_buffer(i) = 0
    computed_voltage(i) = 0
Next i
```

Clear the save location and print "Not Saved" in the save status.

```
lblSaveLocation.Caption = ''''
lblSaveStatus.Caption = ''Not Saved''
```

Registration of Card

```
If card_ID < 0 Then      ' test to see if the card has been registered before
cmdStart.Enabled = False      'disables the start button so that it can not be pressed
```

until the sample has been taken

```
card_ID = Register_Card(PCI_9812, CardNumber) 'Registers the card type and the
```

card number

Test to see if the card registration was successful, if not the display the message "Register Card Failed" in a message box.

```
If card_ID < 0 Then
MsgBox ''Register Card Failed''
End If
End If
```

Configuration of Card

All the data that is necessary for the configuration of the card is set by defining variables that that are taken from the setting selected by the user.

```
trigger_mode = CInt(cboTrigMode.ListIndex)
trigger_source = CInt(cboTrigSrc.ListIndex) * 8
trigger_polarity = CInt(cboTrigPol.ListIndex) * 64
clock_source = CLng(cboClkSrc.ListIndex) * 256
trigger_level = CInt(cboTrigLvl.ListIndex)          ' 128 = 0V
post_count = CInt(txtPostCount.Text)
result = AI_9812_Config(CardNumder, trigger_mode, trigger_source, _
trigger_polarity, P9812_AD2_GT_PCI Or clock_source, _
trigger_level, post_count)
```

Start the A/D conversion

Set the number of channels used. Zero is the first channel.

```
channels_used = CInt(cboChn.Text) -- 1
```

Sets the voltage range of the card to ±5V. This tells the program what solder pads have been used.

```
voltage_range = AD_B_5_V
```

Set the DMA memory size to the number of samples per channel multiplied by number of channels used

```
dma_size = CLng(cboDataSize.Text) * CLng(cboChn.Text)
```

Set the sample rate to the value selected by the user

```
sample_rate = CSng(cboRate.Text) * 1000000
dt = 1 / sample_rate
A_D_status = 0              ' reset the status to run
```

Start the continuous sampling

```
result = AI_ContScanChannels(CardNumber, channels_used,
voltage_range, aquired_data_buffer(0), dma_size, sample_rate,
ASYNCH_OP)
```

Test for end of conversion

```
While A_D_status = 0
result = AI_AsyncCheck(CardNumber, A_D_status, A_D_count)
Wend
```

Stop A to D conversion. This command must be given for the data to be assigned to the acquisition buffer.

```
result = AI_AsyncClear(CardNumber, A_D_count)
```

Convert the Signal stored in the Buffer to a voltage

```
result = AI_ContVScale(CardNumber, voltage_range, aquired_data_buffer(0),
computed_voltage(0), A_D_count)
```

Split data into array of separate channels

```
Dim samp_val As Long
samp_val = 0        'variable to count through the samples in computed voltage
number_of_samples = CLng(cboDataSize.Text) - 1
```

```
ReDim voltage_out(number_of_samples, channels_used)
For r = 0 To number_of_samples
For s = 0 To channels_used
voltage_out(r, s) = computed_voltage(samp_val)
samp_val = samp_val + 1
Next s
Next r
```

Reset the START button so it can take the next sample if pressed

```
cmdStart.Enabled = True
```

Enable the check box so that the user can select which channel is to be viewed.

```
If channels_used = 0 Then
chkChn(0).Enabled = True
chkChn(1).Enabled = False
chkChn(2).Enabled = False
chkChn(3).Enabled = False
ElseIf channels_used = 1 Then
chkChn(0).Enabled = True
chkChn(1).Enabled = True
chkChn(2).Enabled = False
chkChn(3).Enabled = False
Else
chkChn(0).Enabled = True
chkChn(1).Enabled = True
chkChn(2).Enabled = True
chkChn(3).Enabled = True
End If
```

Enable the scroll bar

```
If number_of_samples > 1000 Then
hsbData.Enabled = True
hsbData.Max = number_of_samples - 1000
Else
```

```
hsbData.Enabled = False
hsbData.Max = 1000
End If
hsbData.Value = 0 'set the scroll bar the home position
```

Set the Check boxes to be on.

```
chkChn(0).Value = 1
chkChn(1).Value = 1
chkChn(2).Value = 1
chkChn(3).Value = 1
```

Enable the View All check box

```
chkAllData.Enabled = True
```

Set the status of the View All check box to false

```
chkAllData.Value = 0
```

Call the Show data sub-routine

```
ShowData channels_used
End Sub
```

When data has been captured it is displayed with the $x-$axis as time and the $y-$axis as the amplitude of the signal in volts. The maximum and minimum amplitude is fixed at ± 5V. The default $x-$axis will show 1000 data points. If the Show All check box is selected then all the data will be shown.

```
Private Sub ShowData(ByVal channels_used As Integer)
```

Set variables used in the show data sub-routine

```
Dim w As Long, h As Long          'width and height of the display window
Dim i As Long
Dim yi As Double                  'y initial value
Dim yf As Double                  'y final value
Dim dx As Double                  'change in the step size
```

Clear the display screen

```
picScreen.Cls
```

Set the width and the height of display screen

```
w = picScreen.ScaleWidth
h = picScreen.ScaleHeight
```

Test if the Show All check box has been selected, if it has then adjust the step width.

```
If chkAllData.Value = 1 Then
dx = picScreen.ScaleWidth / number_of_samples
Else
dx = 1
End If
```

Cycle though the channels used

```
For s = 0 To channels_used
```

Set the start point of the display

```
yi = 5 - voltage_out((0 + CLng(hsbData.Value)), s)
xi = 0
xf = dx
```

Test to see if the view channel is selected, if not skip the draw data section.

```
If chkChn(s).Value = 1 Then
```

If the Show All Data is selected then draw all the data points

```
If chkAllData.Value = 1 Then
For i = 1 To number_of_samples - 1
yf = 5 - voltage_out(i, s)
picScreen.Line (xi, yi)-(xf, yf), shpLineColor(s).BackColor
xi = xf
xf = xf + dx
yi = yf
Next i
```

Else only draw 1000 points and take into account the position of the horizontal scroll bar.

```
Else
For i = 1 + CLng(hsbData.Value) To CLng(hsbData.Value) + 999
'number_of_samples - 1
yf = 5 - voltage_out(i, s)
```

```
picScreen.Line (xi, yi)-(xf, yf), shpLineColor(s).BackColor
xi = xf
xf = xf + dx
yi = yf
Next i
End If
End If
Next s
Call the Draw Trigger level sub-routine
DrawTrigLvl trigger_level
End Sub
```

When the draw trigger level sub-routine is called a horizontal line is drawn at the value set in the drop down select box.

```
Private Sub DrawTrigLvl(ByVal trigger_level As Integer)
Dim w As Long, h As Long
Dim Y As Double
w = picScreen.ScaleWidth
h = picScreen.ScaleHeight
trigger_level = CInt(cboTrigLvl.ListIndex)
Y = h * (255 - trigger_level) / 255
picScreen.Line (0, Y)-(w, Y), &H909090
End Sub
```

When the Visual Basic program of the data acquisition system is started, the following values are loaded into the select boxes and default values are set.

```
Private Sub Form_Load()
CardNumber = 0      ' There is only one card and it's number is 0
card_ID = -1        'Sets the card ID so as to test that the card Register is set correctly
Set the number of samples per channel that can be selected.
cboDataSize.AddItem ''1000''
```

```
cboDataSize.AddItem ''1200''
cboDataSize.AddItem ''2000''
cboDataSize.AddItem ''4000''
cboDataSize.AddItem ''8000''
cboDataSize.AddItem ''10000''
cboDataSize.AddItem ''12000''
cboDataSize.AddItem ''15000''
cboDataSize.AddItem ''24000''
```

Default selection is 1000 samples per channel.

```
cboDataSize.ListIndex = 0
```

Set the number of channel to be used.

```
cboChn.AddItem ''1''
cboChn.AddItem ''2''
cboChn.AddItem ''4''
```

Default selection is channel one.

```
cboChn.ListIndex = 0
```

Set the type of trigger mode.

```
cboTrigMode.AddItem ''Soft-Trigger''
cboTrigMode.AddItem ''Post-Trigger''
cboTrigMode.AddItem ''Pre-Trigger''
cboTrigMode.AddItem ''Delay-Trigger''
cboTrigMode.AddItem ''Middle-Trigger''
```

Default selection is Middle-Trigger

```
cboTrigMode.ListIndex = 4
```

Set the type of trigger source.

```
cboTrigSrc.AddItem ''Channel-0''
cboTrigSrc.AddItem ''Channel-1''
cboTrigSrc.AddItem ''Channel-2''
cboTrigSrc.AddItem ''Channel-3''
cboTrigSrc.AddItem ''Digital''
```

Default selection is Channel-0

```
cboTrigSrc.ListIndex = 0
```

Set the type of trigger polarity

```
cboTrigPol.AddItem ''Positive''
cboTrigPol.AddItem ''Negative''
Default selection is Positive
cboTrigPol.ListIndex = 0
```

Generate the numbers that can be selected for the trigger level.

```
For i# = -1.024 To 0.992 Step 0.008
cboTrigLvl.AddItem Fix(i# * 5000) / 1000
Next
```

Default selection is 0V

```
cboTrigLvl.ListIndex = 128          '128, 0V
```

Set the type of clock source.

```
cboClkSrc.AddItem ''Internal''
cboClkSrc.AddItem ''Ext Sin''
cboClkSrc.AddItem ''Ext Square''
```

Default selection is Internal

```
cboClkSrc.ListIndex = 0
```

Set the sample rate

```
cboRate.AddItem ''0.5''
cboRate.AddItem ''1''
cboRate.AddItem ''2''
cboRate.AddItem ''5''
cboRate.AddItem ''10''
cboRate.AddItem ''20''
```

Default selection is 10MHz.

```
cboRate.ListIndex = 4
```

Clear the Save status.

```
lblSaveLocation.Caption = ''''
lblSaveStatus.Caption = ''Not Saved''
```

Disable the horizontal scroll bar.

```
hsbData.Enabled = False
```

Disable the channel select check boxes

```
chkChn(0).Enabled = False
chkChn(1).Enabled = False
chkChn(2).Enabled = False
chkChn(3).Enabled = False
```

Disable the show all data check boxes

```
chkAllData.Enabled = False
End Sub
```

When the horizontal scroll bar (HSB) is changed the new position of the data is shown. This is achieved by loading the new value of the HSB into the offset for displaying the data

```
Private Sub hsbData_Change()      'when the HSB is changed
ShowData channels_used            'Redraw the data
End Sub
```

Release the cad when the EXIT button on the drop down menu is pressed.

```
Private Sub mnuExit_Click()
If card_ID >= 0 Then Release_Card (card_ID)     ' test to see if the card has
```

been registered and if so release it

```
End     'exit the program
End Sub
```

When the save button is pressed or the File_Save menu is selected the saved data sub-routine is called. The save sub-routine calls up a the Windows standard SAVE AS command dialog box. The command dialog box in filtered so as only to allow TXT files to be used. The save sub-routine saves the time and all the data that was entered on the sheet along with the data.

```
Private Sub mnuSave_Click()
Dim time_of_sample As Double
```

```
time_of_sample = 0
wrap$ = Chr$(13) & Chr$(10)
```

Call the SAVE AS command dialog box

```
CommonDialog1.ShowSave
```

Set filter to TXT file type

```
CommonDialog1.Filter = ''Text files (*.TXT)|*.TXT''
```

If a file name has been entered then open a TXT file. If no file name has been entered then display a message box the indicates that the data has not been saved

```
If CommonDialog1.FileName <> '''' Then
Open CommonDialog1.FileName For Output As #1     'open the TXT file
```

Print the description of data to the text file

```
Print #1, ''Description of Data'' & Chr(9); txtLabDescription.Text
```

Print Date and Time to the text file

```
Print #1, ''Date:'' & Chr(9); Date$
Print #1, ''Time:'' & Chr(9); Time$
```

Print sample rate to the text file

```
Print #1, ''Rate:'' & Chr(9); sample_rate & Chr(9) & ''MHz''
```

Print Striker Data to the text file

```
Print #1, ''Striker Data''
Print #1, ''Length:'' & Chr(9); txtSrikerLength.Text & Chr(9)
& Chr(9) & ''Diameter:'' & Chr(9) & txtStrikerDiameter.Text
```

Print speed trap data to the text file

```
Print #1, ''Speed Trap Data''
Print #1, ''Time:'' & Chr(9); txtTrapTime.Text & Chr(9) & Chr(9)
& ''Trap Gap'' & Chr(9) & txtTrapGap.Text
```

Print Specimen Data to the text file

```
Print #1, ''Speciment Data''
Print #1, ''Length:'' & Chr(9); txtSpecLength.Text & Chr(9) & Chr(9)
 & ''Diameter:'' & Chr(9) & txtSpecDiameter.Text & Chr(9) & Chr(9) &
  ''Material:'' & Chr(9); txtSpecMat.Text
```

Print Bridge Voltage to the text file

```
Print #1, ''Bridge Voltage ''
Print #1, ''Voltage:'' & Chr(9); txtBVolt.Text & Chr(9) & ''V''
```

Print headings for the voltages to the text file

```
If channels_used = 0 Then
Print #1, ''Time'' & Chr(9) & ''Channel 0''
ElseIf channels_used = 1 Then
Print #1, ''Time'' & Chr(9) & ''Channel 0'' & Chr(9); ''Channel 1''
Else
Print #1, ''Time'' & Chr(9) & ''Channel 0'' & Chr(9); ''Channel 1'' &
 Chr(9) & ''Channel 2'' & Chr(9) & ''Channel 3''
End If
```

Print the data voltages to the text file

```
For i% = 0 To number_of_samples
If channels_used = 0 Then
Print #1, time_of_sample & Chr(9) & voltage_out(i%, 0) '& Chr(9) &
 aquired_data_buffer(i%)
ElseIf channels_used = 1 Then
Print #1, time_of_sample & Chr(9) & voltage_out(i%, 0) & Chr(9);
 voltage_out(i%, 1)
Else
Print #1, time_of_sample & Chr(9) & voltage_out(i%, 0) & Chr(9);
 voltage_out(i%, 1) & Chr(9) & voltage_out(i%, 2) & Chr(9) &
 voltage_out(i%, 3)
End If
time_of_sample = time_of_sample + dt
Next i
```

Acknowledge that the file has been saved and the file location on the form

```
lblSaveLocation.Caption = CommonDialog1.FileName
lblSaveStatus.Caption = ''Saved''
Else
MsgBox ''Not Saved''
```

```
End If
Close #1 'close the TXT file
End Sub
```

When the continuous scan is selected a timer is used to take samples.

```
Private Sub tmrCStartTimer_Timer()
Call cmdStart_Click                    'Call the Start sub-routine
tmrCStartTimer.Enabled = True          'Reset the timer
End Sub
```

Appendix B

Test Results

B.1 Compression test results for material tested on the SHPB

B.1.1 Mild Steel

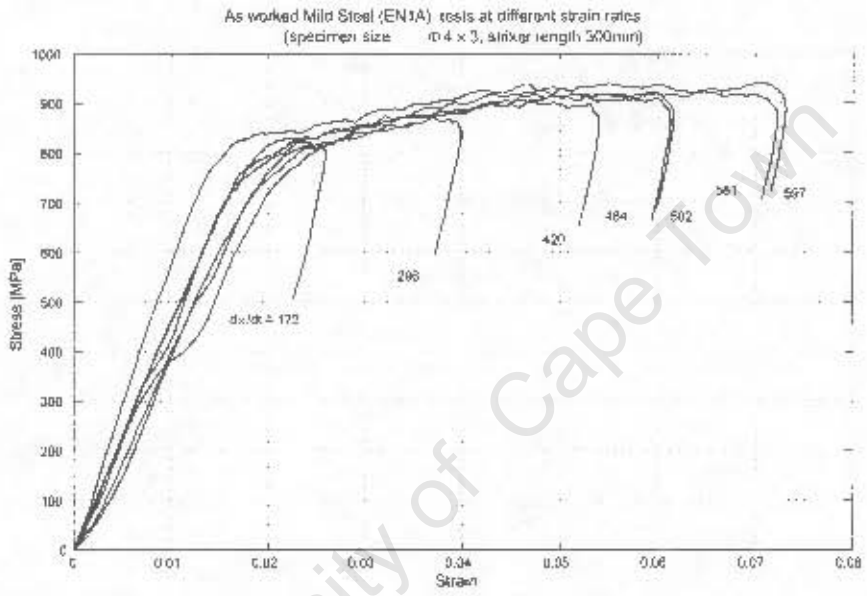

SHPB compression test for as received mild steel (EN1A) at different strain rates (specimen size Φ4 x 3, striker length 300mm)

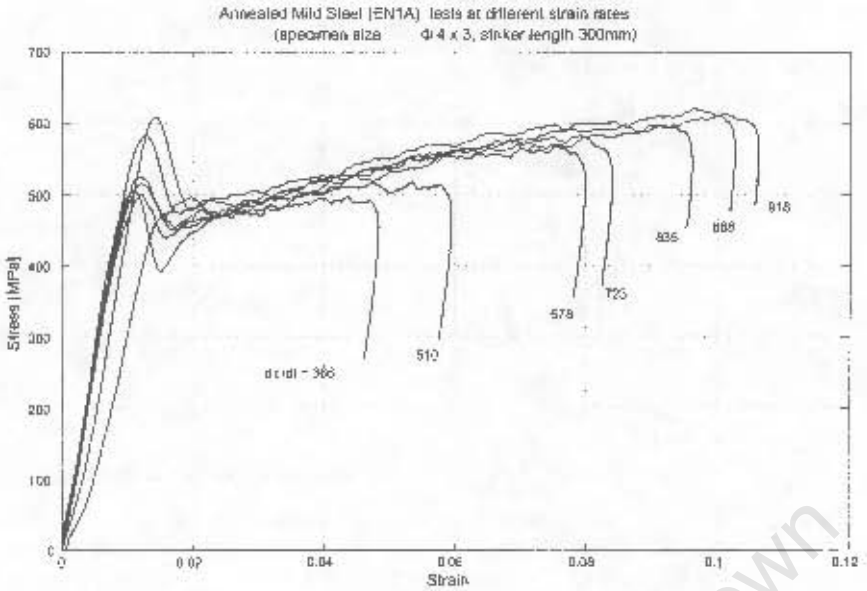

SHPB compression test for annealed mild steel (EN1A) at different strain rates (specimen size Φ4 x 3, striker length 300mm)

B.1.2 Aluminium

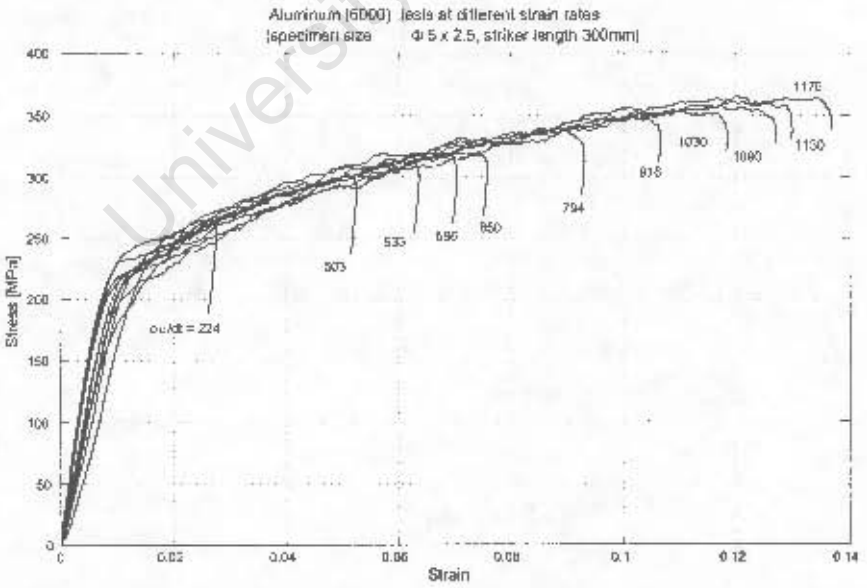

SHPB compression test for annealed mild steel (EN1A) at different strain rates (specimen size Φ5 x 2.5, striker length 300mm)

B.1.3 Copper

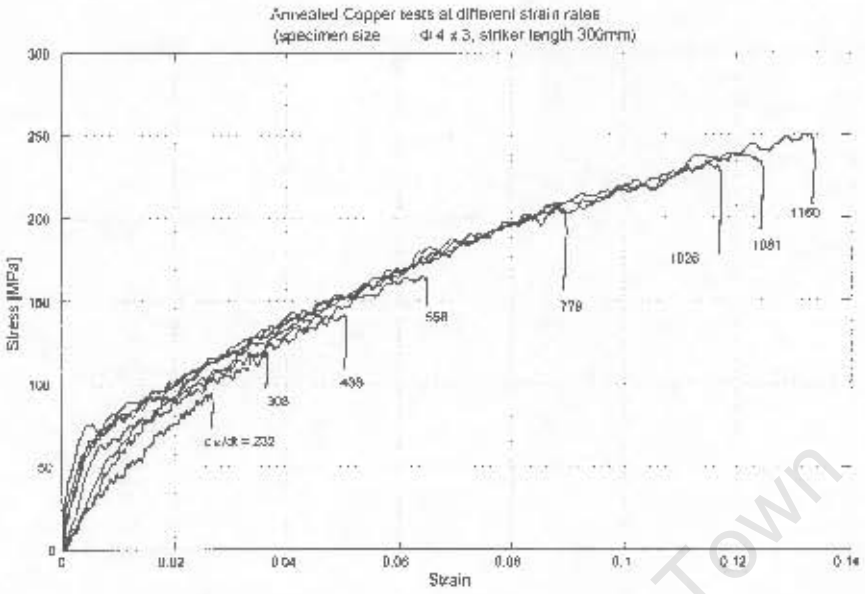

SHPB compression test for annealed copper at different strain rates (specimen size Φ4 x 3, striker length 300mm)

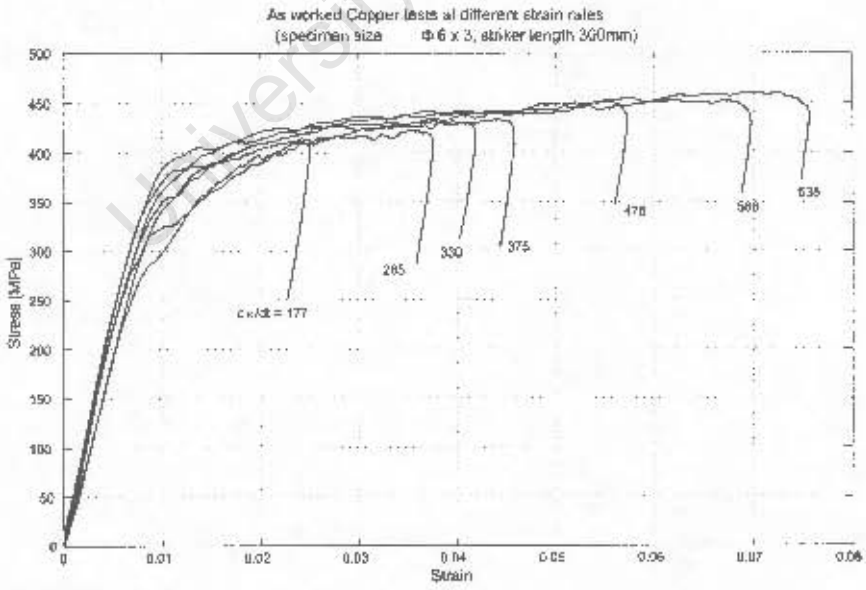

SHPB compression test for as received copper at different strain rates (specimen size Φ6 x 3, striker length 300mm)

B.2 Quasi-static tensile test results

B.2.1 Mild Steel

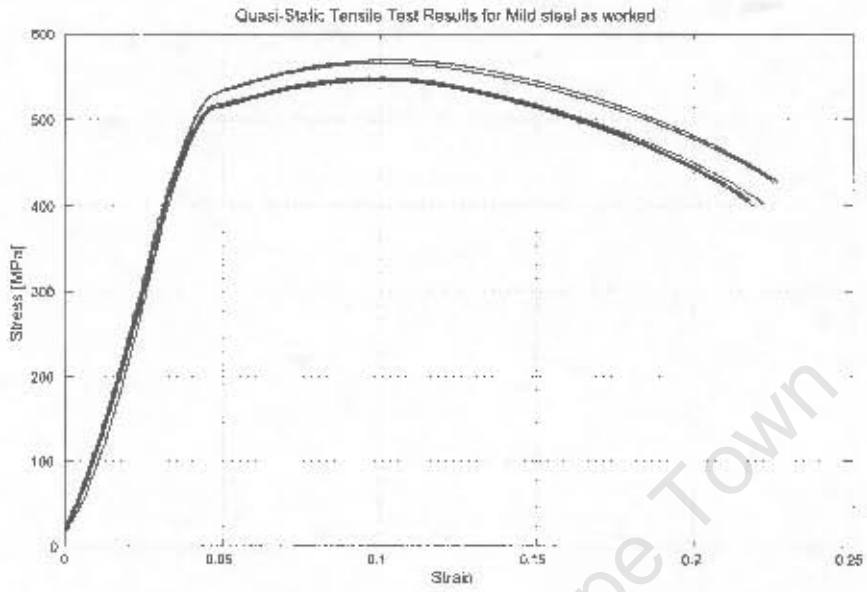

Quasi-static tensile test results for mild steel as received

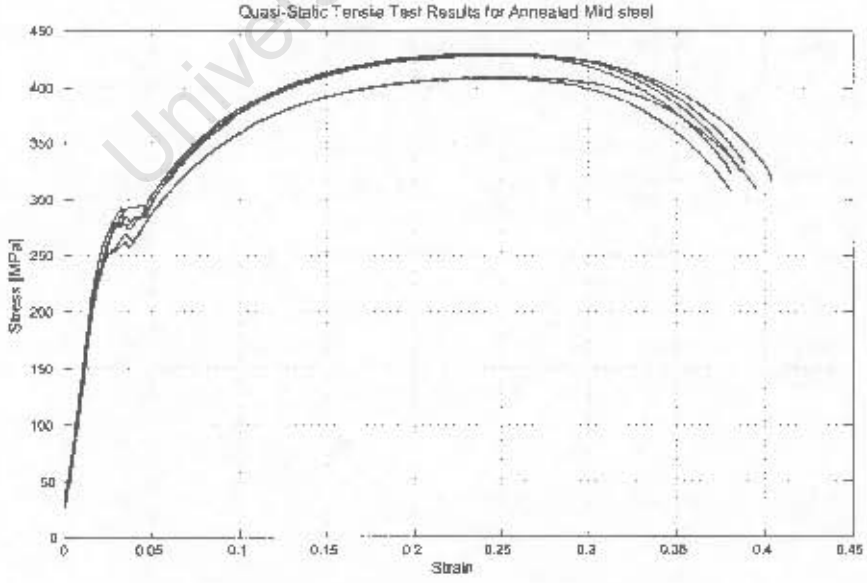

Quasi-static tensile test results for annealed mild steel.

B.2.2 Aluminium

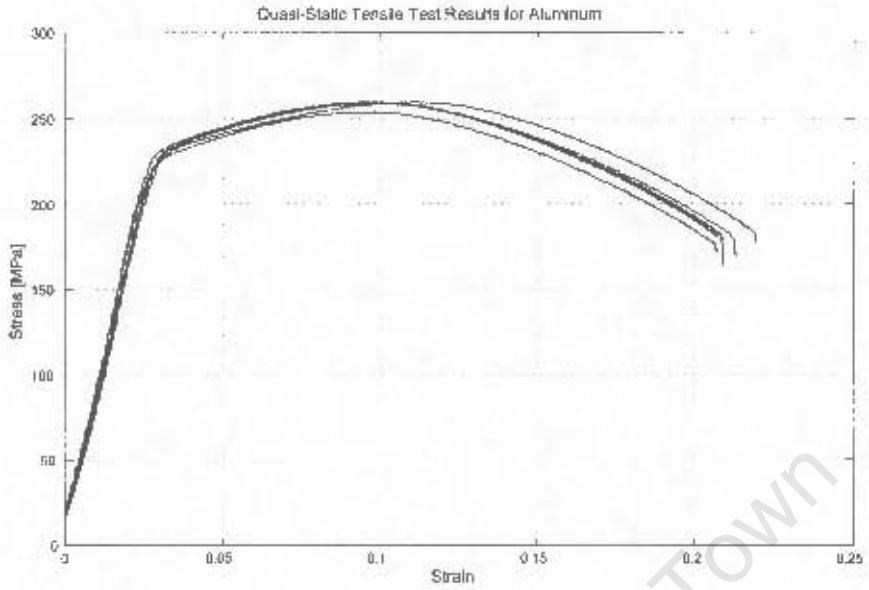

Quasi-static tensile test results for aluminum

B.2.3 Copper

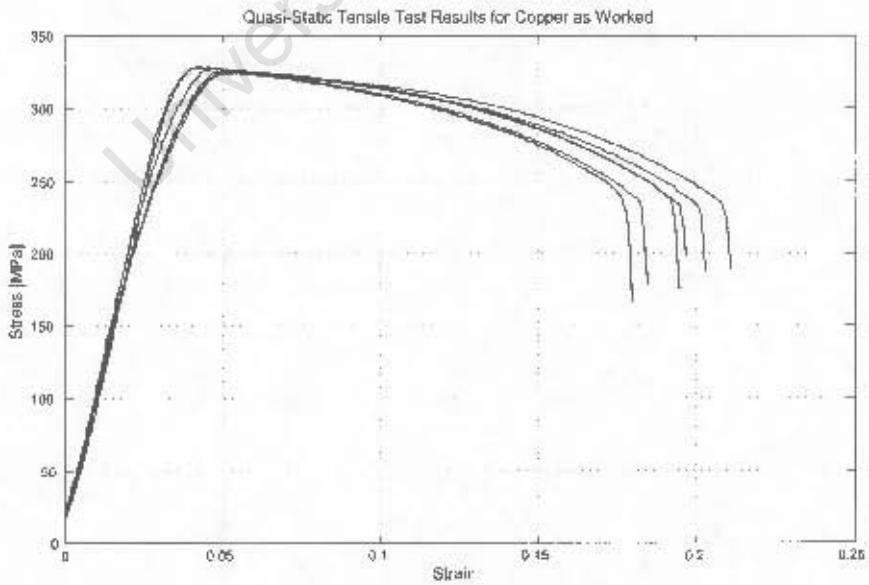

Quasi-static tensile test results for copper as received

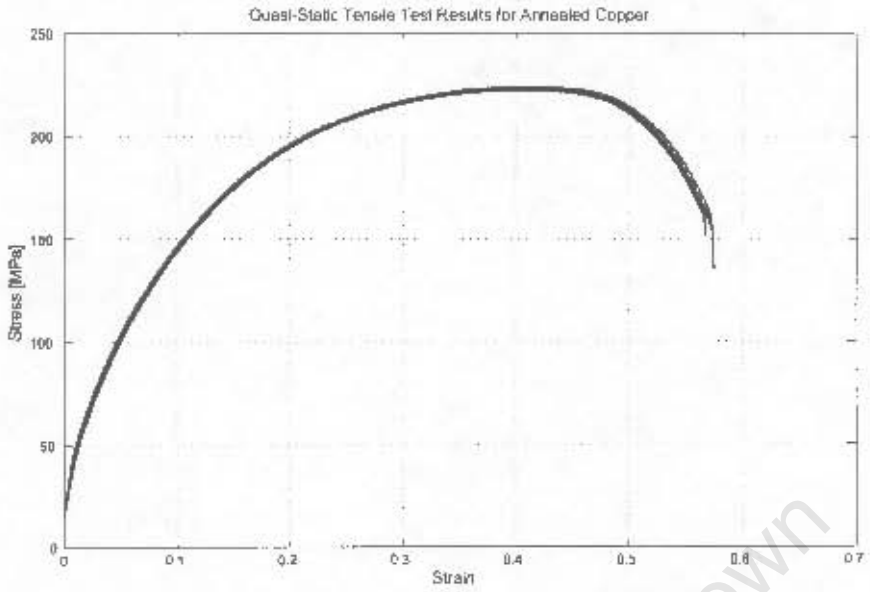

Quasi-static tensile test results for annealed copper

Appendix C

Gas gun Operation Procedure

C.1 General Safety Instructions

- Do not operate the gas gun alone and without permission.
- Wear earplugs or some other means of aural protection.
- Make sure that there are adequate barriers to prevent projectile recoil when performing ballistic tests.

C.2 Preliminary Checks

Before charging the gas gun cylinders make sure of the following:

1. There is no pressured air in the primary or trigger cylinder. If there is, follow the *depressurising sequence* of the instructions.
2. The gas bottle valve and the pressure regulator valves are closed.
3. The trigger circuit is switched off.
4. There is no projectile in the barrel.

C.3 Cylinder Charging

Carry out the following procedure when pressurising the cylinders:

1. Open the gas bottle valve and check that the primary regulator valve registers the bottle pressure.
2. Pressurise the trigger cylinder. NB: The trigger cylinder must always be at a higher pressure than the primary cylinder.

3. Pressurise the primary cylinder. Set the primary cylinder to the desired test pressure by adjusting the primary regulator valve. If the desired test pressure is lower than the pressure in the primary cylinder then close the primary regulator valve and open the bleed of valve to drop the pressure in the primary cylinder.

4. Conduct a test fire by following the *firing sequence* but without a projectile.

C.4 Firing Sequence

Carry out the following procedure when firing projectiles:

1. Check that the trigger circuit is switched off.

2. Check that the primary cylinder pressure is correct.

3. Load the projectile.

4. Switch on the trigger circuit.

5. Stand to the rear of the gun, well clear of the muzzle.

6. Lift the safety switch and, while keeping it up, press the trigger button to fire the gas gun.

7. Switch off the trigger circuit.

Note:

- The cylinders do not have to be depressurised after each firing.
- If at any time the pressure regulator dials do not register a pressure when the valves are open, depressurise the gas gun and have them checked.

C.5 Depressurising Sequence

Carry out the following procedure when depressuring the cylinders:

1. Close the gas bottle valve.

2. Open the bleed off valve to depressurise the primary cylinder pressure.

3. Conduct a test fire by following the firing sequence but without a projectile, until the pressure regulator dials on the trigger cylinder indicate a pressure of zero.

4. Close the pressure regulator valving.

5. Switch off the trigger circuit.

Appendix D

Drawings

Drawing Number	Description
GASGUN-000-00	GA FOR SHPB TEST RIG
GASGUN-001-01	GA FOR GUN SUPPORTS
GASGUN-001-02	GUN SUPPORT
GASGUN-001-03	MAIN BED
GASGUN-001-04	LEG PARTS
GASGUN-001-05	GUSSETS
GASGUN-001-06	FOOT PLATES
GASGUN-001-07	TANK SUPPORT
GASGUN-002-01	GA FOR BAR SUPPORTS
GASGUN-002-02	UPPER CLAMP
GASGUN-002-03	LOWER SUPPORT
GASGUN-002-04	UPPER SUPPORT
GASGUN-002-05	LOWER CLAMP
GASGUN-002-06	BAR SUPPORT BUSH
GASGUN-003-01	GA FOR BARREL SUPPORTS
GASGUN-003-02	UPPER CLAMP
GASGUN-003-03	SUPPORT BLOCK
GASGUN-004-01	STRIKERS AND BARS
GASGUN-005-01	SPEED SENSOR HOUSING

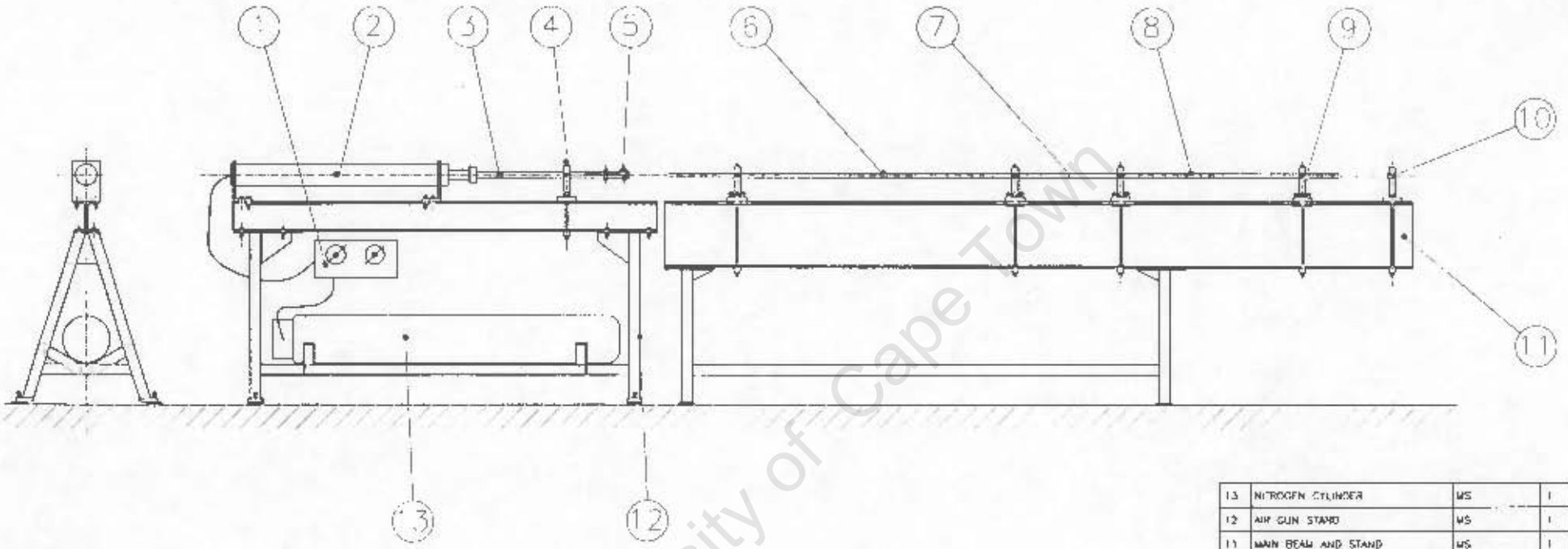

PART No.	DESCRIPTION	MATERIAL	No. OFF	REMARKS
13	NITROGEN CYLINDER	MS	1	
12	AIR GUN STAND	MS	1	
11	MAIN BEAM AND STAND	MS	1	
10	END STOP	MS	1	
9	BAR SUPPORT	MS	4	
8	TRANSMITTER BAR	SILVER STEEL	1	
7	SPECIMEN			
6	INCIDENT BAR	SILVER STEEL	1	
5	SPEED TRAP	TEFLON	2	
4	BARREL SUPPORT	MS	1	
3	BARREL		1	
2	AIR GUN		1	
1	CONTROL VALVING		2	

AIR GUN

UNIVERSITY OF CAPE TOWN
DEPARTMENT OF MECHANICAL ENGINEERING

TITLE
GA FOR SHPB TEST RIG

DIMENSIONS IN MILLIMETRES (mm) TOLERANCE UNLESS OTHERWISE STATED ±0.1

SCALE 1 : 20

DATE 29/05/2001

SHEET 1 OF 1

DRAWN BY S.T.MARAIS

DRAWING NUMBER GASGUN-000-00

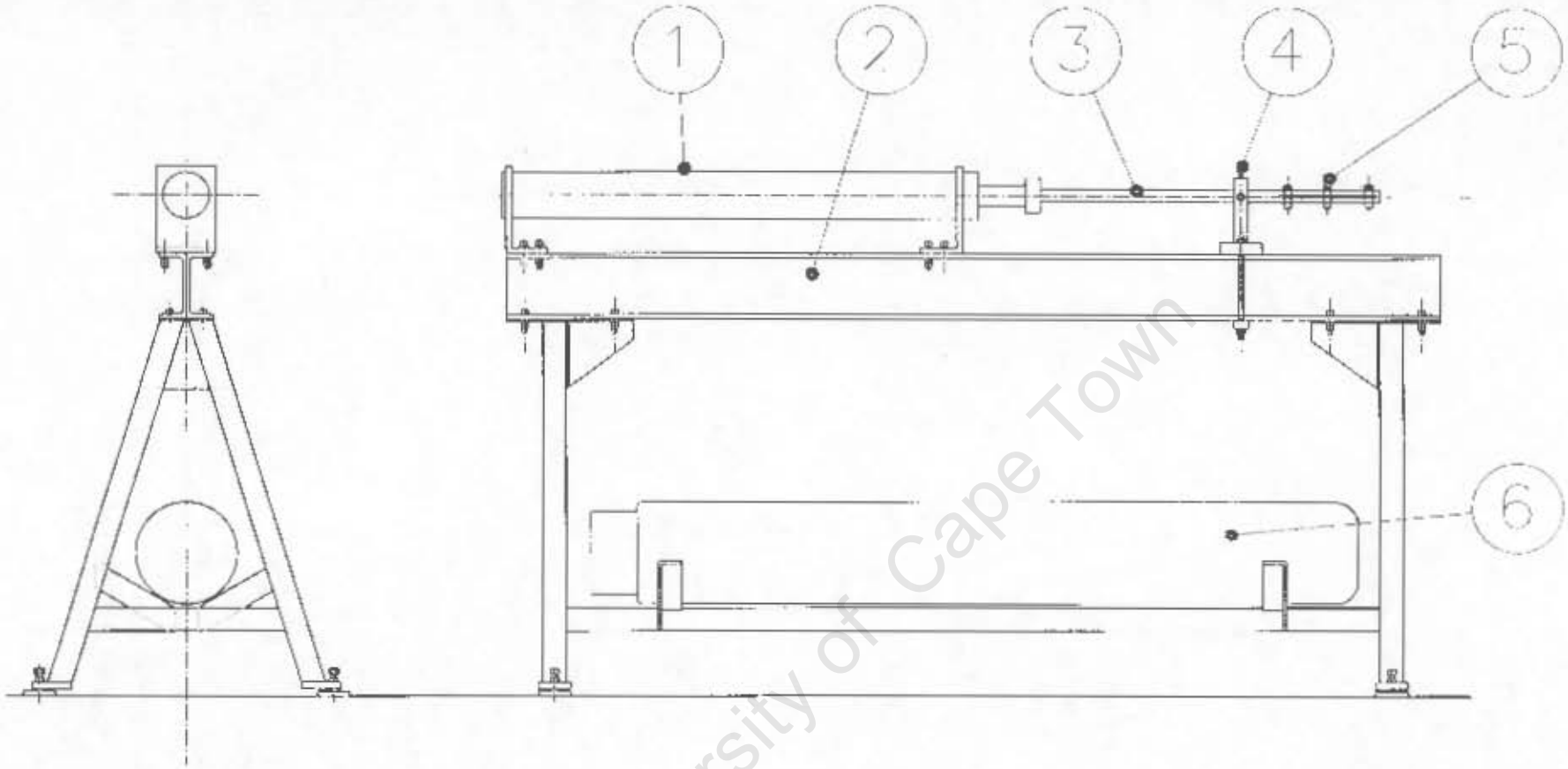

PART No.	DESCRIPTION	MATERIAL	No. OFF	REMARKS
6	TANK			
5	SPEED TRAP			
4	BARREL SUPPORT			
3	BARREL			
2	AIR GUN SUPPORT			
1	AIR GUN			

AIR GUN

UNIVERSITY OF CAPE TOWN
DEPARTMENT OF MECHANICAL ENGINEERING

TITLE
GA FOR GUN SUPPORTS

DIMENSIONS IN MILLIMETERS (mm)
TOLERANCE UNLESS OTHERWISE STATED
0.1

SCALE 1 : 10

DATE 23/08/2000

SHEET 1 OF 7

DRAWN BY S.T.MARAIS

DRAWING NUMBER GASGUN-001-01

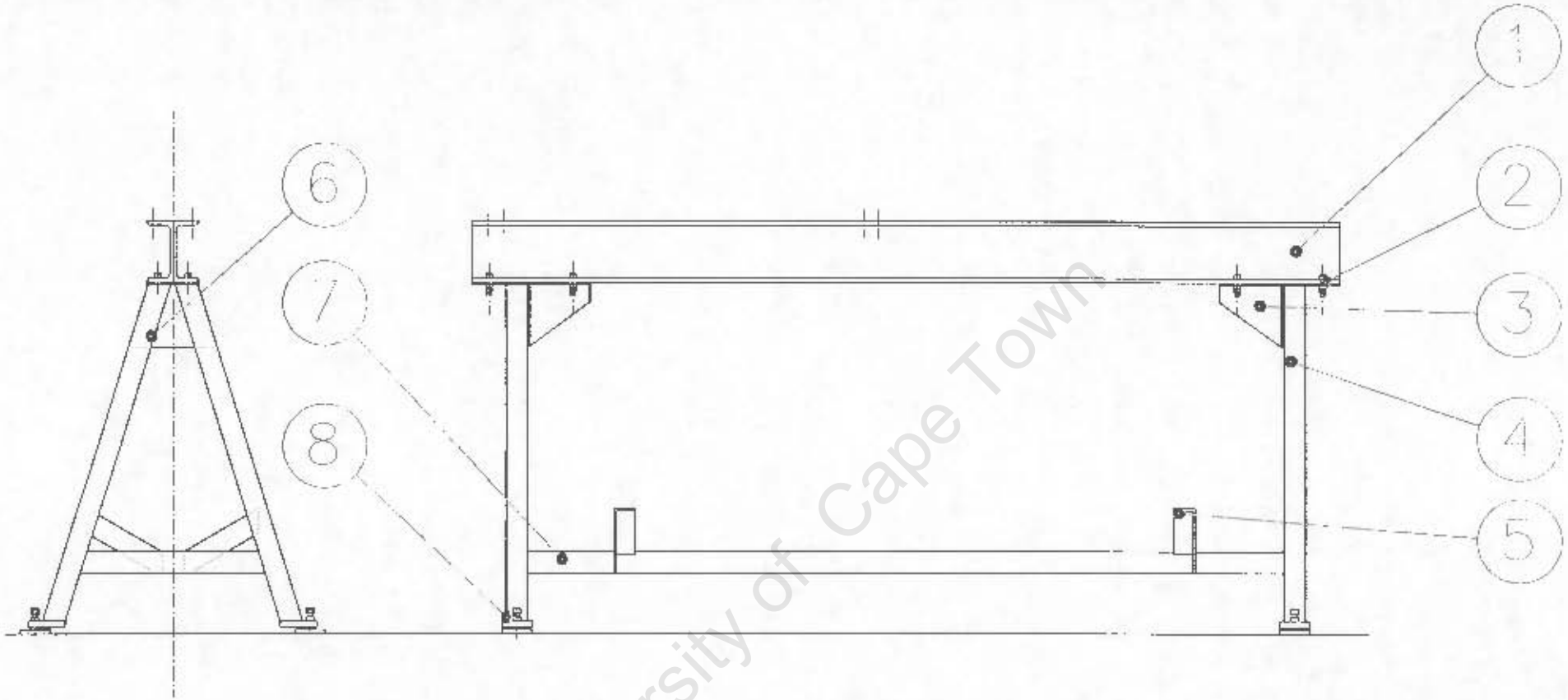

PART No.	DESCRIPTION	MATERIAL	No. OFF	REMARKS
8	FOOT	MS	4	
7	TANK MAIN SUPPORT	MS	1	
6	BACK GUSSET	MS	2	
5	TANK SUPPORT	MS	4	
4	LEG	MS	4	
3	SIDE GUSSET	MS	2	
2	BASE PLATE	MS	2	
1	DEO 140 X 80 CH	MS	2	

AIR GUN

UNIVERSITY OF CAPE TOWN
DEPARTMENT OF MECHANICAL ENGINEERING

TITLE
GUN SUPPORT

DIMENSIONS IN MILLIMETERS (mm) TOLERANCE UNLESS OTHERWISE STATED 0.1

SCALE 1 : 10

DATE 23/08/2000

SHEET 2 OF 7

DRAWN BY S.T.MARAIS

DRAWING NUMBER GASGUN-001-02

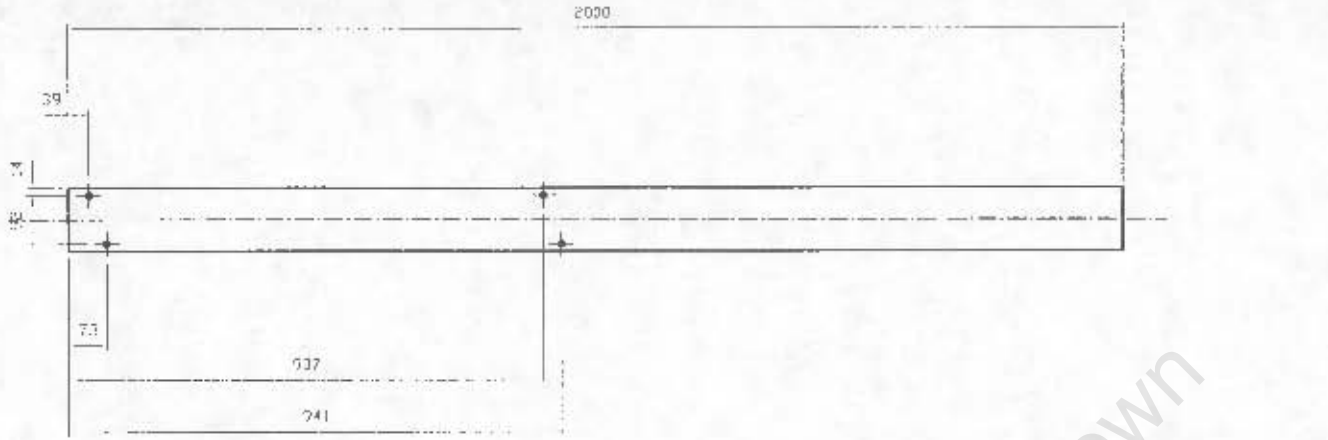

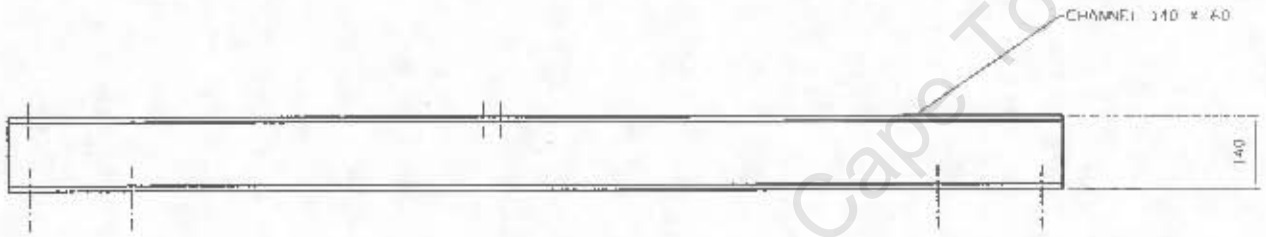

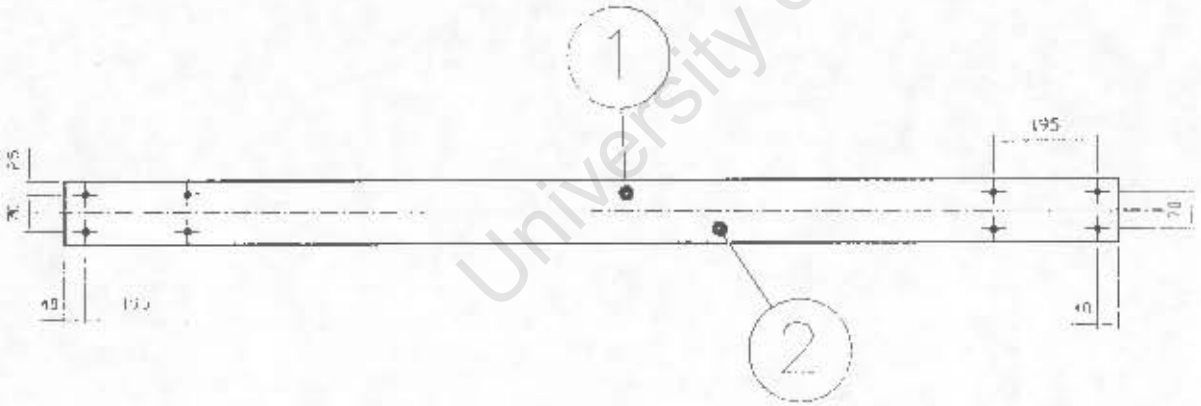

ALL HOLES Ø11
WELD CHANNELS TOGETHER AND THEN DRILL HOLES

PART No.	DESCRIPTION	MATERIAL	No OFF	REMARKS
2	LEFT SUPPORT	MS	1	
1	RIGHT SUPPORT	MS	1	

AIR GUN

UNIVERSITY OF CAPE TOWN
DEPARTMENT OF MECHANICAL ENGINEERING

TITLE
MAIN BED

DIMENSIONS IN MILLIMETERS (mm)
TOLERANCE UNLESS OTHERWISE STATED
0.1

SCALE: 1 : 10
DATE: 23/08/2000
SHEET 5 OF 7

DRAWN BY: S.T. MARAIS

DRAWING NUMBER: GASGUN-001-03

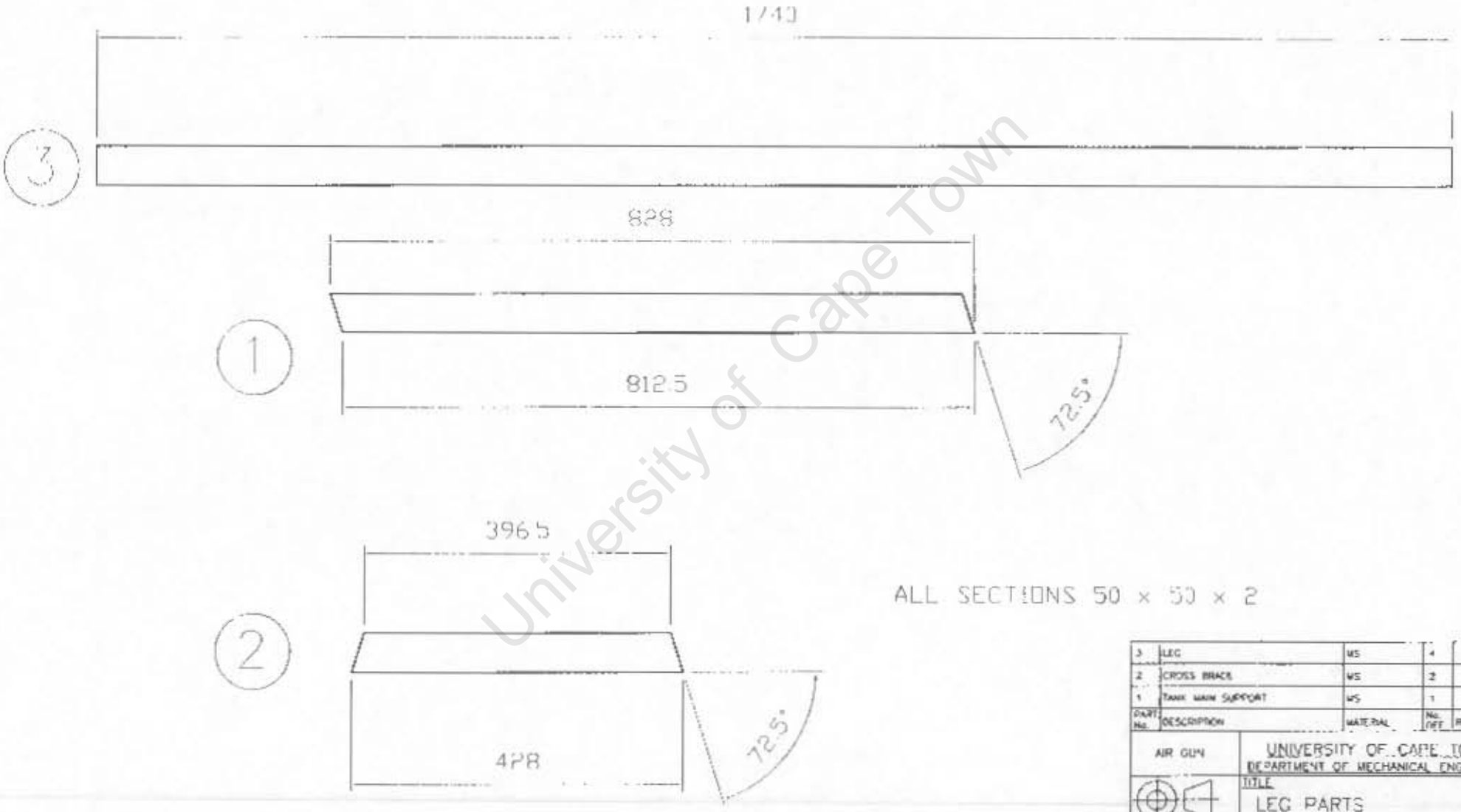

PART No.	DESCRIPTION	MATERIAL	No. OFF	REMARKS
3	LEG	MS	4	
2	CROSS BRACE	MS	2	
1	TANK MAIN SUPPORT	MS	1	

AIR GUN

UNIVERSITY OF CAPE TOWN
DEPARTMENT OF MECHANICAL ENGINEERING

TITLE
LEG PARTS

DIMENSIONS IN MILLIMETERS (mm) TOLERANCE UNLESS OTHERWISE STATED ±1

SCALE 1 : 5 | DATE 23/08/2000 | SHEET 4 OF 7

DRAWN BY S.T. MARAIS

DRAWING NUMBER GASGUN-001-04

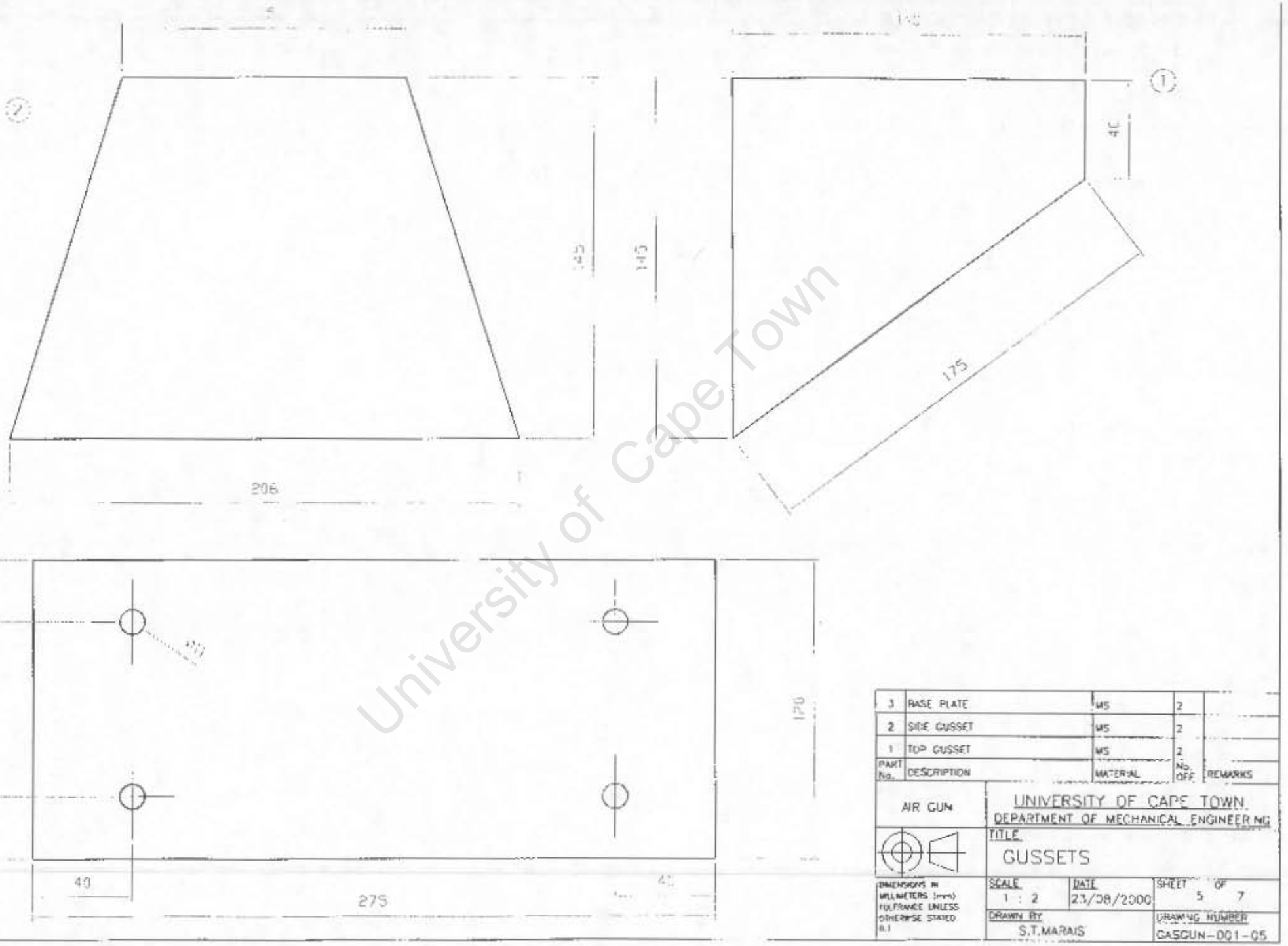

PART No.	DESCRIPTION	MATERIAL	No. OFF	REMARKS
3	BASE PLATE	MS	2	
2	SIDE GUSSET	MS	2	
1	TOP GUSSET	MS	2	

AIR GUN

UNIVERSITY OF CAPE TOWN
DEPARTMENT OF MECHANICAL ENGINEERING

TITLE
GUSSETS

DIMENSIONS IN MILLIMETERS (mm) TOLERANCE UNLESS OTHERWISE STATED ± 1

SCALE 1 : 2

DATE 23/08/2000

SHEET 5 OF 7

DRAWN BY S.T.MARAIS

DRAWING NUMBER GASGUN-001-05

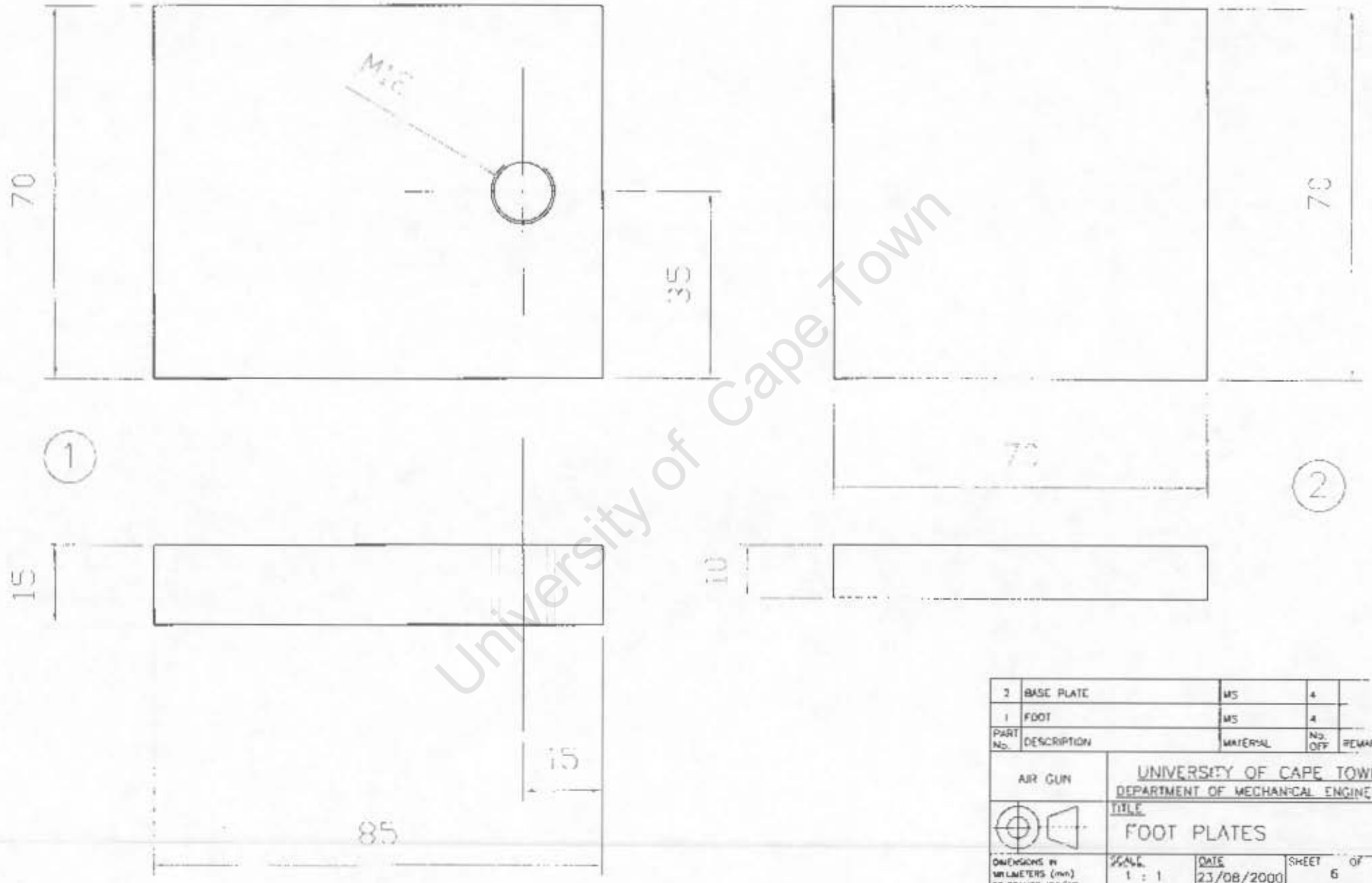

PART No.	DESCRIPTION	MATERIAL	No. OFF	REMARKS
2	BASE PLATE	MS	4	
1	FOOT	MS	4	

AIR GUN

UNIVERSITY OF CAPE TOWN
DEPARTMENT OF MECHANICAL ENGINEERING

TITLE
FOOT PLATES

DIMENSIONS IN MILLIMETERS (mm)
TOLERANCE UNLESS OTHERWISE STATED ±1

SCALE 1 : 1

DATE 23/08/2000

SHEET 6 OF 7

DRAWN BY S.T.MARAIS

DRAWING NUMBER GASGUN-001-06

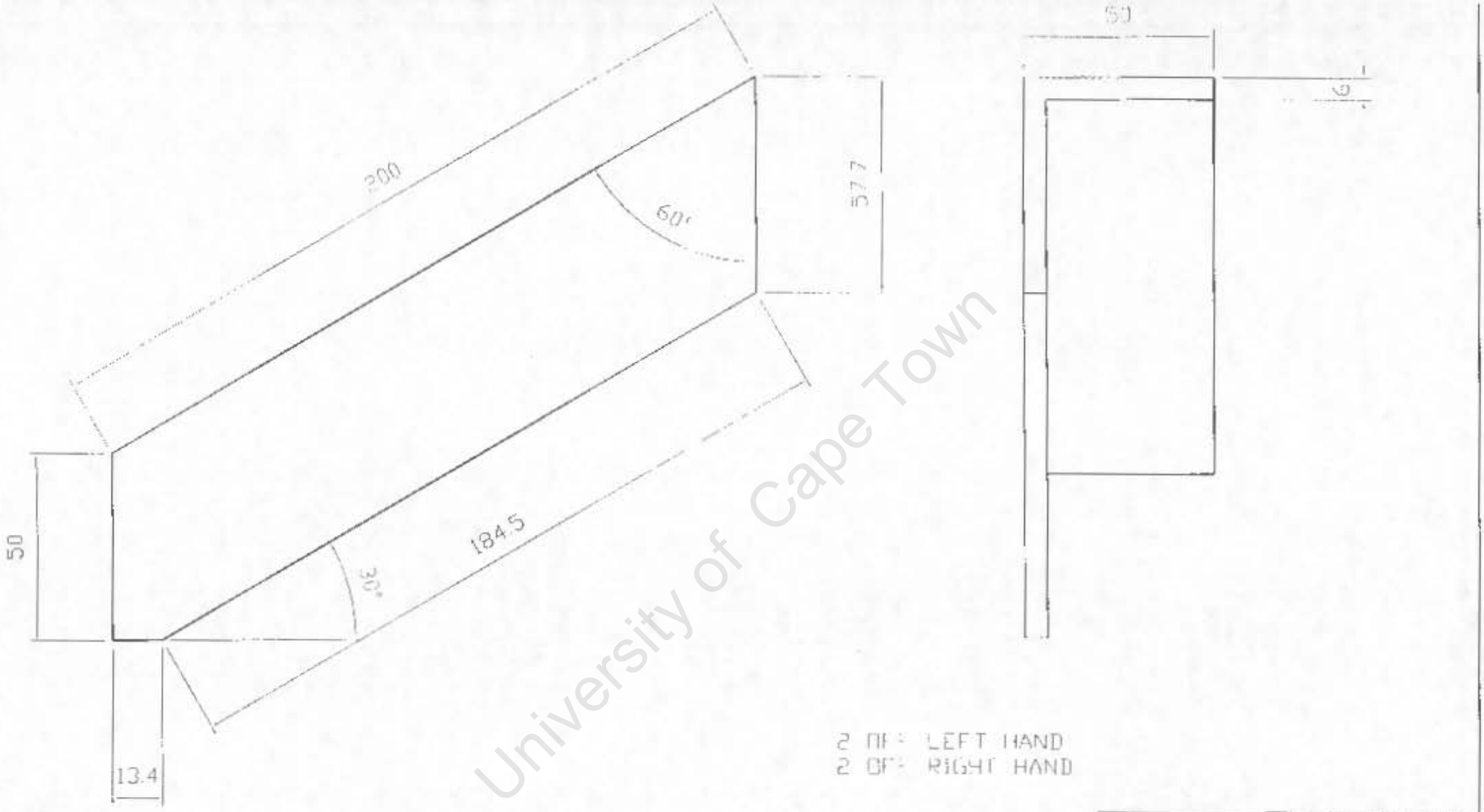

PART NO.	DESCRIPTION	MATERIAL	No. OFF	REMARKS
2	RIGHT TANK SUPPORT	MS	2	
1	LEFT TANK SUPPORT	MS	2	

AIR GUN

UNIVERSITY OF CAPE TOWN
DEPARTMENT OF MECHANICAL ENGINEERING

TITLE
TANK SUPPORT

DIMENSIONS IN MILLIMETERS (mm) TOLERANCE UNLESS OTHERWISE STATED ±0.1

SCALE 1 : 2

DATE 23/08/2000

SHEET 7 of 7

DRAWN BY S.T.MARAIS

DRAWING NUMBER GASGUN-001-07

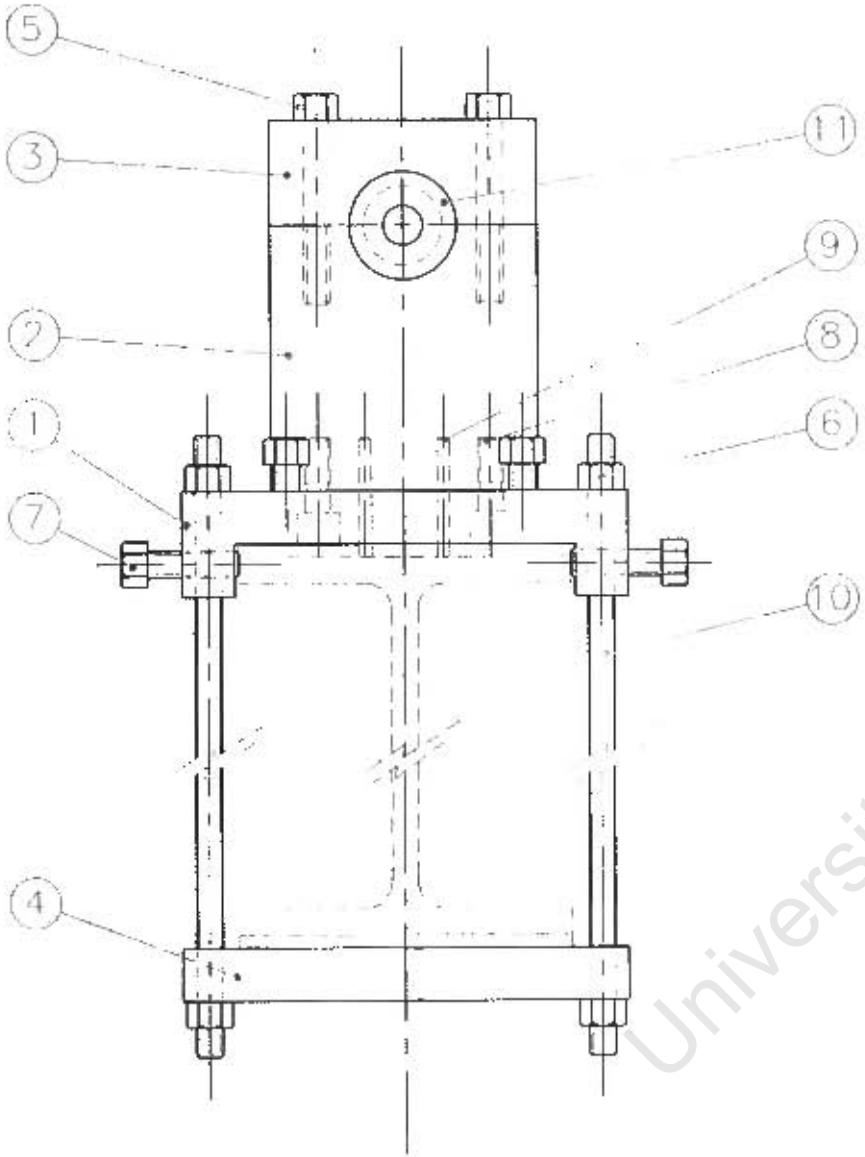

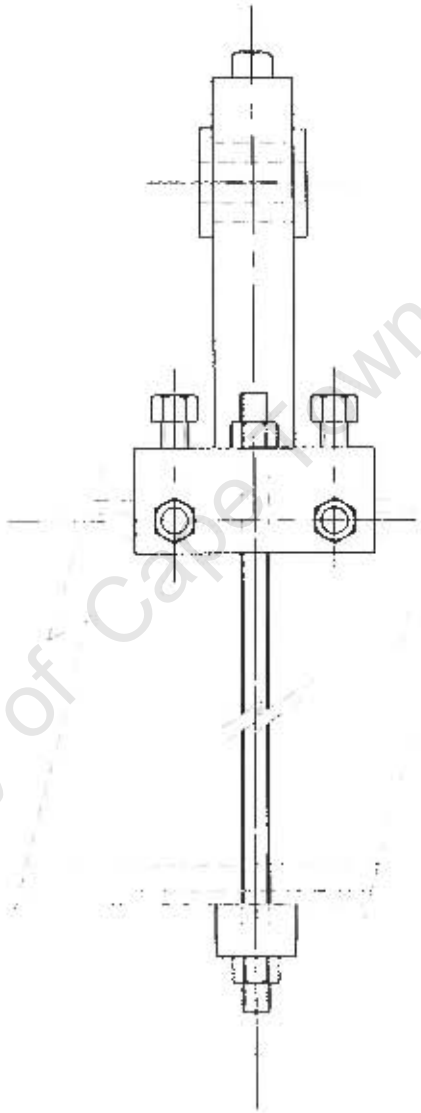

PART No.	DESCRIPTION	MATERIAL	No. OFF	REMARKS
11	BUSH	TEFLON	2	
10	M10 THREADED BAR 400 LG.		6	
9	ø5 DOWEL PIN	SILVER STEEL	6	
8	M10 CAP SCREW		4	
7	M10 X 30 BOLT		24	
6	M10 NUT		12	
5	M10 X 65 BOLT		4	
4	LOWER CLAMP	MS	3	
3	UPPER SUPPORT	MS	2	
2	LOWER SUPPORT	MS	2	
1	UPPER CLAMP	MS	2	

AIR GUN

UNIVERSITY OF CAPE TOWN
DEPARTMENT OF MECHANICAL ENGINEERING

TITLE
GA FOR BAR SUPPORTS

DIMENSIONS IN MILLIMETRES (mm) TOLERANCE UNLESS OTHERWISE STATED ±0.1

SCALE 1 : 2

DATE 11/08/2000

SHEET 1 OF 5

DRAWN BY S.T.MARAIS

DRAWING NUMBER CASGUN-002-01

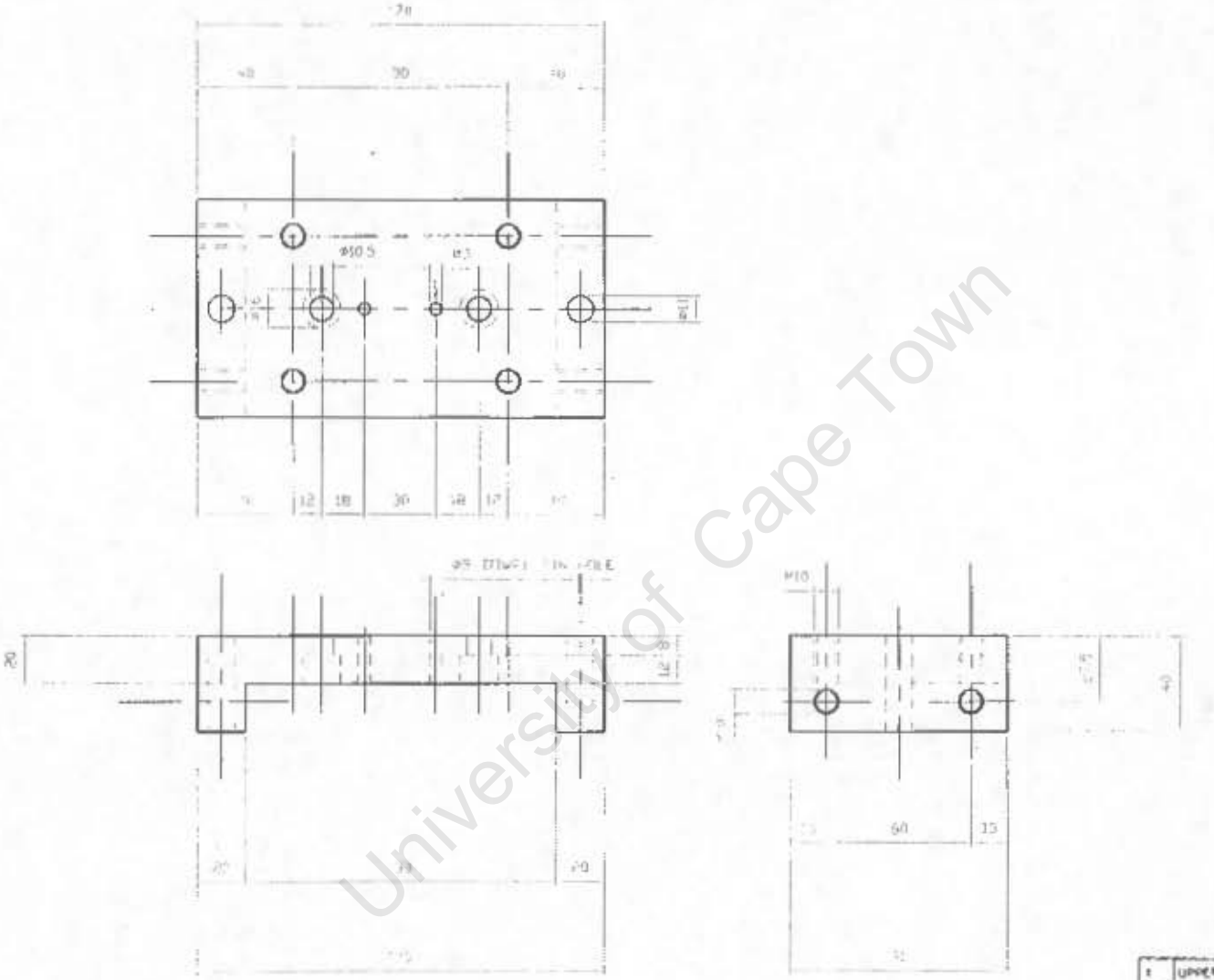

1	UPPER CLAMP	MS	2	REMARKS
PART NO.	DESCRIPTION	MATERIAL	NO. OFF	REMARKS

AIR GUN	UNIVERSITY OF CAPE TOWN DEPARTMENT OF MECHANICAL ENGINEERING	
	TITLE UPPER CLAMP	
DIMENSIONS IN MILLIMETRES (mm) TOLERANCE UNLESS OTHERWISE STATED ± 1	SCALE 1 : 2	DATE 11/08/2000
	DRAWN BY S.T.MARAIS	DRAWING NUMBER CASGUN-002-02
		SHEET 2 OF 6

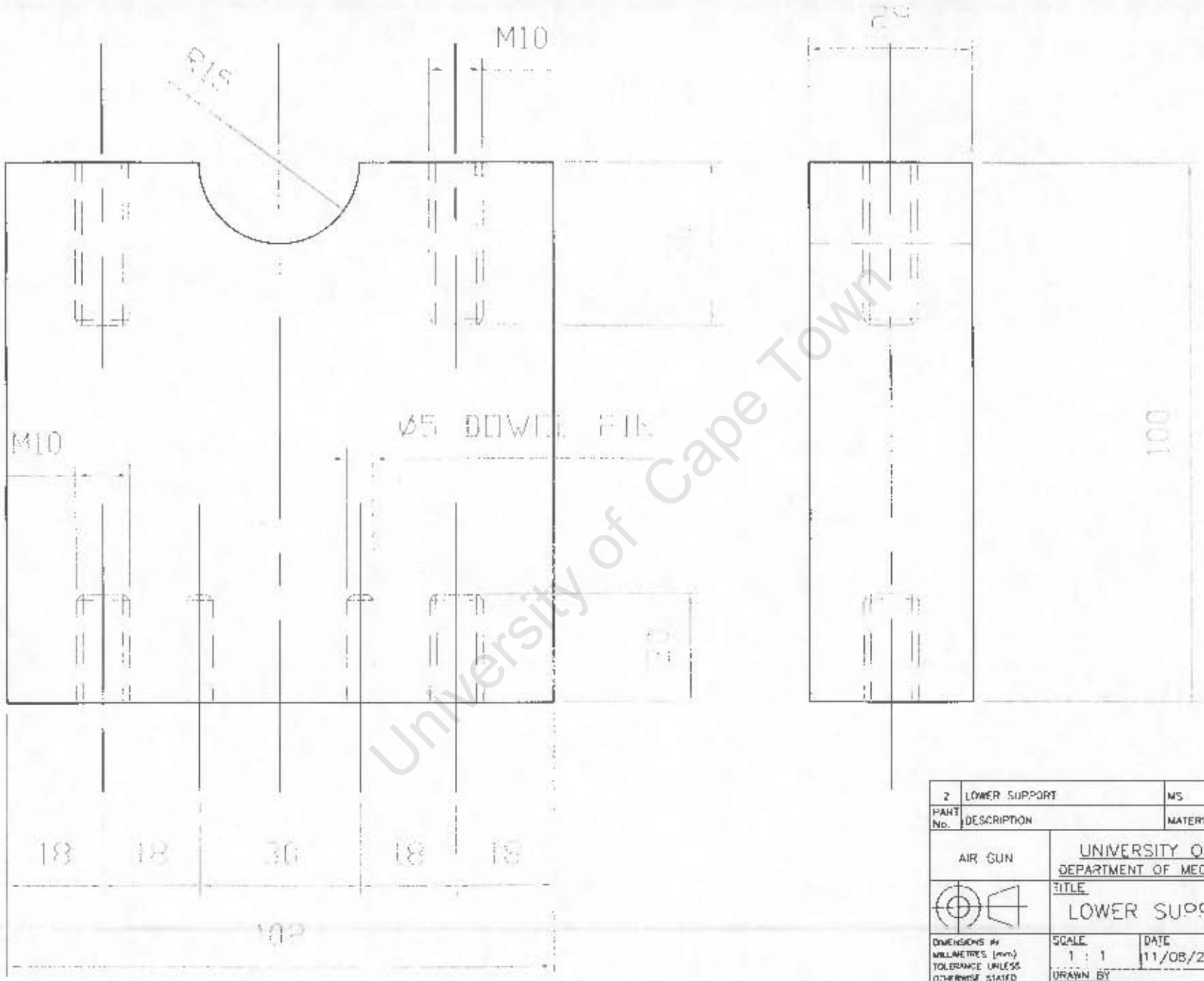

PART No.	DESCRIPTION	MATERIAL	No OFF	REMARKS
2	LOWER SUPPORT	MS	2	

AIR GUN	UNIVERSITY OF CAPE TOWN DEPARTMENT OF MECHANICAL ENGINEERING		
	TITLE LOWER SUPPORT		
DIMENSIONS IN MILLIMETRES (mm) TOLERANCE UNLESS OTHERWISE STATED 0.1	SCALE 1 : 1	DATE 11/08/2000	SHEET OF 3 5
	DRAWN BY S.T.MARAIS		DRAWING NUMBER GASGUN-002 03

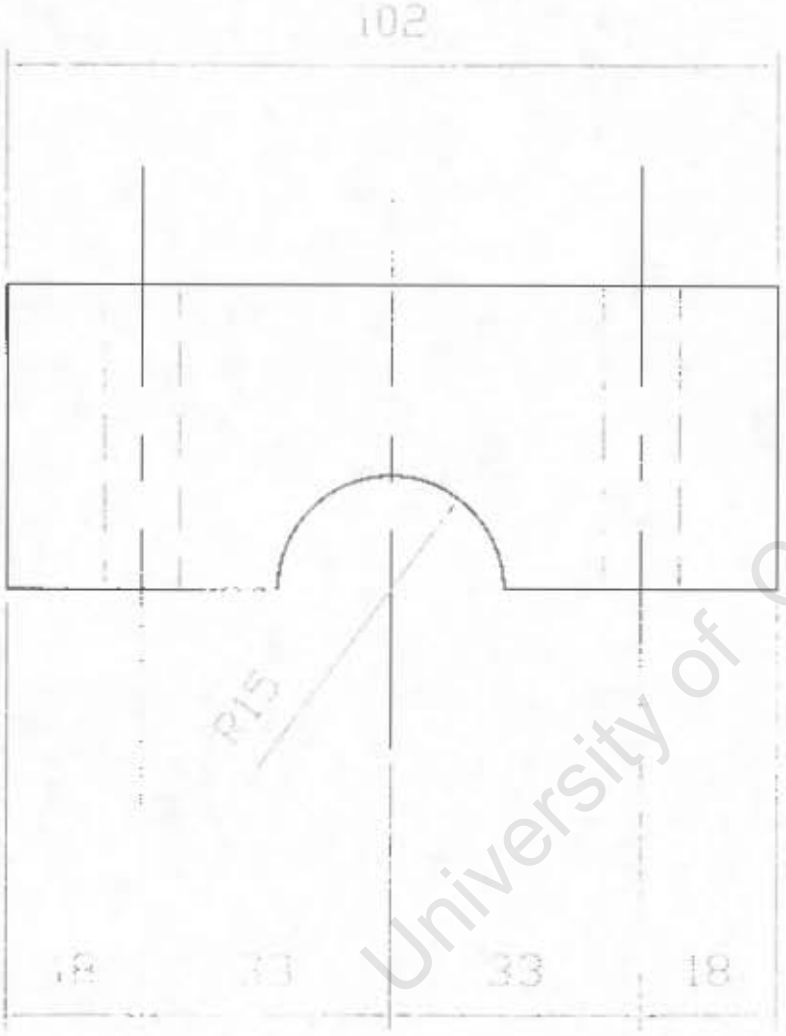

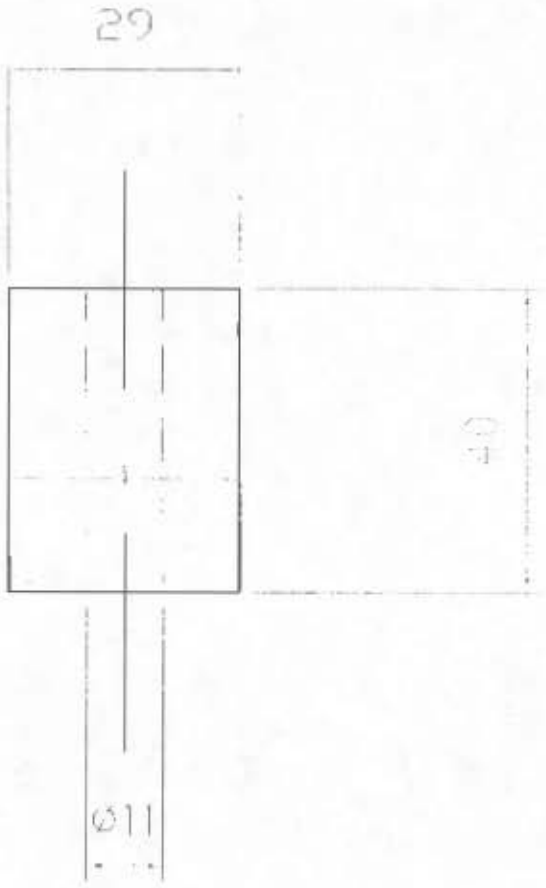

PART No.	DESCRIPTION	MATERIAL	No OFF	REMARKS
3	UPPER SUPPORT	MS	2	

AIR GUN

UNIVERSITY OF CAPE TOWN
DEPARTMENT OF MECHANICAL ENGINEERING

TITLE
UPPER SUPPORT

DIMENSIONS IN MILLIMETRES (mm) TOLERANCE UNLESS OTHERWISE STATED ±0.1

SCALE 1 : 1

DATE 11/08/2000

SHEET 4 OF 5

DRAWN BY S.T.MARAIS

DRAWING NUMBER GASGUN-002-04

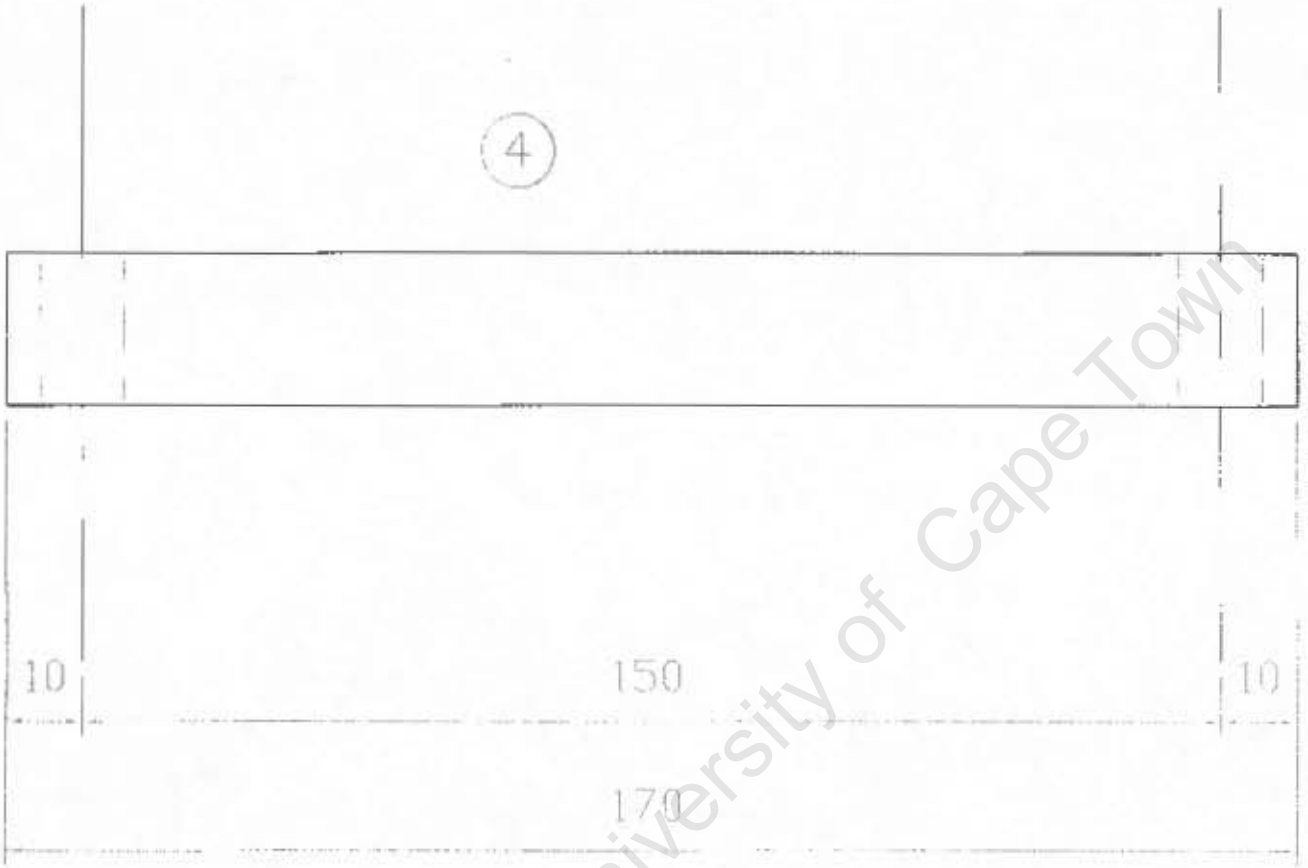

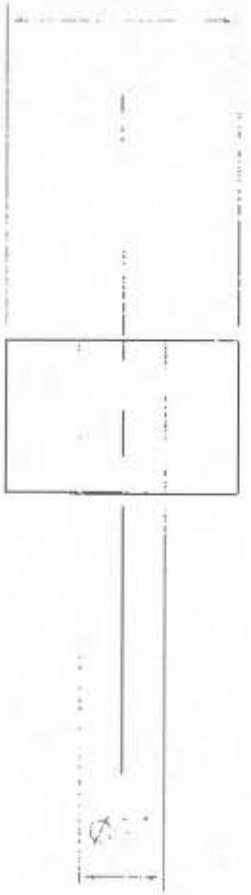

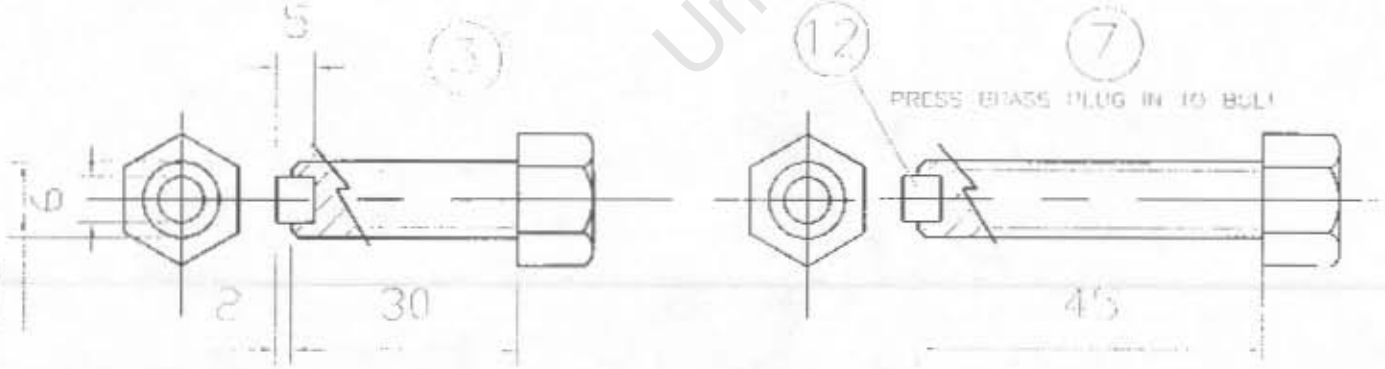

PART No.	DESCRIPTION	MATERIAL	No. OFF	REMARKS
12	BRASS PLUG	BRASS	20	
7	M10 X 45 BOLT		3	
3	M10 X 35 BOLT		17	
4	LOWER CLAMP	MS	3	

AIR GUN

UNIVERSITY OF CAPE TOWN
DEPARTMENT OF MECHANICAL ENGINEERING

TITLE
LOWER CLAMP

DIMENSIONS IN MILLIMETRES (mm) TOLERANCE UNLESS OTHERWISE STATED ±0.1

SCALE 1 : 1

DATE 11/08/2000

SHEET 5 OF 6

DRAWN BY S.T.MARAIS

DRAWING NUMBER GASGUN-002-05

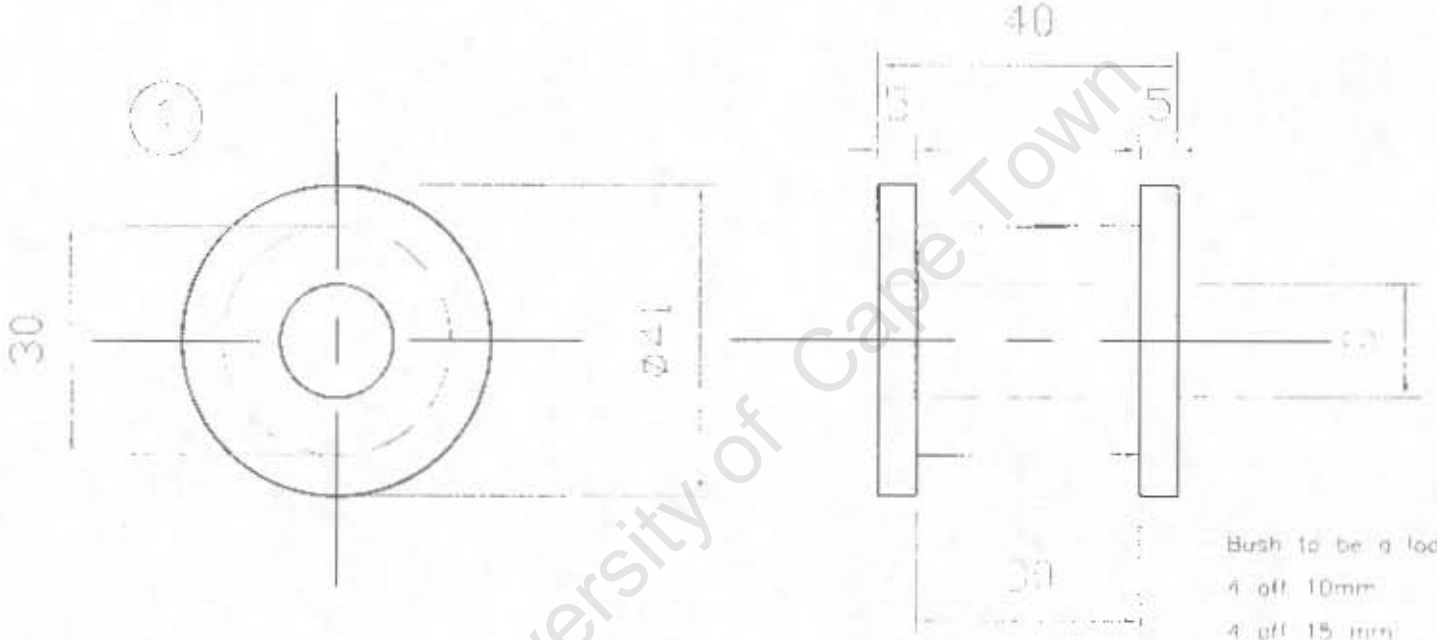

1	BAR SUPPORT BUSH	TEFLON	2	
PART No.	DESCRIPTION	MATERIAL	NO. OFF	REMARKS

AIR GUN

UNIVERSITY OF CAPE TOWN
DEPARTMENT OF MECHANICAL ENGINEERING

TITLE
BAR SUPPORT BUSH

DIMENSIONS IN MILLIMETRES [mm]
TOLERANCE UNLESS OTHERWISE STATED
0.1

SCALE 1 : 1
DATE 03/08/2000
SHEET 6 OF 6
DRAWN BY S.T.MARAIS
DRAWING NUMBER GASGUN-002-06

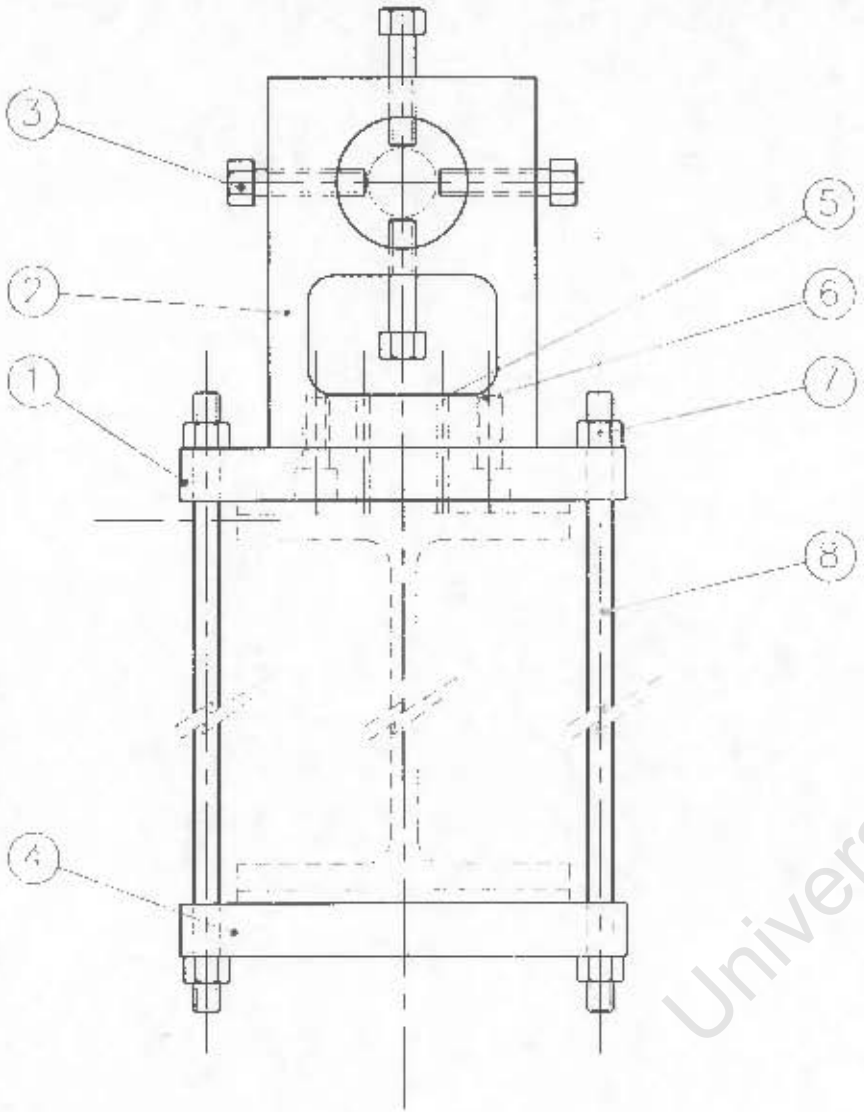

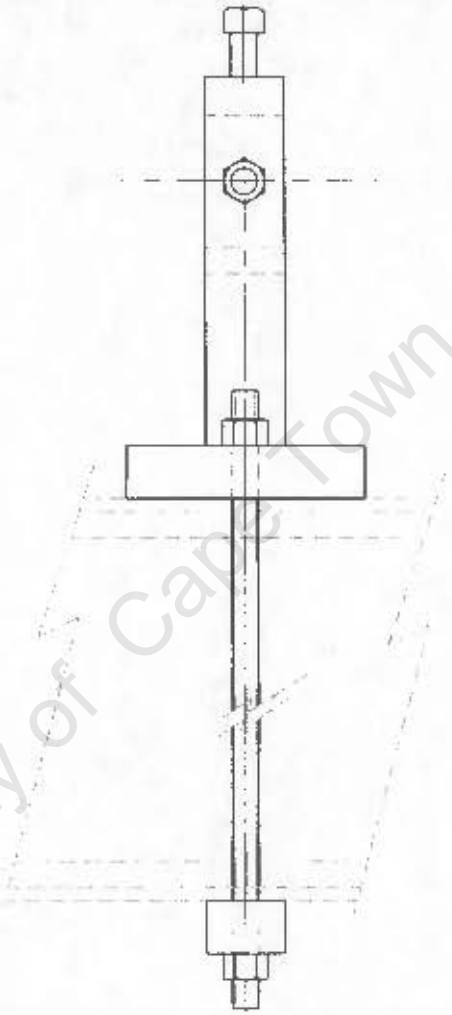

PART No.	DESCRIPTION	MATERIAL	No. OFF	REMARKS
8	M10 THREADED BAR 400 LG.		2	
7	M10 NUT		4	
6	M10 CAP SCREW		2	
5	#5 DOWEL Pin	SILVER STEEL	2	
4	LOWER CLAMP	MS	1	
3	M10 BOLT	MS	4	
2	SUPPORT BLOCK	MS	1	
1	UPPER CLAMP	MS	1	

AIR GUN

UNIVERSITY OF CAPE TOWN
DEPARTMENT OF MECHANICAL ENGINEERING

TITLE
GA FOR BARREL SUPPORTS

DIMENSIONS IN MILLIMETRES (mm) TOLERANCE UNLESS OTHERWISE STATED 0.1

SCALE 1 : 2

DATE 11/08/2000

SHEET 1 OF 3

DRAWN BY S.T.MARAIS

DRAWING NUMBER GASGUN-003-01

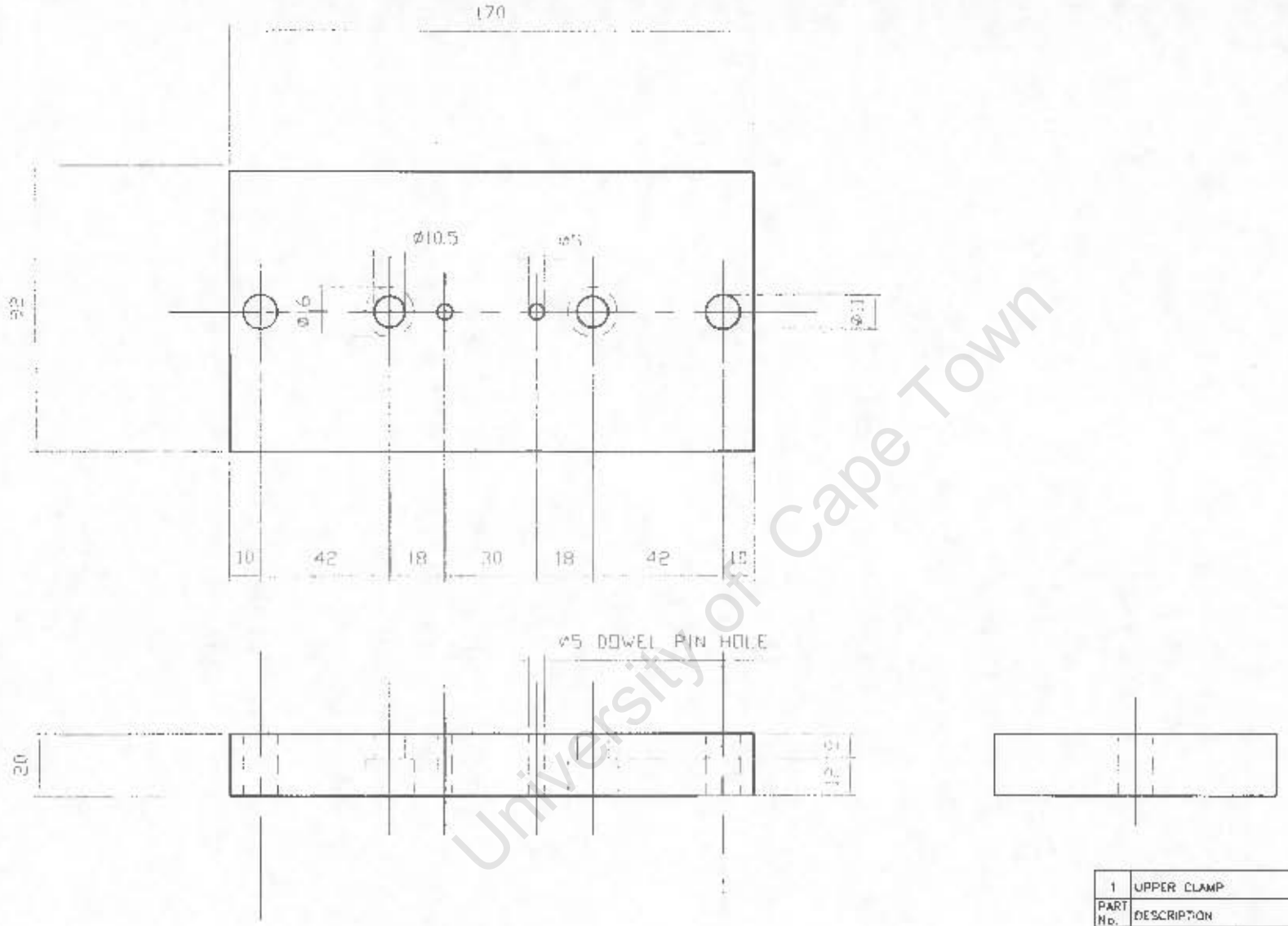

PART No.	DESCRIPTION	MATERIAL	No. OFF	REMARKS
1	UPPER CLAMP	MS	1	

AIR GUN

UNIVERSITY OF CAPE TOWN
DEPARTMENT OF MECHANICAL ENGINEERING

TITLE
UPPER CLAMP

DIMENSIONS IN MILLIMETRES (mm)
TOLERANCE UNLESS OTHERWISE STATED ±1

SCALE 1 : 2
DATE 11/08/2000
SHEET 2 OF 3
DRAWN BY S.T.MARAIS
DRAWING NUMBER GASGUN--003--02

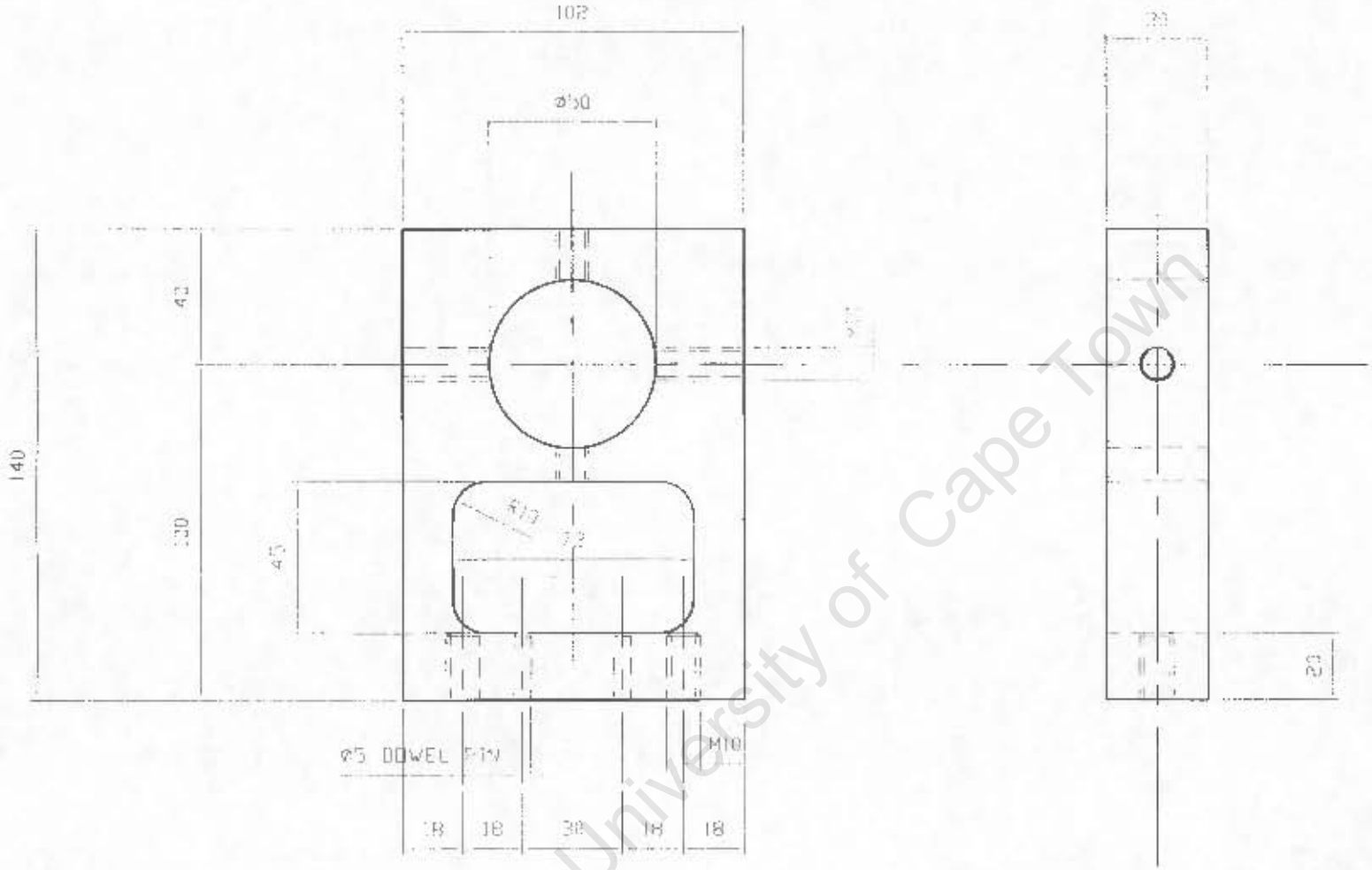

PART No.	DESCRIPTION	MATERIAL	No OFF	REMARKS
2	SUPPORT BLOCK	MS	1	

AIR GUN

UNIVERSITY OF CAPE TOWN
DEPARTMENT OF MECHANICAL ENGINEERING

TITLE
SUPPORT BLOCK

DIMENSIONS IN MILLIMETRES (mm) TOLERANCE UNLESS OTHERWISE STATED ±0.1

SCALE 1 : 2

DATE 11/08/2000

SHEET 3 OF 3

DRAWN BY S.T.MARAIS

DRAWING NUMBER GASGUN-003-03

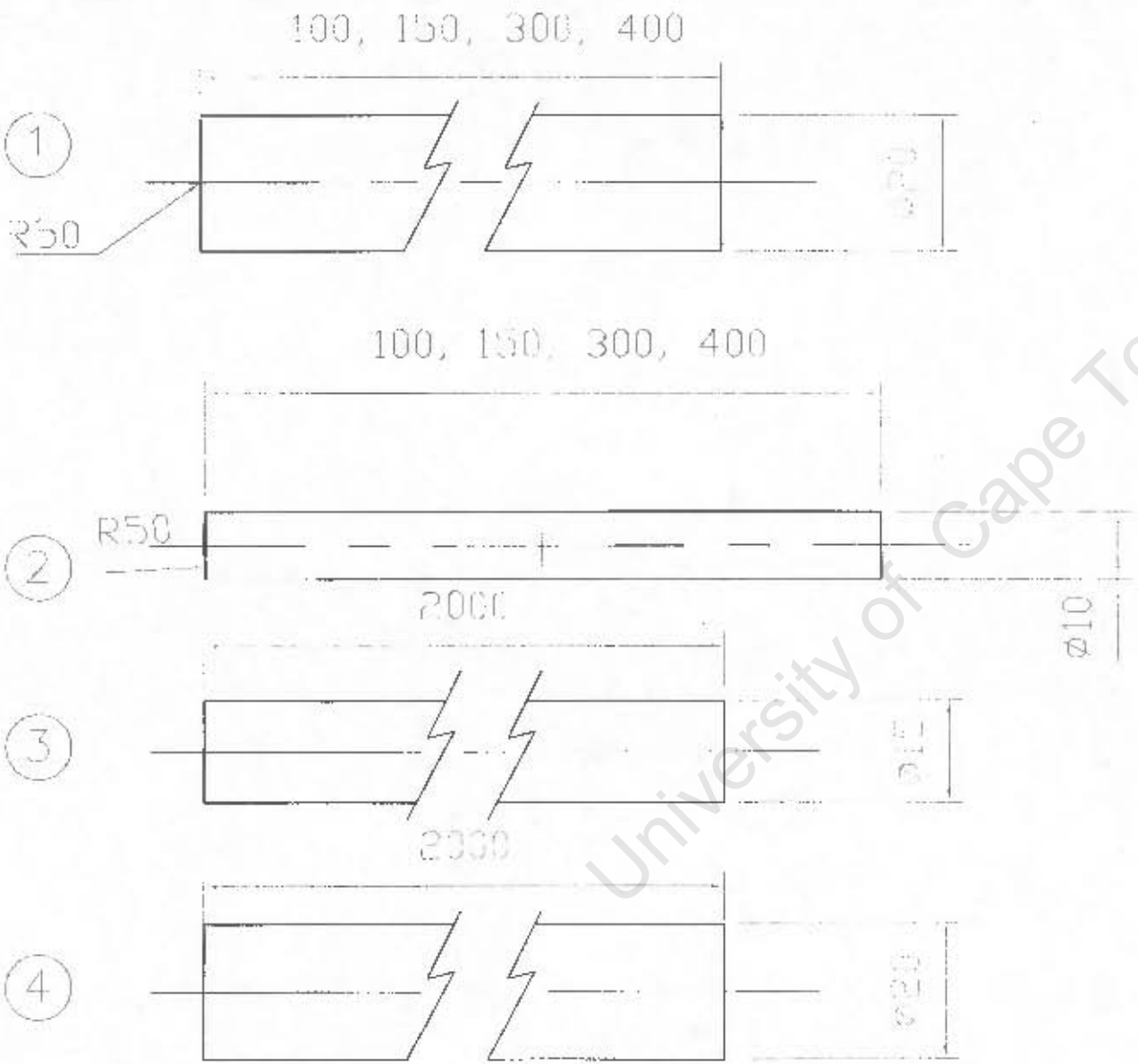

PART No.	DESCRIPTION	MATERIAL	No. OFF	REMARKS
4	INCIDENT BAR (20mm)	SILVER ST	2	
3	INCIDENT BAR (15mm)	SILVER ST	2	
2	STRIKER BAR (10mm)	SILVER ST	1	
1	STRIKER BAR (20mm)	SILVER ST	1	

AIR GUN

UNIVERSITY OF CAPE TOWN
DEPARTMENT OF MECHANICAL ENGINEERING

TITLE
STRIKERS AND BARS

DIMENSIONS IN MILLIMETRES (mm) TOLERANCE UNLESS OTHERWISE STATED ±0.1

SCALE 1 : 1

DATE 03/08/2000

SHEET 1 OF 1

DRAWN BY S.T.MARAIS

DRAWING NUMBER GASGUN - 004 - 01

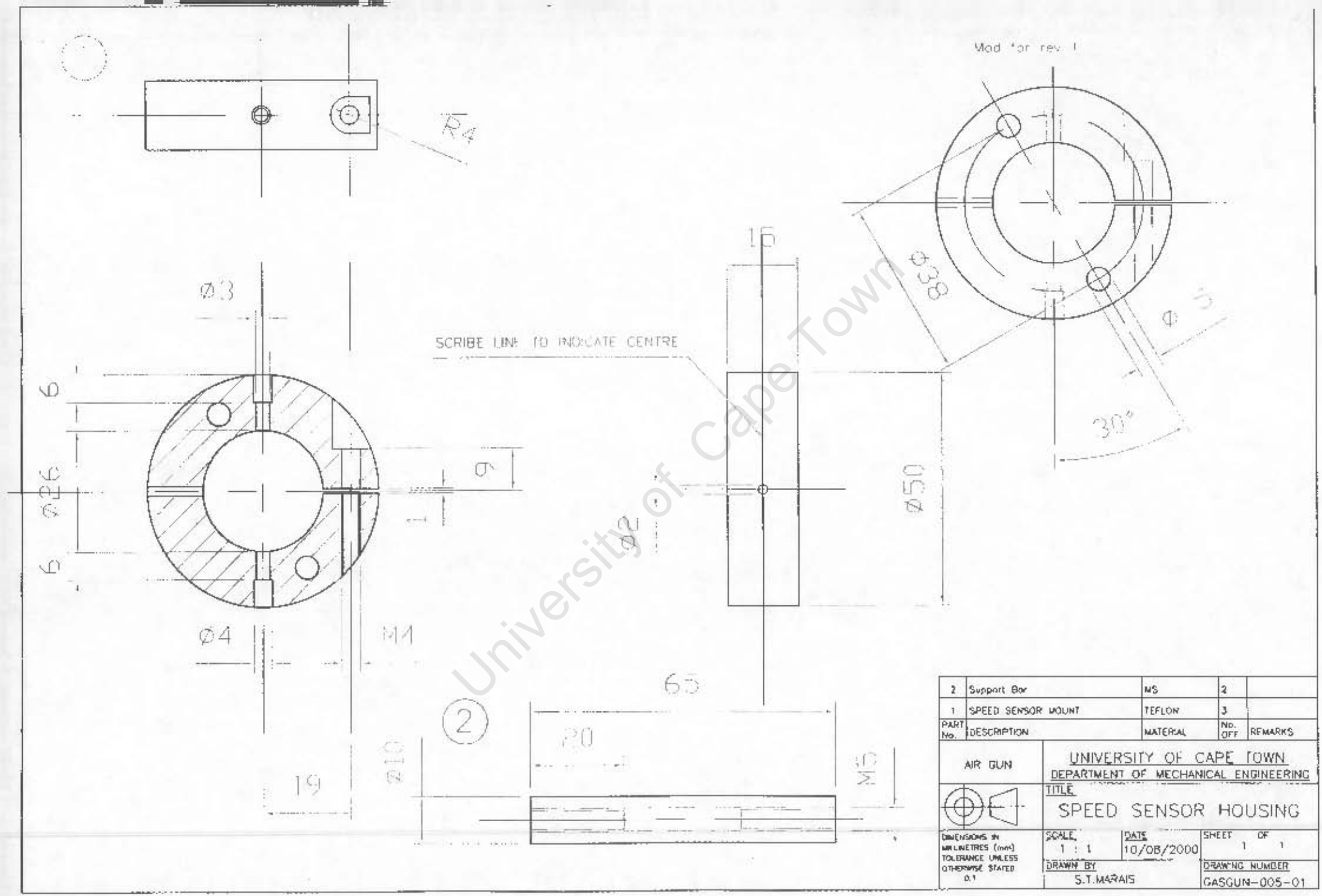

PART No.	DESCRIPTION	MATERIAL	No. OFF	REMARKS
2	Support Bar	MS	2	
1	SPEED SENSOR MOUNT	TEFLON	3	

AIR GUN

UNIVERSITY OF CAPE TOWN
DEPARTMENT OF MECHANICAL ENGINEERING

TITLE
SPEED SENSOR HOUSING

DIMENSIONS IN MILLIMETRES (mm)
TOLERANCE UNLESS OTHERWISE STATED
0.1

SCALE 1 : 1

DATE 10/08/2000

SHEET 1 OF 1

DRAWN BY S.T.MARAIS

DRAWING NUMBER GASGUN-005-01